INTERACTIONS OF BIOMASS DERIVED OXYGENATES WITH HETEROGENEOUS CATALYSTS IN AQUEOUS AND VACUUM ENVIRONMENTS

A Dissertation
Presented to
The Academic Faculty

By

John R. Copeland

In Partial Fulfillment
Of the Requirements for the Degree
Doctor of Philosophy in Chemical Engineering

Georgia Institute of Technology
December, 2013

INTERACTIONS OF BIOMASS DERIVED OXYGENATES WITH HETEROGENEOUS CATALYSTS IN AQUEOUS AND VACUUM ENVIRONMENTS

Approved by:

Dr. Carsten Sievers, Advisor
School of Chemical & Biomolecular Engineering
Georgia Institute of Technology

Dr. David S. Sholl
School of Chemical & Biomolecular Engineering
Georgia Institute of Technology

Dr. Charles L. Liotta
School of Chemical & Biomolecular Engineering
Georgia Institute of Technology

Dr. Christopher T. Williams
Department of Chemical Engineering
University of South Carolina

Dr. Thomas M. Orlando
School of Chemistry and Biochemistry
Georgia Institute of Technology

Date Approved: November 15, 2013

For all those who have supported me over the years.

ACKNOWLEDGEMENTS

The successful completion of graduate school has been the most challenging task that I have undertaken thus far in my life, and would not have been possible without the support of many, truly fantastic people. First, I must thank my advisor, Dr. Carsten Sievers, for putting a great deal of faith in me when accepting me as his first Ph.D. student and for supporting me for the several years that followed. From cleaning out abandoned labs to publishing papers together, my graduate school experience would not have been the same without him. I would also like to thank my thesis committee, comprised of Charles Liotta, Thomas Orlando, David Sholl, and Christopher Williams for their valued expertise and guidance in the direction of my thesis work. I would also like to thank my committee for pushing me to question not only my experimental results, but what I was getting out of my Ph.D. work; this concept changed the way I approached my research and my overall graduate school experience.

There were many other experts that deserve recognition for helping me in conquering myriad obstacles. Kevin Guger, Bradley Donegan, and Charles Brookshire have been amazingly fast and efficient in solving I.T. issues for years. John Starnes and the rest of the Georgia Oven Company were essential in several build projects that became the workhorses of my research. Jeffrey Andrews and Bradley Parker were central to the success of every build project that I have accomplished while setting up a new lab. Without their invaluable expertise, hard work under hard deadlines, and flexibility in making emergency repairs, I would have only accomplished a small fraction of what I have accomplished during the last several years. Michael Buchannan has been my

"analytical chemistry question buddy" for my tenure at Ga Tech, and his help is greatly appreciated. Johannes Leisen was crucial to the design and execution of many MAS-NMR experiments that added much to my research.

I could not have possibly have succeeded in my efforts in graduate school without the help of my fellow group members. I must first give special recognition to Dr. Ryan M. Ravenelle, who was a great mentor, and an even better friend. Ryan helped to get me started on my thesis work by teaching me many experimental techniques and by sharing valuable wisdom regarding good research practices as soon as I started in the lab. I must also thank all my other group members for their support, both professional and personal, and understanding over the challenging years that make up graduate school, including current group members: Jessica Ewbank, Guo Shiou Foo, Sarah Schimming, Gautami Newalkar, Olga Simakova, and Akil Syed, as well as former group members: Paige Case, Maximilian Hahn, Michael König, Jared McGrath, Sudhir Sharma, Abiola Shitta, Tobias Tengler, and Adam Van Pelt. I must also thank the undergraduate researchers whose hard work increased the quality of the research that I was able to conduct, specifically, Alvin Evans, Lindsey Harrison, Treat Jennings, Ivan Santillan, Pedro Torres, and Mark Williams.

Over the last four years, I have had the great fortune of enjoying the company of several great friends, both old and new, whose positive impact on my life made persevering through the trials of my Ph.D. thesis a fight worth fighting. These people include: Ashley Allen, Jose Baltazar, Michael Casciato, Stephanie Didas, Joshua Glueck, Brian Kraftschik, Becky and Lester Li, Michael Mangarella, Ryan Quilling, Saujan Sivaram, Sara Stahley, Kyle Strohl, Aubrey Tiernan, and Kathleen Vermeersch. I must

also thank a very special group of friends, my roommates: Derek Liddell, Jared McGrath, Ryan Ravenelle, Charles Rutter, Andrew Smith, and Archie O'Neal. These people were invaluable to my well-being and happiness, and were key figures in my favorite times spent in Atlanta. I wish all of these incredible friends of mine the best of luck as they also move on to bigger and better things in life.

Finally, I wish to recognize and thank my family for their unconditional support of all my aspirations. I thank my Uncle Tim and Aunt Libby for being so hospitable and generous toward me over the last few years. I thank my brother, David, and my sister, Reagan, for helping me to learn the innumerable life lessons that come with growing up, and for being great examples of how to live my own life better. I thank my mother, Mary, for being an incredible mother, and for cultivating a stalwart foundation in my own character based on love, hard work, and dedication. I thank my father, Randall, for being an incredible father, and for instilling a lifelong love for all things science and engineering related through the countless and priceless hours spent working on "home improvement" projects with me. Without the love and support of my family, I would certainly not be where I am today.

TABLE OF CONTENTS

Page

ACKNOWLEDGEMENTS iv

LIST OF TABLES xi

LIST OF FIGURES xii

LIST OF SYMBOLS AND ABBREVIATIONS xviii

SUMMARY xx

CHAPTER

1 Introduction 1

1.1 Fossil Fuels as Sources for Energy and Chemical Production 1

1.2 Biomass as a Replacement for Fossil Fuels and Chemical Feedstocks 7

1.3 Current Understanding of the Heterogeneously Catalyzed Conversion of Biomass Derived Oxygenates in Aqueous Phase 11

1.4 Objectives and Organization 18

2 Surface Interactions of C_2 and C_3 Polyols with γ-AL_2O_3 and the Role of Coadsorbed Water. 20

2.1 Background 20

2.2 Materials and Methods 22

2.2.1 Materials 22

2.2.2 Catalyst Characterization 23

2.2.3 Aqueous Phase Adsorption Isotherms 24

2.2.4 Impregnation of γ-Al_2O_3 with Oxygenate Solutions for IR and NMR Spectroscopy. 25

2.2.5 NMR Spectroscopy 26

2.2.6 IR Spectroscopy of Adsorbed Species 26

2.2.7 DFT Calculations 27

2.3 Results 28

2.3.1 Catalyst Characterization 28

2.3.2 Aqueous Phase Adsorption Isotherms 29

2.3.3 ^{2}H Solid Echo Pulse NMR 30

2.3.4 IR Spectroscopy 32

2.3.4.1 Interactions with OH Groups of γ-Al_2O_3 via IR Spectroscopy 32

2.3.4.2 Ethylene Glycol on γ-Al_2O_3 34

2.3.4.3 1,2-Propanediol on γ-Al_2O_3 36

2.3.4.4 1,3-Propanediol on γ-Al_2O_3 38

2.3.4.5 Glycerol on γ-Al_2O_3 40

2.3.5 DFT Calculations of Glycerol/γ-Al_2O_3 interactions 42

2.4 Discussion 48

2.4.1 Adsorption Behavior of Polyols on γ-Al_2O_3 48

2.4.2 Surface Species Formed by Polyols on γ-Al_2O_3 51

2.4.3 Influence of the Presence of Water on the Surface Species Formed by Polyols on γ-Al_2O_3 54

2.4.4 Sites for Alkoxy Bond Formation on γ-Al_2O_3 57

2.4.5 Implications for the Stability of γ-Al_2O_3 in Hot Liquid Water 59

2.5 Conclusions 60

3 Surface Interactions of Glycerol with Acidic and Basic Metal Oxides 62

3.1 Background 62

3.2 Materials and Methods 66

3.2.1 Materials 66

3.2.2 Catalyst Characterization 67

3.2.3 IR Spectroscopy of Adsorbed Glycerol 69

3.3 Results 70

3.3.1 Catalyst Characterization 70

3.3.2 Surface Hydroxyl Interactions Evidenced by IR Spectroscopy 79

3.3.3 Glycerol Surface Species by IR Spectroscopy 81

3.4 Discussion 87

3.4.1 Surface Properties of Metal Oxides 87

3.4.2 Role of Lewis Acid Sites in the Formation of Surface Species from Glycerol on the Metal Oxides 89

3.4.3 Role of Basic Oxygen Sites in the Formation of Surface Species from Polyols on the Metal Oxides 91

3.4.4 Role of Basic Surface Hydroxyls in the Surface Interactions of Glycerol with Metal Oxides 94

3.4.5 Role of Water in the Surface Interactions of Glycerol with Metal Oxides 95

3.4.6 Importance of Findings for Heterogeneous Catalysis and Other Fields 97

3.5 Conclusions 98

4 In Situ ATR-IR Study on Aqueous Phase Reforming Reactions of Glycerol over a Pt/γ-Al2O3 Catalyst 100

4.1 Background 100

4.2 Materials and Methods 103

4.3 Results and Discussion 106

4.3.1 Catalyst Characterization and Stability 106

4.3.2 Identification and Evolution of Surface Species During Cleaning Cycles 107

4.3.3 Surface Species Formed During Glycerol APR 119

4.3.4 Kinetics of Glycerol Conversion after Different Pretreatments 127

4.4 Conclusions 137

Appendix A: Supplementary Information for Chapter 2 139

A.1 IR Spectra Normalization and Subtraction Procedure for Difference Spectra 144

A.2 DFT Experimental Details 145

A.3 Reaction Energy ΔE 146

A.3.1 Molecular Adsorption 146

A.3.2 Dissociation of the First H 147

A.3.3 Dissociation of the Second H 147

A.3.4 Desorption of Surface H as $\frac{1}{2}H_{2(g)}$ 147

A.3.5 Surface H Reacting with Surface OH and Leaving as $H_2O_{(g)}$ 147

A.4 Reaction Mechanism from PBE Calculation 148

A.5 Comparison of the Most Stable Structures for PBE and PBE+D2 Methods. 149

Appendix B: Supplementary Information for Chapter 3 151

Appendix C: Supplementary Information for Chapter 4 161

REFERENCES 164

VITA 179

LIST OF TABLES

Page

Table 2.1: Comparison of experimentally observed and calculated vibrational modes of pure, liquid glycerol and glycerol on γ-Al_2O_3 in the 1200-1000 cm^{-1} region.46

Table 3.1: Carbonate mode assignment from CO2 adsorption and desorption. All frequencies are in cm-1. 74

Table 3.2: Assignments of the νOH vibrations observed in the IR spectra of the metal oxides. 78

Table 4.1: N_2 physisorption and acidity measurement results for 5 wt% Pt/γ-Al_2O_3 catalyst 107

Table 4.2: Vibrational modes of pure glycerol, glycerol solution, and glycerol solution flown over the catalyst layer 123

Table 4.3: First order step response function fit parameters for Pt bound CO species with different pretreatment procedures. 131

Table A.1: Select IR peak positions of pure oxygenates and oxygenates loaded on γ-Al_2O_3 in various environments. 143

Table A.2: Comparison of structures for PBE and PBE+D2 method as shown in Figure A.7 and Figure 2.8, the distance of O-Al bond formed between oxygen of glycerol and surface Al atoms (Å), the H bond distance between the glycerol and surface (Å). 149

Table A.3: Comparison of experimentally observed and literature values of vibrational frequencies of surface OH groups of γ-Al_2O_3. Number following μ indicates the coordination number of the OH group, and the numbers in the parenthesis indicate the Miller index of the plane in which the OH group exists. 150

Table B.1: Area densities in mg/cm^2 of the metal oxide wafers used for all of the in situ transmission IR experiments carried out in the present study. 151

Table B.2: Metal Oxide N_2 Physisorption Results. 151

Table B.3: Total and strong acid site concentrations in $\mu mol/m^2$ 153

LIST OF FIGURES

Page

Figure 1.1: Recent trends in crude oil consumption, import, and production in the U.S.A. 3

Figure 1.2: Global mean CO_2 concentration predictions that include dynamic amounts of atmospheric CO_2 and terrestrial vegetation (red), dynamic CO_2 concentration and fixed vegetation (dashed), and a model that neglects CO_2 induced climate change (blue). 4

Figure 1.3: A simplified flow diagram of a typical crude oil refinery optimized for the production of transportation fuels including various heterogeneously catalyzed processes.....7

Figure 1.4: The three major macromolecules of lignocellulosic biomass and the natural chemical intermediates they can be transformed into. 9

Figure 1.5: Value added products and chemical intermediates that can be derived from glucose via fermentation and catalytic routes. 13

Figure 1.6: Aqueous phase reforming reaction pathways for the production of H_2 and alkanes from polyols. 15

Figure 2.1: Aqueous phase adsorption isotherms of the oxygenate molecules on γ-Al_2O_3. Solid lines indicate adsorption isotherms of the molecules on ZSM-5, and dashed lines indicate adsorption isotherms of the molecules on γ-Al_2O_3. ♦ = EG, ■ = 1,2-PDO, ▲ = 1,3-PDO, and ● = glycerol.....30

Figure 2.2: ^2H NMR of 4.3 wt% (1,1,2,2,$^2H_4$)EG on γ-Al_2O_3 (a, b, c) and 1.3 wt% (1,1,2,3,3,$^2H_5$)glycerol on γ-Al_2O_3 (d, e, f). Samples were subjected to flowing ambient air (a and d), followed by flowing dry air (b and e), followed by flowing ambient air again (c and f, f shown in grey for clarity). 31

Figure 2.3: IR spectra of pure γ-Al_2O_3 and difference spectra of oxygenate molecules on γ-Al_2O_3 with the γ-Al_2O_3 spectrum subtracted. Solid lines indicate samples under HV at RT. Dotted lines indicate samples at RTP. 33

Figure 2.4: IR spectra of liquid EG and EG on γ-Al_2O_3. Liquid EG, a. EG on γ-Al_2O_3 at RTP, b. EG on γ-Al_2O_3 after 1 h spent at RTHV, c. EG on γ-Al_2O_3 after 1 h spent at 1.00 mbar of H_2O vapor, d. Spectra b-d are difference spectra in which the spectrum of γ-Al_2O_3 was subtracted from the EG loaded sample.35

Figure 2.5: IR spectra of pure 1,2-PDO and 1,2-PDO on γ-Al_2O_3. Pure 1,2-PDO, a. 1,2-PDO on γ-Al_2O_3 at RTP, b. 1,2-PDO on γ-Al_2O_3 after 1 h spent at RTHV, c. Difference spectrum of c and b, d. 1,2-PDO on γ-Al_2O_3 after 1 h spent at 1.00 mbar of H_2O vapor, e. Spectra b, c, and e are difference spectra in which the spectrum of γ-Al_2O_3 was subtracted from the 1,2-PDO loaded sample. 37

Figure 2.6: IR spectra of pure 1,3-PDO and 1,3-PDO on γ-Al_2O_3. Pure 1,3-PDO, a. 1,3-PDO on γ-Al_2O_3 at RTP, b. 1,3-PDO on γ-Al_2O_3 after 1 h spent at RTHV, c. 1,3-PDO on γ-Al_2O_3 after 1 h spent at 1.00 mbar of H_2O vapor, d. Spectra b-d are difference spectra, where the spectrum of γ-Al_2O_3 was subtracted from the 1,3-PDO loaded sample. 39

Figure 2.7: IR spectra of pure glycerol and glycerol on γ-Al_2O_3. Pure glycerol, a. glycerol on γ-Al_2O_3 at RTP, b. glycerol on γ-Al_2O_3 after 1 h spent at RTHV, c. glycerol on γ-Al_2O_3 after 1 h spent at 1.00 mbar of H_2O vapor, d. Spectra b-d are difference spectra, where the spectrum of γ-Al_2O_3 was subtracted from the glycerol loaded sample. 41

Figure 2.8: Side and top views of the most energetically favorable surface species of glycerol on γ-Al_2O_3 (110). Energies are relative to the previous step. Molecular adsorption, a. Adsorption with dissociation of one H atom, b. Adsorption with dissociation of a second H atom, c. Single dissociated H leaving as ½$H_{2(g)}$, d. Single dissociated H forming H_2O with a surface OH of γ-Al_2O_3 and leaving as $H_2O_{(g)}$, e.....43

Figure 2.9: Most energetically favorable conformation of glycerol adsorbed on γ-Al_2O_3 in the case of single H dissociation, a. Molecule rotated 90° for clarity, b. Atoms are labeled for vibrational mode analysis in Table 2.1. 47

Figure 3.1: Lewis acid site concentrations of the metal oxides according to pydridine adsorption/TPD followed by IR spectroscopy. 72

Figure 3.2: IR spectra showing the νOH region of the metal oxides used in the present study after one hour spent under UHV conditions: γ-Al2O3 (a), basic γ-Al2O3 (b), TiO2 (c), ZrO2 (d), Alfa ZrO2 (e), MgO (f), CeO2 (g).....76

Figure 3.3: νOH Difference IR spectra of glycerol loaded metal oxide minus wetted metal oxide. Metal oxides include: γ-Al2O3 (a), basic γ-Al2O3 (b), TiO2 (c), ZrO2 (d), Alfa ZrO2 (e), MgO (f), CeO2 (g). The subscripts indicate the environment that the sample was exposed to at the time the spectrum was collected: RTP (1), UHV (2), and 0.1 mbar water vapor (3). 80

Figure 3.4: νCH and νCO regions of the difference IR spectra of glycerol loaded metal oxide minus wetted metal oxide. Metal oxides include: γ-Al2O3 (a), basic γ-Al2O3 (b), TiO2 (c), ZrO2 (d), Alfa ZrO2 (e), MgO (f), CeO2 (g). The subscripts indicate the environment that the sample was exposed to at the time the spectrum was collected: RTP (1), UHV (2), and 0.1 mbar water vapor (3). 82

Figure 3.5: Depiction of glycerol adsorbed to CUS sites of a metal oxide. The white spheres indicate hydrogen atoms, the light grey spheres indicate oxygen atoms, the dark grey spheres indicate CUS surface metal atoms of a metal oxide, and the black spheres indicate carbon atoms. 83

Figure 3.6: νCO frequency of alkoxy interaction vs. metal oxide metal atom electronegativity. γ-Al2O3 (♦), basic γ-Al2O3 (■), TiO2 (▲), ZrO2 (X), Alfa ZrO2 (○),CeO2 (+). RTP values shown in black, if UHV treatment induced a shift in νCO frequency, then the frequency when under UHV is shown in grey. 85

Figure 4.1: Flow periods used period used during the cleaning cycle experiment. Before the O2(H2O) flow period that starts at -35 min, H2O was flowed over the catalyst layer for 3 h, and is not shown. The black arrow indicates the time at which the background was collected. 109

Figure 4.2: ATR-IR difference spectra of the catalyst layer during the cleaning cycle experiment. Spectra were recorded at the end of the following flow periods: first H_2O a), first $O_2(H_2O)$ b), first $H_2(H_2O)$ c), second H_2O d), second $O_2(H_2O)$ e), third $H_2(H_2O)$ f), third H_2O g), third $O_2(H_2O)$ h), fourth $H_2(H_2O)$ i), fourth H_2O j), fourth $O_2(H_2O)$ k). 111

Figure 4.3: Integrated peak areas of νCO_L modes during cleaning cycle experiment. Each flow period is labeled at the top of the figure. O_2 denotes $O_2(H_2O)$ flow, H_2 denotes $H_2(H_2O)$ flow. CO_L/H, ◊ , was centered at ca. 2052 cm^{-1} peak. CO_L/H_2O, ●, was centered at ca. 1990 cm^{-1}. 113

Figure 4.4: Flow compositions of different experiments: control experiment with H_2O pretreatment, a. $O_2(H_2O)$ pretreatment, b. $H_2(H_2O)$ pretreatment ,c. Two cleaning cycles, d. At least 3 h of H_2O flow preceded each experiment, and is not shown. Gly(H_2O) indicates, 0.100 M aqueous solution of glycerol. The black arrow indicates the time at which the background was collected. 121

Figure 4.5: ATR-IR spectra of catalyst layer, subjected to a H_2O pretreatment period, during and after glycerol solution exposure. All of the spectra were collected at the end of their respective flow period. Pure glycerol is shown for reference, a). 0.100 M glycerol flowing over the catalyst, b). H_2O flow after the glycerol flow period, c). $O_2(H_2O)$ flow that followed the H_2O flow, d). 122

Figure 4.6: Integrated peak areas of the $\nu CO_L/H$ mode as a function of time and pretreatment period used. H_2O pretreatment, X. $O_2(H_2O)$ pretreatment, ■. Multiple cleaning cycles pretreatment, ▲.....129

Figure 4.7: Integrated peak areas of the $\nu CO_L/H_2O$ mode as a function of time and pretreatment period used. H_2O pretreatment, X. $O_2(H_2O)$ pretreatment, ■. $H_2(H_2O)$ pretreatment, ○. Multiple cleaning cycles pretreatment, ▲.....129

Figure 4.8: Integrated peak areas of the νCO_B mode as a function of time and pretreatment period used. H_2O pretreatment, X. $O_2(H_2O)$ pretreatment, ■. $H_2(H_2O)$ pretreatment, ○. Multiple cleaning cycles pretreatment, ▲.....130

Figure 4.9: ATR-IR spectra of catalyst layer at the end of the glycerol exposure period of the different pretreatment experiments showing the Pt bound νCO region. $H_2(H_2O)$ pretreatment, a. H_2O pretreatment, b. $O_2(H_2O)$ pretreatment, c. Multiple cleaning cycles pretreatment, d. 133

Figure A.1: Sketch of the high vacuum chamber used in the present study. P1 is a cryogenic pump, P2 is a turbo-molecular pump, P3 is a rotary vane pump, P4 is a membrane pump. V1 and V2 are 90° high vacuum valves, V3 is a leak valve, V4 is a high-vacuum glassware valve with a Viton o-ring that is part of the 50 ml sample vessel where water or other probe molecules are contained, V5 is a bellows sealed valve. 139

Figure A.2: Schematic of the in situ high vacuum transmission IR cell used in the present study. The ZnSe windows were sealed on either side of each window with custom made 1 mm thick PTFE gaskets (not shown). The heating wire and the thermocouple are soldered to the removable cell top / sample holder. The removable cell top / sample holder seals to the cell with a CF 40 flange and a copper gasket. The "To UHV Chamber" connection is a CF 16 flange with a copper gasket. 140

Figure A.3: Top view of the γ-Al_2O_3 surfaces used in this work: hydrated (110) surface with 5.9 OH/nm^2. Atoms in the first layer are shown in a ball and stick form with white (H), red (O), and pink (Al) balls. The surface unsaturated Al is marked by purple balls. The other layers are shown in a stick representation. 141

Figure A.4: XRD diffractogram of γ-Al_2O_3 used in the current study. 141

Figure A.5: ^{27}Al MAS-NMR of γ-Al_2O_3 used in the current study. 142

Figure A.6: A depiction of glycerol in the αα conformation. Grey balls are carbon atoms, red balls are oxygen atoms, and white balls are hydrogen atoms. 144

Figure A.7: Side and top views of the most energetically favorable surface species in the case of glycerol on γ-Al_2O_3(110) surface with energies relative to the previous scenario, a: molecular adsorption; b: single H dissociation; c: second H dissociation; d: single dissociated H leaving as ½$H_{2(g)}$; e: single dissociated H bonding with a surface OH γ-Al_2O_3(110) surface and leaving as ½$H_2O_{(g)}$. Small white balls: H; red balls: surface O; green balls: O of glycerol; gray balls: C; pink balls: Al atoms; purple balls: unsaturated surface Al atoms. The black cycle indicated the dissociated H from glycerol in that reaction step. 148

Figure B.1: XRD diffractograms of metal oxides. γ-Al_2O_3 (a), basic γ-Al_2O_3 (b), TiO_2 (c), ZrO_2 (d), Alfa ZrO_2 (e), MgO (f), CeO_2 (g). The numbers in parenthesis indicate the family of planes to which the corresponding peak is assigned. 152

Figure B.2: IR difference spectra of pyridine on metal oxides after 200 °C desorption temperature. γ-Al_2O_3 (a), basic γ-Al_2O_3 (b), TiO_2 (c), ZrO_2 (d), Alfa ZrO_2 (e), MgO (f), CeO_2 (g). 154

Figure B.3: Wafer mass normalized integrated peak areas of pyridine coordinated to LAS for the ZrO_2 samples. 155

Figure B.4: Relative Lewis acid site concentration of the metal oxides as a function of pyridine desorption temperature. γ-Al_2O_3 (♦), basic γ-Al_2O_3 (■), TiO_2 (▲), ZrO_2 (X), Alfa ZrO_2 (○), MgO (●), CeO_2 (+). 155

Figure B.5: IR spectra of the temperature programmed desorption of CO_2 from the metal oxides. The samples shown are γ-Al_2O_3 (a), basic γ-Al_2O_3 (b), ZrO_2 (c), Alfa ZrO_2 (d), MgO (e), and CeO_2 (f). The number in subscript denotes the highest desorption temperature that the sample was exposed to: 100 °C (1), 200 °C (2), 300 °C (3), 400 °C (4), and 500 °C (5). 156

Figure B.6: IR spectra of CO_2 adsorption on TiO_2 at various pressures. CO_2 pressures as follows: 0.14 mbar (a), 0.51 mbar (b), 1.02 mbar (c), 2.53 mbar (d), 5.01 mbar (e), 10.02 mbar (f), UHV (g). 157

Figure B.7: IR spectra of the wetted metal oxides at RTP. γ-Al_2O_3 (a), basic γ-Al_2O_3 (b), TiO_2 (c), ZrO_2 (d), Alfa ZrO_2 (e), MgO (f), CeO_2 (g). 158

Figure B.8: Adsorbed carbonate region of the IR spectra of the wetted metal oxides after one hour spent under HV. γ-Al_2O_3 (a), basic γ-Al_2O_3 (b), TiO_2 (c), ZrO_2 (d), Alfa ZrO_2 (e), MgO (f), CeO_2 (g). 159

Figure B.9: Shift in electron density due to increased electronegativity of metal atom to which glycerol is bound. Arrows indicate direction of shifts in electron density. The white spheres indicate hydrogen atoms, the light grey spheres indicate oxygen atoms, the dark grey spheres indicate CUS surface metal atoms of a metal oxide, and the black spheres indicate carbon atoms. 160

Figure C.1: XRD diffractogram of the 5 wt% Pt/g-Al_2O_3 catalyst used in the current study. 161

Figure C.2: ^{27}Al MAS-NMR Spectrum of the 5 wt% Pt/g-Al_2O_3 catalyst used in the current study. 161

Figure C.3: Transmission FT-IR of the catalyst after activation, exposure to 0.110 mbar pyridine for 30 min, and subsequent high vacuum exposure for 30 min. ..162

Figure C.4: Difference spectra of the catalyst layer collected every 5 min during the $O_2(H_2O)$ flow period, black arrow indicates direction of increasing time. The subtrahend spectrum was the spectrum collected just prior to the the $O_2(H_2O)$ flow period so that changes upon the admission of oxygen can be clearly observed.....163

LIST OF SYMBOLS AND ABBREVIATIONS

δ	deformation vibrational mode
ν	stretching vibrational mode
1,2-PDO	1,2-propanediol
1,3-PDO	1,3-propanediol
AES	Auger electron spectroscopy
APR	aqueous phase reforming
ATR-IR	attenuated total reflectance infra-red spectroscopy
BAS	Brønsted acid site
BET	Brunauer-Emmett-Teller
BJH	Barett-Joyner-Halenda
boe	barrel of oil energy equivalent
Btu	British thermal unit
CO_B	CO bridge bound to Pt
CO_L	CO linearly bound to Pt
CO_L/H	CO linearly bound to Pt interacting with dissociatively adsorbed hydrogen
CO_L/H_2O	CO linearly bound to Pt interacting with molecularly adsorbed water
CUS	coordinatively unsaturated
DFT	density functional theory
EG	ethylene glycol
FT-IR	Fourier transform infra-red spectroscopy
H*	dissociatively adsorbed hydrogen on Pt
H/C	hydrogen to carbon ratio

HREELS	high resolution electron energy loss spectroscopy
HV	high vacuum
IR	infra-red
LAS	Lewis acid site
MAS NMR	magic angle spin nuclear magnetic resonance
MCT/A	mercury cadmium telluride antimonide
MMbpd	million barrels per day
NMR	nuclear magnetic resonance
O/C	oxygen to carbon ratio
PIXE	proton induced x-ray emission
Qbtu	quadrillion British thermal units
RT	room temperature
RTHV	room temperature and high vacuum
RTP	room temperature and pressure
TPD	temperature programmed desorption
UHV	ultra-high vacuum
WGS	water-gas shift
XPS	x-ray photoelectron spectroscopy

SUMMARY

The recognition of the finite nature and limited availability of fossil fuels has resulted in a heightened interest in finding more sustainable replacements for the precursors of transportation fuels and chemicals. Biomass is one of the most promising replacements as it can be grown indigenously, sustainably, and in a carbon neutral fashion. Heterogeneous catalysts, such as metal oxides and metals supported on metal oxides, play a large role in oil refining and chemical production in large part due to their favorable stability, selectivity, and economic utilization relative to other chemical conversion methods. Consequently, metal oxide containing heterogeneous catalysts are also expected to play a large role in the industrial scale catalytic upgrading of biomass in the future.

The knowledge based design of catalysts for the development of more effective and efficient processes in petrochemical refining required an understanding of the relevant surface chemistry involved. Similarly, the rational design of catalysts for biomass upgrading will require an in-depth knowledge of how biomass molecules interact with heterogeneous catalyst surfaces. However, the chemical makeup of most biomass derived molecules presents a new set of challenges in studying their catalytic surface chemistries. As most biomass derived molecules are highly oxygenated, they typically exhibit low vapor pressures and are soluble in polar solvents. Water is the preferred solvent due to its low cost, general availability, and environmentally benign nature. Most traditional surface science techniques require dosing the molecule being studied via gas phase, the use of ultra-high vacuum conditions, and the lack of “sticky”

molecules, which include those with low vapor pressures and water. As a result, alternative methods must be developed and utilized in order to study the surface science of biomass derived oxygenates on heterogeneous catalysts.

The purpose of this dissertation is to develop and utilize methods which provide an understanding of how biomass derived oxygenate molecules and model compounds interact with metal oxide catalysts, and to understand how the presence of water effects such interactions. More specifically, there are three main objectives in this thesis: to understand how polyols interact with metal oxide surfaces, to elucidate the role of various strengths and types of surface sites on polyol-metal oxide interactions, and to discover the surface species of kinetic importance in aqueous phase reforming reactions of biomass molecules.

The first study investigates the surface species formed by two and three carbon polyols on γ-Al_2O_3. Polyols are used because they are functionally similar to biomass derived carbohydrates, and γ-Al_2O_3 is used because it is a common solid acid catalyst and metal catalyst support. The polyols with alcohol groups on the one and three carbons, 1,3-propanediol and glycerol, form a chemisorbed surface species with a bridging alkoxy bond and an acid/base interaction through their primary alcohol groups to Lewis acid sites on the γ-Al_2O_3 in the presence of bulk, coadsorbed water. In contrast, the polyols with alcohol groups only on the one and two carbons, ethylene glycol and 1,2-propanediol, only form alkoxy bonds with the γ-Al_2O_3 when bulk water is not present, and adsorbing water reverses the formation of some of these bonds. Consequently, polyols interact with γ-Al_2O_3 primarily through their alcohol groups to Lewis acid sites. The alcohol groups must be spaced far enough from one another on the carbon backbone

of the polyol so that steric constraints allow multiple alcohol groups to interact with the surface in the presence of bulk water. Otherwise, coadsorbed water can prevent strong adsorption of the polyol.

The second study examines how glycerol adsorbs to various metal oxide surfaces in order to provide an understanding of how different strengths and types of acid and base sites affect the surface species formed by glycerol. It was found that glycerol engages in the same bridging alkoxy and acid/base interactions on all other metal oxides which contained strong Lewis acid sites, TiO_2, ZrO_2, and CeO_2, as it did on γ-Al_2O_3. Glycerol forms an additional hydrogen bond through its secondary alcohol group to basic surface oxygen sites for the metal oxides with weakly basic surface oxygen atoms, γ-Al_2O_3, TiO_2, and CeO_2. ZrO_2 has strongly basic surface oxygen atoms which are effectively poisoned by CO_2 from exposure to atmosphere and thus cannot interact with the adsorbed glycerol. As a result, the primary means for a glycerol to interact with a metal oxide is through its primary alcohol groups to strong Lewis acid sites on the metal oxide; interactions with basic surface oxygen atoms or surface hydroxyls are significantly weaker and are of import when the metal oxide lacks strong Lewis acid sites.

The third study explores the effect of Pt bound species on the aqueous phase reforming dynamics of glycerol over a 5 wt% Pt on γ-Al_2O_3 catalyst as monitored by in-situ attenuated total reflectance infra-red spectroscopy. It was found that pre-adsorbed hydrogen or oxygen from reduction and cleaning pretreatments effectively block active sites and result in artificially slow apparent rates of Pt bound CO formation. A pretreatment consisting of at least two iterations of dissolved oxygen, followed by dissolved hydrogen, followed by dissolved helium flow periods provides a clean Pt

surface for monitoring carbon monoxide formation rates, and allows for the observation of the preferential removal of bridging bound CO from the Pt surface by water-gas shift reactions. These results indicate that the catalyst layer pretreatment must be carefully chosen for subsequent reaction dynamics studies, that water-gas shift removal of Pt bound CO is the rate limiting step in the aqueous phase reforming of glycerol. Additionally, the bridging bound CO on Pt is the more quickly removed that the linearly bound CO species and is thus Pt bound CO species of greatest kinetic significance.

CHAPTER 1

INTRODUCTION

1.1 Fossil Fuels as Sources for Energy and Chemical Production

A large and increasing consumption of both energy and fossil fuels is a common characteristic shared among the developed countries. The conversion of fossil fuels to energy and value added products is a necessity for the high standard of living enjoyed in these countries. In 2011, the U.S.A. consumed 90 quadrillion Btu (QBtu) of energy from the combustion of fossil fuels. This constituted 82.0% of the total national energy consumption that year.[1] Despite the staggering amount of energy consumed by the U.S.A. every year, the demand for energy is constantly on the rise. The energy consumption for the U.S. has tripled since 1950, and is projected to continue to increase in the future.[1] An increasing demand for energy is not limited to the U.S.A., however. Global energy use is projected to increase by 56% between 2010 and 2040.[2] Half of this increase is attributed to the China and India, two countries that are rapidly becoming industrialized nations.

In the U.S.A. in 2011, the consumption of transportation fuels was one of the largest subsets of domestic energy consumption at 27.8% of the total annual energy consumption. While the other major sectors of energy consumption, such as industry, commercial, and residential can utilize electricity generated from stationary power plants, the transportation sector is almost completely reliant on petroleum derived liquid transportation fuels. In fact, 70.2% of the 18.84 million barrels per day (MMbpd) consumed by the U.S. was eventually consumed by the transportation sector.[1] Although the majority of the petroleum imported into the U.S.A. is eventually converted into liquid transportation fuels, transportation fuels are not the only valuable products derived from

petroleum. In 2011 The U.S.A. also produced 8.2 MMbpd of refined petroleum products other than transportation fuels, such as asphalt, waxes, special napthas, and petrochemical feedstocks. While the importance of transportation fuels to modern society is evident, the importance of the petrochemical feedstocks must not be overlooked. These chemical pools are the precursors to the majority of the polymers, plastics, and specialty chemicals that comprise the products and technologies that improve our standard of living.

While the dependence of a modern economy on fossil fuels for energy and chemical production is generally accepted, the availability, price, and environmental implications of the continued use of these resources are much less understood. Although the exact amount of crude oil and other fossil fuels reserves has been a hotly debated topic for decades, the finite supply of these resources is certain.[3] The U.S.A. has significant reserves of coal and natural gas.[1] However, the domestic supply of crude oil has been significantly less than the consumption for at least the last 60 years (Figure 1.1).[1] Consequently, the continued vitality of the U.S.A.'s economy is dependent on foreign sources of crude oil. This dependence is the basis for the geo-political issues associated with interest in foreign oil supply and why finding a domestically available replacement has become a matter of national security.[1] The finite global crude oil reserves has more profound implications than that of domestic reserves. As the global demand for petroleum products increases, particularly due to the growth in developing countries, and the global supply eventually decreases, the price of petroleum products is expected to continue to increase in the future. This will have an immense impact on the global economy, and the quality of life enjoyed by nearly every person on the planet. In order to avoid the dramatic and negative impacts to society associated with rapidly

increasing oil prices, sustainable replacements for petroleum derive products must be developed in the near future.

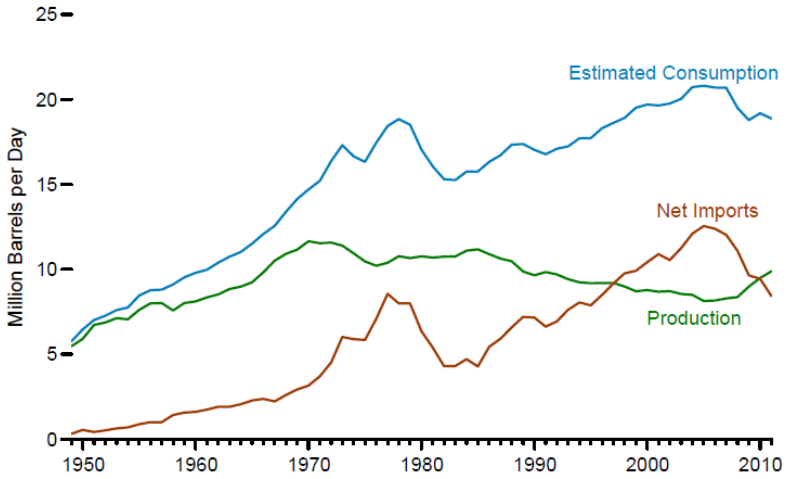

Figure 1.1 Recent trends in crude oil consumption, import, and production in the U.S.A.[1]

Increasing energy and chemical prices due to limited availability is not the only drawback of the continued use of fossil fuels. The utilization of fossil fuels, either through combustion or chemical conversion, inevitably results in the release of CO_2. CO_2 is perhaps the most infamous greenhouse gas, and is the leading contributor to global warming.[4] Global warming causes increased severity and decreased predictability of severe weather events, such as hurricanes and droughts. As shown in Figure 1.2, the global average concentration of CO_2 has been increasing at an extraordinarily fast since the start of the industrial revolution in the mid-19th century.[5] This change is coupled with an increase in the average global temperature. Neither of these trends are expected to decrease in the near future without a dramatic decrease in anthropogenic CO_2 production

and as a result weather events that are detrimental to human life and agricultural productivity are expected to increase in both severity and frequency.

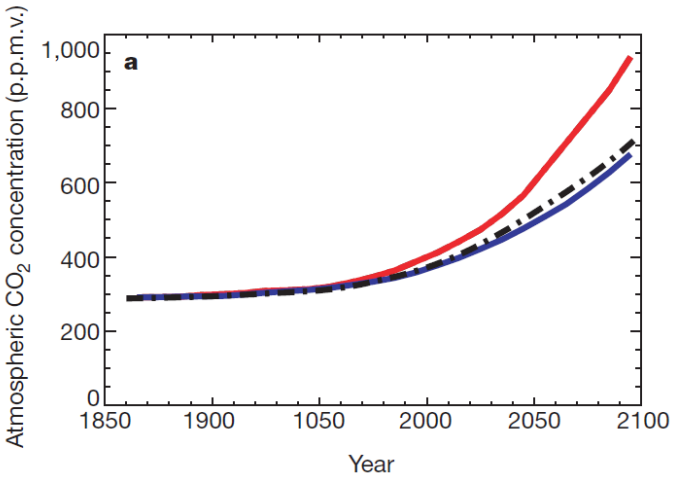

Figure 1.2 Global mean CO_2 concentration predictions that include dynamic amounts of atmospheric CO_2 and terrestrial vegetation (red), dynamic CO_2 concentration and fixed vegetation (dashed), and a model that neglects CO_2 induced climate change (blue).[5]

Artificially increased levels of atmospheric CO_2 due to anthropogenic sources are also expected to have deleterious effects to oceanic ecosystems. The increase in average ocean temperature caused by global warming will accelerates the bleaching of coral reefs.[6] The earth's oceans are one of the largest terrestrial carbon sinks. The oceans naturally absorb CO_2 in the form of carbonic acid and become increasingly acidified as the atmospheric CO_2 concentration increases. The increasing acidity in the ocean can both kill living coral colonies and dissolve the carbonate based reef structure.[7] As coral reefs are an essential building block the oceanic food chain, the recent damage to coral reefs due to climate change are a threat to a significant portion of the global food supply. Furthrmore, these ecosystems are some of the most biodiverse found on earth[7] and on

that distinction alone merit protection. All of the potential negative side effects of increased global CO_2 concentration dictate that petroleum products, and fossil fuels in general, be replaced by sources that can be utilized in a carbon neutral manner.

Since a steady supply of liquid transportation fuels and other petroleum derived products have been essential to a healthy economy for decades, the associated chemistry and chemical engineering challenges have been heavily investigated for decades as well, and are now well established. Natural gas, coal, and crude oil are the three most utilized fossil fuels both globally and in the U.S.A.. These fossil fuels and are largely made up of hydrocarbons. The low concentration of heteroatoms, such as O, N, S, and thus functional groups as well, in these fossil fuels makes them insoluble in water, generally. Natural gas has a molar hydrogen to carbon ratio (H/C) of 4, contains no O and is very commonly burnt as a fuel source. Natural gas is also the primary industrial feedstock for hydrogen production via steam reforming over a heterogeneous catalyst.[8]

Coal can have varied H/C and oxygen to carbon (O/C) ratios depending on the type; anthracite typically has a H/C ratio of < 0.5 and has an O/C ratio of < 0.1 whereas lignite has a H/C ratio of ca. 1 and an O/C ratio of ca. 0.35. [9] Coal is very mostly burned for energy production, but can be converted to other chemicals including liquid transportation fuels. The primary means of chemically upgrading coal include gasification followed by Fischer-Tropsch synthesis, pyrolysis, solvent extraction, and hydroliquifaction.[8]

Crude Oil is perhaps the most chemically diverse fossil fuel available, as it typically contains from 10,000 to 100,000 chemically distinct compounds, depending on the source.[10] Generally, crude oil has H/C and O/C ratios of ca. 1.75 and < 0.05,

respectively,[9] which lead to its relatively high heating value. However, it is the chemical diversity of crude oil that sets it apart from the other fossil fuels. The diverse set compounds found in crude oil enable it to be transformed into not only liquid transportation fuels but also the myriad petrochemical compounds found in virtually every item that humans interact with on a daily basis. Decades of research and development have led to the development of heterogeneously catalyzed chemical processes for oil refining on an industrially viable scale. Heterogeneous catalysts are central to many processes in petroleum refining, including: alkylation, catalytic cracking, hydro-cracking, hydrodesulfurization, hydrotreating, isomerization, polymerizing, reforming, and sweetening (Figure 1.3).[11] As was the case with fossil fuels, developing industrially viable heterogeneous catalytic methods for the production of energy, transportation fuels, and petrochemical feedstocks from biomass will require many years of intensive research and development, and the financial investment to do so.

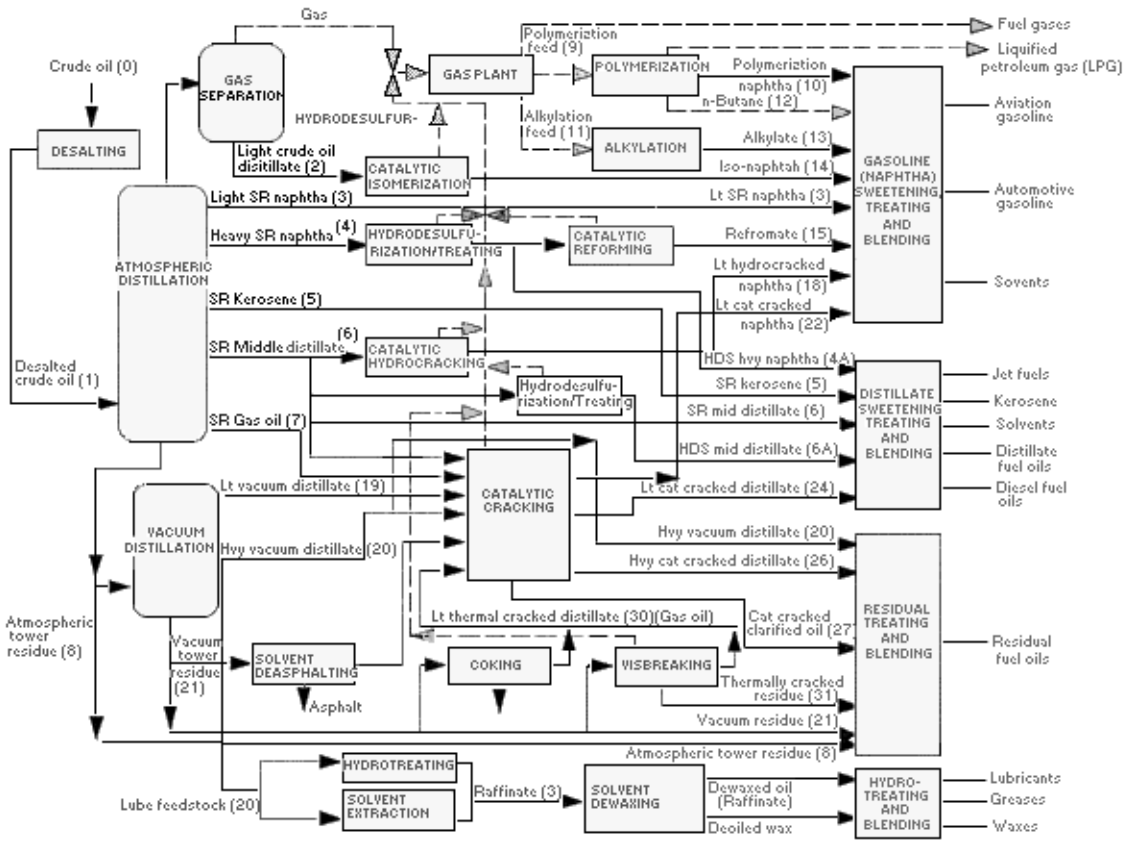

Figure 1.3 A simplified flow diagram of a typical crude oil refinery optimized for the production of transportation fuels including various heterogeneously catalyzed processes.[11]

1.2 Biomass as a Replacement for Fossil Fuels and Chemical Feedstocks

Biomass is heralded as one of the most promising replacements for fossil fuels as for several reasons. First, biomass is abundant enough both domestically and globally that its utilization poses to make a real impact. The U.S.A. is capable of producing 3.8 x 10^9 barrels of oil energy equivalent (boe) of biomass per year, 54% of the U.S.A.'s annual oil consumption, without impacting the current agricultural food production.[12] Additionally, Europe, Africa, and Latin America could combine to produce an additional 8.1 x 10^9 boe annually.[12] Second, biomass can be grown in a sustainable fashion. If an appropriate

energy crop is utilized in a given agricultural environment, it does not require significant irrigation or fertilization, which makes the crop largely carbon neutral.[13-15] As a result, the use of the energy crop has a minimal net contribution to global CO_2 levels and can maintain a favorable energy output to input ratio. Finally, many studies have already demonstrated that various biomass sources can be upgraded through thermal and/or chemical means to transportation fuels or chemicals.[12,15-18]

Although biodiesel and ethanol are currently perhaps the two most recognized biofuels, they both have limitations to further widespread utilization. Biodiesel can be produced from the trans-esterification of waste triglyceride sources, such as used cooking oils. [14,15] Unfortunately, these sources are relatively limited in quantity. Biodiesel can also be produced from virgin vegetable oils, such as rape seed oil or soybean oil, but this both makes the process economically unfavorable and creates issues regarding the competition of foodstuffs versus transportation fuels.[15] Ethanol produced in the U.S.A. for use as a supplement in motor gasoline is primarily derived from the enzymatic hydrolysis of corn starch to sugars, followed by the fermentation of the sugars by yeast to ethanol.[13] The fermentation and subsequent distillation steps in this process are very energy intensive and make the entire process suffer from an energy output to input ratio that is arguably greater than 1.[19]

The next and most promising generation of biofuels and biomass derived chemicals are derived from lignocellulosic biomass. Lignocellulosic biomass is the structural component of biomass primarily consisting of cellulose, hemicellulose, and lignin (Figure 1.4).[12] This "woody" biomass is not a foodsource for humans, and thus avoids many ethical issues regarding agricultural versus industrial land use competition.

Additionally, lignocellulosic biomass can come from energy crops purposefully planted for conversion to value added products, and it can also come from waste biomass sources such as used lumber, food waste, or yard waste. As a result, lignocellulosic biomass is an extremely accessible and low cost source of biomass.[19]

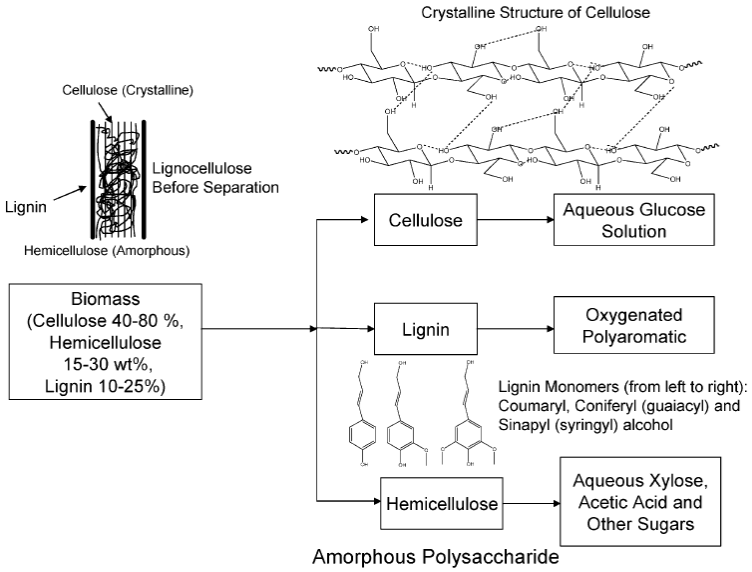

Figure 1.4 The three major macromolecules of lignocellulosic biomass and the natural chemical intermediates they can be transformed into.[12]

As shown in Figure 1.4,[12] the typical constituent molecules of lignocellulosic biomass are polymers made up of carbohydrate monomers. Cellulose consists of a crystalline arrangement of glucose monomers bonded via β-1→4 linkages. Hemicellulose is an amorphous molecule comprised of five and six carbon sugars bonded in various ways. Lignin is also amorphous, and is made up of many different phenolic monomers.[12] The large amount of oxygen containing functional groups, including alcohols, carbonyls, and organic acids, contained in these polymers give them distinctly different properties than the hydrocarbon pool that comprises crude oil.[17] Being partially oxidized, these

biomass derived oxygenate molecules have a much lower heating value than a hydrocarbon of comparable molecular weight.[20] Consequently, if these molecules are to be used as a fuel source, they require catalytic upgrading to lower their O/C ratio.[21]

An additional consequence of the large number of oxygen functional groups found in lignocellulosic biomass is that the constituent molecules tend to be polar and are commonly water soluble. The polarity of the molecules leads to low vapor pressures. As a result, water is the natural solvent for the chemical conversion of such biomass derived oxygenate compounds. Using water as a reaction medium for the conversion of biomass derived oxygenates lends the process many benefits over other common industrial solvents that tend to be expensive, carcinogenic, and are commonly reactive or flammable. Water is an abundant and environmentally benign solvent. Its abundance also makes it relatively inexpensive which adds to the economic viability of any process that utilizes water as a solvent.

The presence of the oxygen containing functional groups also makes these molecules reactive at moderately elevated temperatures. Specifically, they are prone to polymerization and condensation reactions at elevated temperatures. This property combined with the large concentration of functional groups found in biomass can result in an incredibly complex product mixture if even a few side reactions occur in an upgrading process. Consequently, developing catalytic methods with sufficient selectivity toward a small number of desired products is one of the greatest challenges facing biomass upgrading today.[17]

1.3 Current Understanding of the Heterogeneously Catalyzed Conversion of Biomass Derived Oxygenates in Aqueous Phase

Aqueous phase processes that utilize acidic, basic, metal, or metal oxide catalysts have been demonstrated to have potential for upgrading carbohydrates derived from various biomass sources, including lignocellulosic carbohydrates.[12,15,17,22] Additionally, multi-phase systems that utilize an aqueous phase for reaction with a solid catalyst and an organic phase for product extraction have also been shown to be effective.[17] Generally, the first step in upgrading lignocellulosic carbohydrates is the acid catalyzed hydrolysis of macromolecules such as cellulose and hemicellulose into smaller polymers, or their constituent monomers. Although mineral acids and enzymes can be used to hydrolyze these carbohydrates with favorable conversion and selectivity, respectively, they suffer from poor recoverability and activity, respectively, when compared to heterogeneous catalysts. Solid acids including various zeolites and metal oxides are capable of hydrolyzing carbohydrate polymers. While solid bases can be used for hydrolysis reactions, they tend to cause more side reactions than solid acids and are thus less commonly used.[23]

Many reaction studies have demonstrated that various heterogeneous catalysts can be used for different types of biomass upgrading reactions depending on the specific properties of the catalyst. As mentioned previously, solid acids like many zeolites and certain metal oxides, such as γ-Al_2O_3, Nb_2O_5, CeO_2, and ZrO_2 are capable of catalyzing hydrolysis reactions. Many solid acid catalysts are also effective at catalyzing dehydration reactions, which are important for alkene formation and elimination of oxygen atoms from sugars.[17] Solid bases, such as MgO, and CeO_2, ZrO_2, can be used for

catalyzing isomerization reactions, for example the isomerization of glucose to fructose.[17,24,25] Solid bases are also used to catalyze aldol condensation reactions between a carbonyl group with an α hydrogen, and another carbonyl group. Although solid acids can also be used to promote this chemistry, solid bases are more effective at abstracting the α hydrogen from a carbonyl group in the first step of this reaction.[17] Supported metal catalysts, like Ni, Pt, Pd, and Ru are essential to hydrogenation, hydrogenolysis, and selective oxidation chemistries. Using a reaction scheme with sequential reactors which contain different catalysts, or a single reactor with a multi-functional catalyst enable the production of various value added chemicals and chemical intermediates from glucose (Figure 1.5).[17]

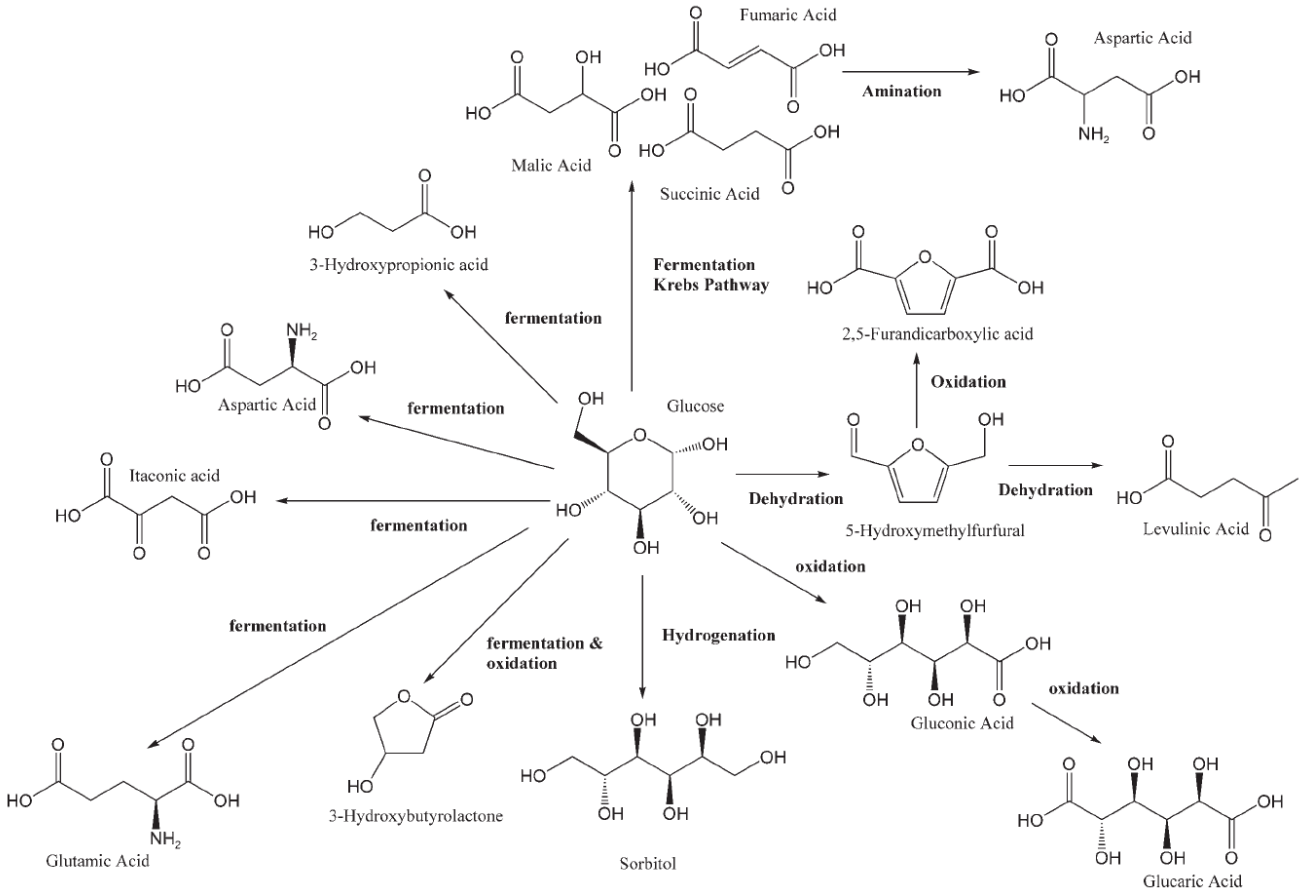

Figure 1.5 Value added products and chemical intermediates that can be derived from glucose via fermentation and catalytic routes.[17]

Aqueous phase reforming (APR) is a particularly promising reaction scheme comprised of several types of reactions that result in the production of H_2 and/or alkanes from carbohydrates depending on the conditions and the supported metal catalyst used. C—C bond cleavage, C—O bond cleavage, dehydration, hydrogenation, and aldol condensation reactions are central to aqueous phase reforming reaction schemes (Figure 1.6).[26] Consequently, supported metal catalysts on acidic metal oxide or zeolite supports are the most common catalysts for aqueous phase reforming of carbohydrates. When supported metals that preferentially cleave C—C bonds, including Pt or Pd, are utilized, the carbohydrate reactants are cleaved, and subsequent water gas shift reactions occur to produce H_2 and CO_2.[26] When metals that preferentially cleave C—O bonds of carbohydrates, such as Ni or Ru, are used in aqueous phase reforming reactions in conjunction with a source of H_2, alkanes are formed preferentially rather than H_2 and CO_2.[17] When straight chain polyols undergo aqueous phase reforming, repeated cycles of sequential dehydration and hydrogenation reactions occur to produce straight chain akanes that are useful in liquid transportation fuel pools. When glucose undergoes aqueous phase reforming with such catalysts, a series of dehydration, hydrogenation, and aldol condensation reactions occur which eventually result in the production of a 9, 12, or 15 carbon long alkane.[27] Hydrogen must be supplied in order to promote the hydrogenation reactions required to form the alkanes and can be produced in situ from a limited amount of reforming reactions, or can be supplied externally via H_2 gas.

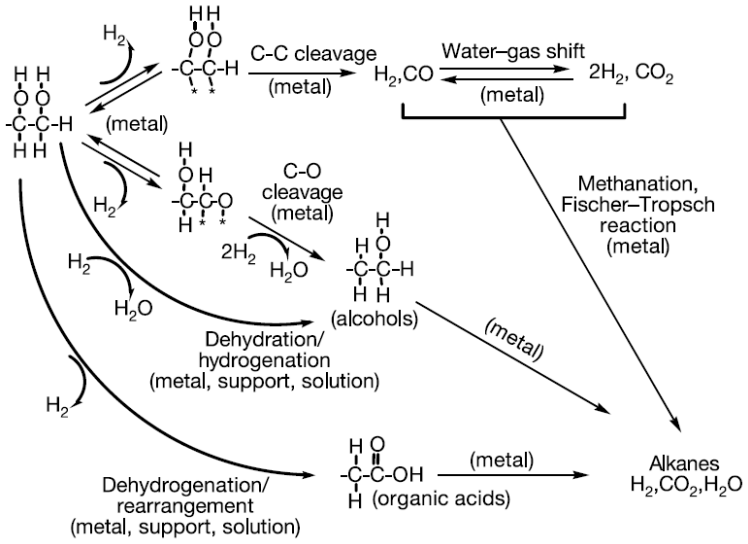

Figure 1.6 Aqueous phase reforming reaction pathways for the production of H_2 and alkanes from polyols.

Although many of the reaction schemes for the aqueous phase conversion of biomass using heterogeneous catalysts have been explored, a detailed understanding of the surface chemistry of such systems is sorely lacking. As the surface chemistry of a molecule on a solid catalyst ultimately dictates the overall performance of the catalyst, an in-depth knowledge of the surface chemistry of biomass molecules on heterogeneous catalysts is central to the efficient design of active and selective catalytic processes for such chemistries. An analogous understanding of the surface chemistry of crude oil derived molecules was essential to the development of catalysts for oil refining.[28] Additionally, a number of studies have shown that the presence of aqueous phase biomass molecules can enhance the stability of metal on γ-Al_2O_3 catalysts against hydrolytic attack and subsequent conversion to boehmite, although the exact reason for the enhanced stability is not fully understood.[29-31] A major reason for the lack of knowledge in this area of surface science is that the physical properties of most biomass

derived carbohydrates present a challenge for studying their surface behavior on heterogeneous catalysts.

Many commonly utilized methods for studying the surface chemistry of molecules, such as in situ transmission infra-red (IR) spectroscopy, nuclear magnetic resonance (NMR) spectroscopy, high resolution energy electron loss spectroscopy (HREELS), x-ray photoelectron spectroscopy (XPS), or Auger electron spectroscopy (AES) typically require dosing the molecule being studied via vapor phase onto an otherwise adsorbate free surface often under a vacuum environment. Since most biomass derived carbohydrates have little to no vapor pressure,[20] such dosing methods are inadequate. Additionally, since the surfaces being studied, and the experimental apparatuses, must remain free of adsorbed water or other bake-out resistant molecules, understanding the effects of an aqueous reaction environment on the surface chemistry of such systems is exceedingly difficult, if not impossible.

Despite the challenges associated with studying the surface interactions of biomass and heterogeneous catalysts, there are a limited number of studies that have provided insight on the subject. A series of studies largely based on the adsorption behavior of multi-functional oxygenates, including polyols, on high Si/Al ratio hydrophobic zeolites determined that dispersive forces dominate the molecule-surface interactions for these materials.[32,33] Additionally, these studies also found than an increasing number of hydroxyls in the adsorbate molecule decreased adsorption, and the position of the hydroxyls within the adsorbate molecule have little influence on surface interactions or uptake. However, adsorption of polyols on a hydrated Al_2O_3, a material with comparatively larger pores and a more hydroxylated surface, is very dependent on

hydroxyl position.[34] Interactions between alkanediols and CeO_2 are speculated to be dominated by acid/base interactions between the hydroxyl groups of the alkanediol and the coordinatively unsaturated (CUS) surface metal atoms of CeO_2.[35] A density functional theory (DFT) study of the surface interactions of ethylene glycol with basic metal oxides found that ethylene glycol interacts with the CUS magnesium atoms of MgO through both of its alcohol groups via acid/base, non-dissociative, interactions.[36] Phenolic molecules are known to preferentially interact with acidic CUS surface metal atoms when available via their hydroxyl group rather than interacting with surface hydroxyls of metal oxides. [37]

Studies that directly observe interactions between biomass derived oxygenates and heterogeneous catalysts in an aqueous medium are very rare. In situ ATR-IR studies of the aqueous phase reforming of various alcohols over metal oxide supported Pt catalysts have provided evidence that even in an aqueous medium, linear and bridging CO and hydrogen are all coadsorbed on the Pt metal particles during reaction.[38,39] The temperature required to initiate such reactions is not fully agreed upon. Additionally, the effect of coadsorbed species, like hydrogen, oxygen, or CO_2 on observed reaction dynamics are not fully understood.[38,40-42]. Consequently, new and robust methods for studying the interactions of biomass derived carbohydrates and heterogeneous catalyst surfaces in the presence of coadsorbed water must be developed and utilized in order to facilitate the design of catalysts for efficient and effective biomass upgrading reaction systems.

1.4 Objectives and Organization

The overall objective of this body of work is to develop and utilize experimental methods for studying the surface interactions of biomass derived oxygenates and heterogeneous catalysts, as well as the role of water on such interactions. This knowledge will help to bridge the gap between the largely empirical knowledge of which catalysts happen to work well for certain systems and the largely unanswered question of why one catalyst behaves differently than another. As discussed previously, this knowledge will be essential to the rational design of catalyst systems for biomass upgrading reactions in the future. More specifically, biomass derived polyols of both industrial and academic relevance will be utilized. These molecules are functionally very similar to the majority of biomass derived carbohydrates, including sugars. As a result, the knowledge gained from the molecules used in the present work will be very relevant for many other biomass derived carbohydrates of interest.

In Chapter 2, aqueous phase adsorption isotherms, ^{2}H solid echo pulse NMR spectroscopy, DFT modeling and in situ high vacuum (HV) transmission IR spectroscopy are used to investigate the surface interactions of two and three carbon polyols with γ-Al_2O_3. Additionally, the role of bulk, coadsorbed water on the formation or removal of certain molecule-surface interactions is investigated. Specifically, ethylene glycol, 1,2-propanediol, 1,3-propanediol, and glycerol are studied. The diols are used in conjunction with glycerol in order to provide information regarding the importance of hydroxyl position on polyol-metal oxide interactions. Glycerol is used because it is functionally similar to sugars, it has been heavily studied in the APR literature, and it is of industrial

relevance as the main byproduct of biodiesel production.[43] Additionally, ethylene glycol is of industrial relevance as it is the main additive in automotive antifreeze.

In Chapter 3, in situ HV transmission IR spectroscopy and various catalyst physicochemical characterization techniques are used to elucidate how glycerol bonds to several different metal oxides. The role of coadsorbed, bulk water on such interactions will again be explored. The oxides studied include, a basic surface enhanced γ-Al_2O_3, TiO_2 anatase, a synthesized ZrO_2, a commercial ZrO_2, CeO_2, and MgO. The oxides used provide a wide array of surface acid site and basic site types, strengths, and concentrations. This variety of surface sites allows for discovering which sites are those active for the formation of glycerol-metal oxide interactions. The range of metal oxides used provides information on which properties of a metal oxide dictate the degree of activation of the C—O bonds of a metal oxide bound glycerol surface species.

In Chapter 4, attenuated total reflection infra-red spectroscopy (ATR-IR) is used to discover the surface intermediates of kinetic relevance in the APR of glycerol over a Pt/γ-Al_2O_3 catalyst and asses the dynamics of their formation and conversion. First, an effective and reproducible catalyst cleaning/pretreatment is established so that subsequent APR studies can be carried out. The exact identity of various Pt bound CO species are elucidated. The effect of Pt bound hydrogen or oxygen, as well as carbonaceous impurities on apparent CO formation dynamics are explored. An optimized cleaning/pretreatment procedure is used to observe the maximum CO formation rate and provide spectroscopic evidence of the rate limiting step in the APR reactions of glycerol. Finally, evidence of the rate limiting water-gas shift removal of Pt bound CO occurring at room temperature is obtained.

CHAPTER 2

SURFACE INTERACTIONS OF C_2 AND C_3 POLYOLS WITH γ-Al_2O_3 AND THE ROLE OF COADSORBED WATER.

2.1 Background

The general acceptance of the finite nature of crude oil has created a driving force for the development of renewable replacements for petroleum derived chemicals.[44] Additionally, growing concern over CO_2 emissions suggests that these alternative feedstocks should be carbon neutral.[45] All of these requirements are fulfilled by biological feedstocks.[16] The use of an aqueous medium for conversion of biomass derived platform molecules is attractive because water is a plentiful, affordable, and green solvent, and many biomass derived oxygenates are soluble in water.[20]

Heterogeneous catalysts are promising for biomass upgrading because they are generally more easily recovered than homogenous catalysts. As a result, there is a growing body of research dedicated to the development of heterogeneous catalytic processes for aqueous phase conversion of biomass to value added products.[15,17,22] Metal oxides are commonly used as supports for noble metal catalysts, and are also often used as solid acid or solid base catalysts.[28] Specifically, γ-Al_2O_3 is a very common solid acid catalyst and noble metal support, and has already been used in a number of biomass conversion studies.[38,46,47]

Ultimately, the performance of a heterogeneous catalyst is dependent on the formation and conversion of surface species during reactions. It is for this reason that

understanding the surface chemistry of petroleum derived molecules on catalytic surfaces was essential to the development of efficient catalytic processes in oil refining.[28] Similarly, understanding the interactions between biomass derived molecules, water, and catalytic surfaces will be central to the development of effective catalysts for aqueous phase biomass upgrading.[48,49] In situ high vacuum (HV) or ultra-high vacuum (UHV) infrared (IR) spectroscopy is widely used to monitor surface species on heterogeneous catalysts, including many metal oxides.[37,50,51] The low vapor pressure of most biomass derived oxygenates, however, requires adjustments of traditional surface science approaches.

Many existing experimental methods for studying surface interactions, including conventional in situ transmission IR spectroscopy, face major challenges for studying biomass derived oxygenates. These traditional methods require the reactant molecules to either be a gas or a liquid with a significant vapor pressure at moderate temperatures.[52-56] Most biomass derived oxygenates are either a liquid or solid with little to no measurable vapor pressure at room temperature (RT), and tend to decompose before volatilizing when heated.[20,57] Furthermore, traditional experiments begin by activating the metal oxide either under HV or a flowing dry gas and elevated temperatures to remove adsorbed water and other surface species. While interactions with water free surfaces are highly relevant for the conversion of hydrocarbons, the role of water as solvent, competitive sorbate, or possible reactant needs to be taken into account for the conversion of biomass derived oxygenates in aqueous phase. These effects have already been proven to be very influential on adsorption behavior and on the conformation of adsorbed species.[41,52,58] Consequently, established in situ IR spectroscopic methods for studying

the evolution of surface species on catalysts are insufficient for studying biomass derived oxygenates, and an alternative method needs to be used.

Interactions between biomass derived oxygenates and metal oxides are of clear importance when the metal oxide itself is the catalyst. However, interactions with a metal oxide whose main function is to support a metal catalyst is still of interest, as a number of studies suggest that support interactions can have an important effect on the overall reaction mechanism.[50,54,58,59] Also, recent studies have found that γ-Al_2O_3 supported catalysts are more stable in biomass solutions than they are in pure water at elevated temperature and pressure, although the mechanism by which the biomass stabilized the support is not fully understood.[30,31] As a result, the development of metal oxide based catalysts for the aqueous phase conversion of biomass molecules necessitates an understanding of how biomass molecules interact with metal oxide surfaces.

In this study, we elucidate the interactions between oxygenates, specifically polyols with two or three carbon atoms, and γ-Al_2O_3 using transmission IR, and nuclear magnetic resonance (NMR) spectroscopic techniques, as well as density functional theory (DFT) calculations. The influence of co-adsorbed water on these interactions is also investigated. The oxygenates examined are ethylene glycol, 1,2-propanediol, 1,3-propanediol, and glycerol.

2.2 Materials and Methods

2.2.1 Materials

>99.5% Ethylene glycol (EG), >99.9% 1,2-propanediol (1,2-PDO), 98% 1,3-propanediol (1,3-PDO), and 99% glycerol were purchased from Sigma Aldrich and were

used as received. γ-Al_2O_3 (99.5% metals basis) was purchased from Sigma Aldrich, was calcined at 500 °C for 4 h with 10 °C/min ramp rates under 100 ml/min air from a VWR 26000-020 zero air generator, and was stored in a dessicant jar. ZSM-5 (SiO_2/Al_2O_3 ratio of 30) was purchased from Zeolyst International and was used as received. (1,1,2,2,$^2H_4$)ethylene glycol (98% isotopic purity) and (1,1,2,3,3,$^2H_5$)glycerol (99% isotopic purity) were purchased from Cambridge Isotope Laboratories Inc. and were used as received. Deionized water was further purified using a Barnstead NANOpure ultrapure water system to 18.2 MΩ/cm.

2.2.2 Catalyst Characterization

X-ray diffraction (XRD) measurements were performed with a Philips X'pert diffractometer equipped with an X'celerator module using Cu Kα radiation. Diffractograms were collected at incident angles from 2θ = 5° to 70° with a step size of 0.0167°. Nitrogen physisorption measurements were performed with a Micromeritics ASAP 2020 Physisorption analyzer. Prior to analysis, samples were degassed under vacuum at 200 °C for 4 h. The BET surface area was calculated from the adsorption isotherm in the region $0.05 < P/P_0 < 0.3$,[60] and pore volumes were calculated using the BJH method.[61] Pyridine adsorption followed by IR spectroscopy was investigated using a Nicolet 8700 Fourier transform (FT) IR spectrometer with a MCT/A detector. For each spectrum, 128 scans were recorded with a resolution of 4 cm^{-1}. The γ-Al_2O_3 was pressed into a self-supported wafer and loaded into a custom built vacuum chamber (Figures A.1 and A.2). The catalyst wafer was activated at < 10^{-6} mbar and 500 °C for 12 h. The temperature was then lowered to 150 °C,[62] when the background spectrum was collected, and pyridine was introduced into the chamber at a pressure of 0.1 mbar for 30 min, the

time to reach adsorption equilibrium was less than 10 min. The chamber was then evacuated for 30 minutes, the time to reach desorption equilibrium was less than 15 min. The spectrum was then collected and the ν_{19b} mode[63] at 1450 cm^{-1}, indicative of pyridine coordinated with Lewis acid sites, was integrated, the ν_{8a} mode[63] had a frequency of 1616 cm^{-1}. The density of the wafer was obtained by weighing a cutout of the wafer with a diameter of 6.35 mm, after the experiment. The concentration of acid sites was calculated based on the integral of the peaks, the density of the wafer and the molar extinction coefficients reported by Datka et al.[50] ^{27}Al MAS-NMR measurements were carried out with a Bruker DSX 400 spectrometer. Zirconia rotors, 4 mm, were used and were spun at 12 kHz. The resonance frequency for ^{27}Al was 104.2 MHz. A $\pi/12$ pulse was used, and the recycling delay was 250 ms. For each spectrum, a minimum of 2400 scans were accumulated. Aqueous $Al(NO_3)_3$ was used as a reference compound (δ = 0 ppm).

2.2.3 Aqueous Phase Adsorption Isotherms

1.000 mL of EG, 1,2-PDO, 1,3-PDO, and glycerol solutions, ranging from 25 mM to 1000 mM, were combined with a known amount, ca. 0.100 g, of either γ-Al_2O_3 or ZSM-5. The resultant slurry was mixed by a vortex mixer for 30 s, placed in a sonication bath for 15 min, and then placed on a shaker table for 16 h. The slurries were then centrifuged for 20 min at 9000 rcf. The catalyst free solution, supernatant, was removed and analyzed via high performance liquid chromatography (HPLC) to determine the concentration of the oxygenate molecule after the adsorption period. The HPLC analysis was carried out on an Agilent 1260 Infinity HPLC, with a refractive index detector, RID, using a Grace Davison Prevail carbohydrate column. The mobile phase consisted of 75% acetonitrile and 25% water, and was flowed at a rate of 0.900 mL/min. The injection

volume used was 10 mL. The uptake was calculated using $U = \frac{(C_i - C_f)V}{M_{cat}}$, where U is uptake in mmol/$g_{catalyst}$, C_i is initial concentration of oxygenate solution in mM, C_f is final concentration of oxygenate solution in mM, V is volume of solution in L, and M_{cat} is mass of catalyst used in g.

2.2.4 Impregnation of γ-Al_2O_3 with Oxygenate Solutions for IR and NMR Spectroscopy.

The metal oxide was impregnated with aqueous solutions of the molecule of interest by mixing 250 mg of γ-Al_2O_3 with 5 ml of a solution of an oxygenate molecule in a 20 ml scintillation vial. The concentrations of oxygenate solutions used were chosen in order to deposit a desired amount of oxygenate on the γ-Al_2O_3 in order to achieve a desired loading (typically ranging from 0.25 wt% to 5.00 wt%) of the oxygenate after the bulk water was removed. The resulting slurry was mixed by a vortex mixer for 30 s, placed in a sonication bath for 15 min, and allowed to stand for 15 min. This mixing process was repeated 3 more times, for a total of 4 cycles. The vial was then placed in a vacuum desiccant jar, under vacuum for 15 min. The vial was then removed and allowed to warm to room temperature. The vacuum and warming process was repeated until the free water was removed, and only a visibly wet γ-Al_2O_3 paste remained. The vial was then allowed to completely dry in a desiccant jar at ambient pressure for 48h. The loadings ultimately used for analysis in the current study were chosen by analyzing different loadings. The loading used maximized the signal from adsorbed oxygenate molecules and minimized signals from bulk oxygenate molecules, as determined by the νCO region of the IR spectrum.

2.2.5 NMR Spectroscopy

^{2}H solid echo pulse sequence NMR analyses were carried out in a Bruker DSX 300 spectrometer. The samples were prepared using deuterium enriched molecules. The samples were analyzed in custom made glass sample tubes that were loosely sealed with PTFE tape. The ^{2}H resonance frequency used was 46.07 MHz. Two 90° pulses were applied separated by a 30 μs delay. Each pulse length was 3.8 μs. A recycle delay of 1 s was used. The number of scans acquired was 61,440. Samples were acquired at 25 °C in an environment of either ambient air (17% relative humidity) or flowing dry air at a rate of 1000 L/h. After switching from ambient air to dry air flow, samples were allowed to equilibrate for 12 h, and then the spectra were collected. Between switching from dry air flow to ambient air, the samples were removed from the spectrometer, and allowed to equilibrate with ambient air at 23 °C for at least 24 h before the samples were again analyzed.

2.2.6 IR Spectroscopy of Adsorbed Species

All spectra were collected with a Nicolet 8700 FT-IR spectrometer with a MCT/A detector. For each spectrum, 128 scans were recorded from 4000 cm^{-1} to 400 cm^{-1} with a resolution of 4 cm^{-1}. A self-built HV transmission IR chamber was used to control the environment to which the sample was exposed (Figures A.1 and A.2). Each sample was pressed into a self-supported wafer. The wafer was placed into the sample holder, which was then inserted into the transmission cell, and a spectrum was collected at room temperature and ambient pressure (RTP) utilizing a background which contained ambient air in the empty cell. High vacuum (HV), $< 10^{-6}$ mbar, was then applied to the cell, and a spectrum was collected when the pressure fell below 0.001 mbar. All spectra collected

while the cell was under HV utilized a background taken after HV was applied to the empty cell. After one hour spent under vacuum, a spectrum was collected, and then water vapor was dosed into the chamber through a leak valve until a pressure of 1.00 mbar was reached. This pressure of water vapor was maintained for 1 h, and then a spectrum was collected. After the desired rehydration period was completed, the sample was removed from the chamber, and a stamp was used to cut a circle sample from the wafer with a diameter of 6.35 mm. This disc was allowed to rest on the scale for ca. 1 h, until the mass reached a constant value. This was used to calculate the wafer area density.

The difference spectra were obtained using Thermo Fisher Scientific Inc. GRAMS 9.1. Spectra of γ-Al_2O_3 wetted with pure water, rather than an oxygenate solution, were collected according to the procedure described above. The spectrum of γ-Al_2O_3 impregnated with only water, at a given temperature and pressure, was then subtracted from the spectrum of the oxygenate impregnated γ-Al_2O_3 at the same temperature and pressure after normalization for any differences in sample wafer optical thickness. The resulting difference spectrum exhibits the differences that the presence of the polyol induced in the hydrated γ-Al_2O_3 spectrum while eliminating the majority of the unchanging signal from γ-Al_2O_3. A detailed description of the wafer optical thickness normalization procedure is in Appendix A.

2.2.7 DFT Calculations

All calculations were performed with plane-wave DFT[64] using the Vienna *ab initio* simulation package (VASP) with the PBE-GGA exchange-correlation functional[65] and the projector augmented wave (PAW) method.[66-69] To elucidate the role of the van der Waals interaction in this system, we also performed calculations using the PBE-D2

functional.[70] Reciprocal space was sampled only at the Γ-point due to the large supercell. Numerical tests with more *k*-points changed the calculated adsorption energies by less than 2%.[71] We adopted models for alumina surfaces from Ref.[72] According to this work, the (110) surface of γ-Al_2O_3 has the largest surface area among the surfaces present on the equilibrium crystal shape. The (110) surface has a hydroxyl coverage of 5.9 OH/nm^2 when γ-Al_2O_3 is prepared at 377-677 °C.[72] An illustration of this surface is shown in Figure A.3.

The reaction energy, ΔE, for surface reaction AB →A + B is calculated by ΔE = E_{total}(A+B/surf) - E_{total}(AB/surf),where E_{tot}(A+B/surf) and E_{tot}(AB/surf) are the total energies for co-adsorption of A and B and AB adsorption on the γ-Al_2O_3 surface, respectively.

For glycerol adsorption on the surface, various scenarios of molecular or dissociative adsorption were simulated. For each case, we considered numerous initial geometries. For brevity, however, only the most stable local minimum energy structures are presented. Further details pertaining to the various scenarios that were calculated can be found in Appendix A.

2.3 Results

2.3.1 Catalyst Characterization

The BET surface area of the γ-Al_2O_3 was 77 m^2/g. The BJH cumulative surface area of pores with a diameter between 1.7 nm and 300 nm based on the desorption branch of the isotherm was 50 m^2/g. The BJH cumulative volume of pores with a diameter between 1.7 nm and 300 nm based on desorption was 0.15 cm^3/g. The BJH average pore

diameter based on desorption was 12.1 nm. The average particle size as determined by N_2 physisorption was 78 nm. The Lewis acid site concentration according to pyridine adsorption followed by IR spectroscopy was 87 μmol/g. There was no measurable Brønsted acidity. The XRD diffractogram exhibited two main, broad peaks at 44.5° and 66.5° that are typical of γ-Al_2O_3 (Figure A.4).[73] The ^{27}Al MAS-NMR exhibited two main peaks at 63 and 7 ppm from Al atoms in tetrahedral and octahedral coordination, respectively (Figure A.5).[73] The tetrahedral and octahedral peaks comprised 31% and 69% of the total integrated peak area, respectively. These results are typical of commercially produced γ-Al_2O_3 and are similar to those used in previous studies.[30,31,48,73,74]

2.3.2 Aqueous Phase Adsorption Isotherms

The adsorption isotherms of the oxygenate molecules on γ-Al_2O_3 and ZSM-5 with a SiO_2/Al_2O_3 ratio of 30 were obtained in order to quantitatively assess how the oxygenate molecules of interest interact with γ-Al_2O_3 from a bulk phase perspective (Figure 2.1). ZSM-5 was used as reference for comparison with γ-Al_2O_3 as it is a very well-studied and characterized material.[75] The uptake of EG, 1,2-PDO, and 1,3-PDO on γ-Al_2O_3 are so small in the range investigated, 0 to 800 mM, that the uptake is difficult to measure. Glycerol has a small, but measurable uptake on γ-Al_2O_3 of approximately 0.18 $mmol/g_{catalyst}$ at an equilibrium concentration of 745 mM.

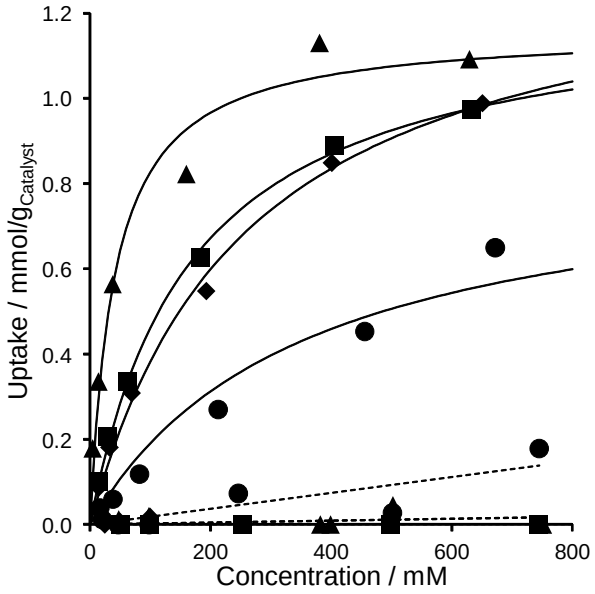

Figure 2.1 Aqueous phase adsorption isotherms of the oxygenate molecules on γ-Al_2O_3. Solid lines indicate adsorption isotherms of the molecules on ZSM-5, and dashed lines indicate adsorption isotherms of the molecules on γ-Al_2O_3. ♦ = EG, ■ = 1,2-PDO, ▲ = 1,3-PDO, and ● = glycerol.

By contrast, the uptake of all of the oxygenate molecules studied is much more significant on ZSM-5. 1,3-PDO had largest uptake, 1.1 mmol/$g_{catalyst}$ at an equilibrium concentration of 630 mM. EG and 1,2-PDO have very similar uptakes of about 0.99 mmol/$g_{catalyst}$ at an equilibrium concentration of 651 mM and 0.97 mmol/$g_{catalyst}$ at an equilibrium concentration of 633 mM, respectively. Glycerol has the smallest uptake of 0.70 mmol/$g_{catalyst}$ at an equilibrium concentration of 672 mM. It should be noted that the surface are of the ZSM-5 was ca. four times that of the alumina.

2.3.3 ^{2}H Solid Echo Pulse NMR

The ^{2}H NMR spectrum of 4.3 wt% (1,1,2,2,$^2H_4$)ethylene glycol on γ-Al_2O_3 after impregnation exhibits a single liquid like peak at 0 Hz (Figure 2.2 a). The same sample, after having been exposed to an extended period of dry air flow exhibits both a liquid like

peak at 0 Hz and a Pake pattern with a width of ca. 2400 Hz (Figure 2.2 b). The Pake pattern indicates that the molecule experiences significantly reduced mobility relative to pure EG or EG dissolved in water.[76] In the current study, the Pake signal indicates a hindered mobility due to interactions with the γ-Al_2O_3. After the sample was allowed to equilibrate with ambient air (Figure 2.2 c), its spectrum still exhibited both the sharp peak that is characteristic for liquid samples and the Pake signals, although the Pake signal is much weaker when compared to the spectrum of the sample under dry air flow (Figure 2.2 b).

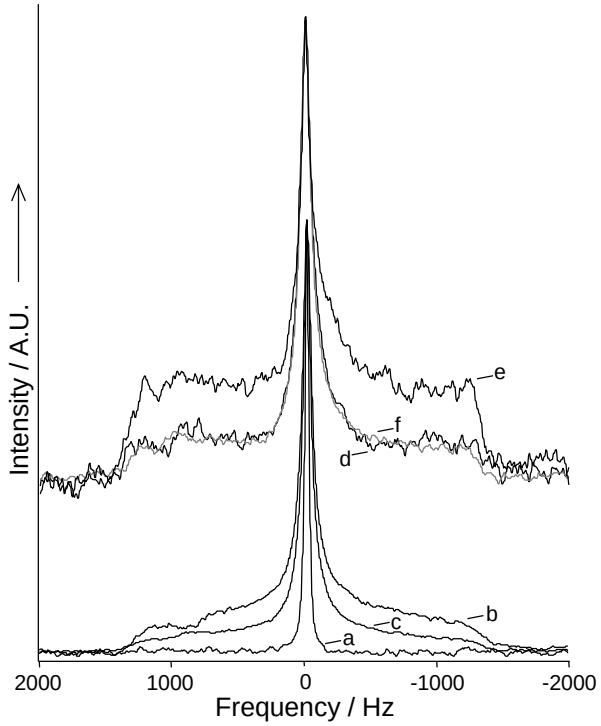

Figure 2.2 ^{2}H NMR of 4.3 wt% (1,1,2,2,$^2H_4$)EG on γ-Al_2O_3 (a, b, c) and 1.3 wt% (1,1,2,3,3,$^2H_5$)glycerol on γ-Al_2O_3 (d, e, f). Samples were subjected to flowing ambient air (a and d), followed by flowing dry air (b and e), followed by flowing ambient air again (c and f, f shown in grey for clarity).

The ^{2}H NMR spectrum of 1.3 wt% (1,1,2,3,3,$^{2}H_5$)glycerol on γ-Al_2O_3 after impregnation exhibits a sharp peak at 0 Hz and a Pake pattern with a width of ca. 2440 Hz (Figure 2.2 d). During extended dry air flow over the sample, both the sharp peak at 0 Hz and the Pake pattern are visible. However, the intensity of the Pake pattern increased significantly (Figure 2.2 e). After equilibration with ambient air for 24 h the spectrum also exhibited a sharp peak at 0 Hz and a Pake pattern (Figure 2.2 f). The intensity of the Pake pattern relative to the liquid like peak is essentially identical to the spectrum of the sample after impregnation (Figure 2.2 d).

2.3.4 IR Spectroscopy

2.3.4.1 Interactions with OH Groups of γ-Al_2O_3 via IR Spectroscopy

Figure 2.3 shows the νOH region of the IR spectra of different oxygenate molecules on γ-Al_2O_3 under various conditions, as well as the νOH region of the spectrum of pure γ-Al_2O_3. The spectrum of the pure γ-Al_2O_3 exhibits several peaks due to νOH modes of various surface OH groups at 3772, 3730, 3700, 3560 cm^{-1}, and very broad, sloping shoulder below 3560 cm^{-1} attributed to surface OH groups involved in hydrogen bonds (Figure 2.3 a). At RTP, all of the difference spectra of samples loaded with the different oxygenate molecules exhibit negative peaks at 3772 and 3700 cm^{-1}, as well as a positive peak at ca. 3475 cm^{-1} that partially obscures a very broad, negative peak that ranges from ca. 3700 to 2800 cm^{-1} (Figure 2.3 c, e, g, i). The broad, negative peaks ranging from 3700 to 2800 cm^{-1} are attributed to the displacement of water on the sample by the biomass molecule relative to the subtracted spectrum, which was only impregnated with water. The positive peaks at 3475 cm^{-1} are attributed to hydrogen

bonding interactions that occur between water and the biomass molecules. At room temperature and high vacuum (RTHV), the spectra of all of the different oxygenate loaded samples (Figure 2.3 b, d, f, h) exhibited negative peaks at several frequencies attributed to OH groups of γ-Al_2O_3, including 3772, 3730, and 3700 cm^{-1}. A very broad, positive peak at ca. 3175 cm^{-1}, also became evident and is attributed to hydrogen bonding OH groups formed between the respective polyol and the γ-Al_2O_3 surface.

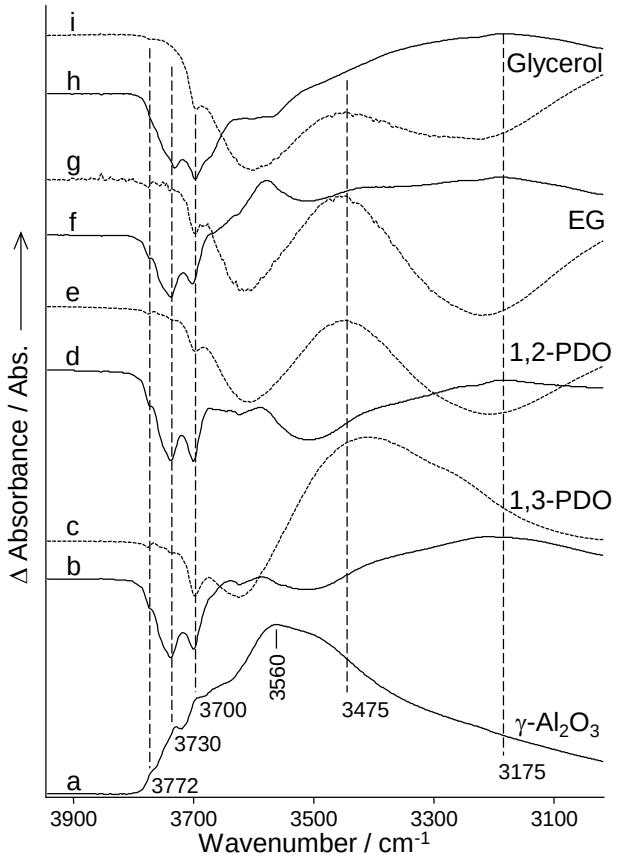

Figure 2.3 IR spectra of pure γ-Al_2O_3 and difference spectra of oxygenate molecules on γ-Al_2O_3 with the γ-Al_2O_3 spectrum subtracted. Solid lines indicate samples under HV at RT. Dotted lines indicate samples at RTP.

2.3.4.2 Ethylene Glycol on γ-Al_2O_3

Figure 2.4 shows the νCH region (3000-2600 cm^{-1}), as well as the νCO region (1200-1000 cm^{-1}) of 4.3 wt% ethylene glycol (EG) on γ-Al_2O_3 under various conditions. These regions are shown for each molecule in this study as they contain the most significant changes observed in all of the various spectra. The most significant IR spectral features for all molecules studied, both pure and on γ-Al_2O_3, can also be found in Table A.1. Pure EG exhibited $\nu_{asym}CH_2$ and $\nu_{sym}CH_2$ modes at 2937 and 2874 cm^{-1}, respectively, as well as $\nu_{asym}CO$ and $\nu_{sym}CO$ modes at 1083 and 1033 cm^{-1}, respectively (Figure 2.4 a).[77] In the spectrum of 4.3 wt% EG on γ-Al_2O_3 at RTP (Figure 2.4 b), the $\nu_{asym}CH_2$ signal broadened and the $\nu_{sym}CH_2$ mode split into a peak at 2879 cm^{-1} with a very weak shoulder at 2850 cm^{-1}. The νCO region displayed blue shifts of 12 and 25 cm^{-1} in the $\nu_{asym}CO$ and $\nu_{sym}CO$ modes to 1095 and 1058 cm^{-1}, respectively, as well as the development of a weak, broad peak at 1131 cm^{-1}.

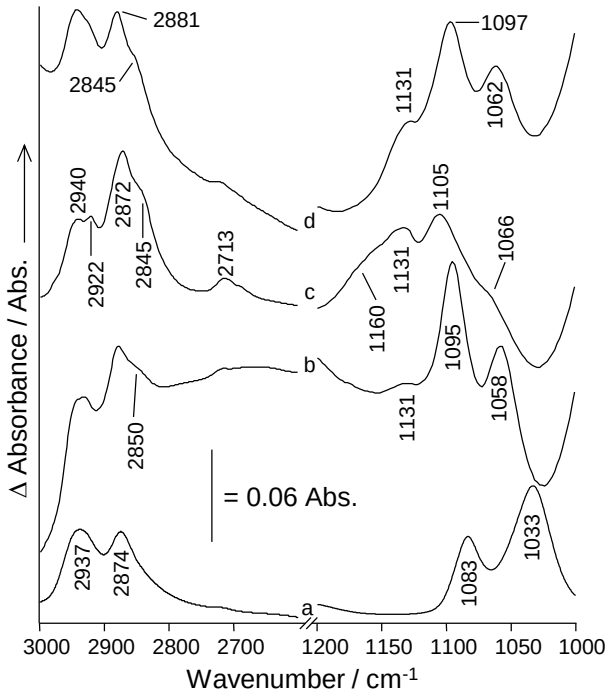

Figure 2.4 IR spectra of liquid EG and EG on γ-Al_2O_3. Liquid EG, a. EG on γ-Al_2O_3 at RTP, b. EG on γ-Al_2O_3 after 1 h spent at RTHV, c. EG on γ-Al_2O_3 after 1 h spent at 1.00 mbar of H_2O vapor, d. Spectra b-d are difference spectra in which the spectrum of γ-Al_2O_3 was subtracted from the EG loaded sample.

When the 4.3 wt% EG on γ-Al_2O_3 had been under HV at RT for 1 h, the νCH region showed further splitting of the previously described peaks (Figure 2.4 c). The $\nu_{asym}CH_2$ fundamental split into 2 peaks at 2940 and 2922 cm^{-1}, and the $\nu_{sym}CH_2$ mode showed a main peak at 2872 cm^{-1} with a shoulder located at 2845 cm^{-1}, which is much more pronounced than when at RTP. Additionally, a new peak arose at 2713 cm^{-1}. The HV treatment also caused significant changes in the νCO modes. The peak at 1131 cm^{-1} grew in intensity into a clearly resolved peak, and the previous peaks at 1095 and 1058 cm^{-1}, shifted to 1105 and 1066 cm^{-1}, respectively. Also, the peak at 1066 cm^{-1} lessened in intensity. A new, broad shoulder at 1160 cm^{-1} also became evident.

The introduction of 1.00 mbar of gaseous water to the sample after the HV period (Figure 2.4 d) broadened the $\nu_{asym}CH_2$ peaks at 2940 and 2922 cm^{-1} relative to when the sample was under HV. As a result, these peaks became less resolved. The $\nu_{sym}CH_2$ peak and shoulder exhibited slight blue shifts induced by the water vapor exposure, and were apparent at 2881 and 2850 cm^{-1}, respectively. The peak at 2713 cm^{-1} became less resolved, but was still resolved. The water vapor exposure caused the νCO modes observed under HV to return to a state that was nearly identical to those observed at RTP, two main peaks at 1097 and 1062 cm^{-1} with a shoulder at 1131 cm^{-1}. The peak at 1131 cm^{-1} became more intense than it was at RTP.

2.3.4.3 1,2-Propanediol on γ-Al_2O_3

Pure 1,2-PDO exhibited a $\nu_{asym}CH_3$ mode at 2973 cm^{-1}, as well as $\nu_{asym}CH_2$ and $\nu_{sym}CH_2$ modes at 2930 and 2876 cm^{-1}, respectively (Figure 2.5 a). Two νCO modes were evident at 1136 and 1038 cm^{-1} and a CH_3 rocking mode was observed at 1077 cm^{-1}.[78] The νCH region of 1.3 wt% 1,2-PDO on γ-Al_2O_3 witnessed a red shift in the $\nu_{asym}CH_3$ fundamental frequency, relative to pure 1,2-PDO, to 2970 cm^{-1}. The two νCH_2 modes did not shift, and two new, weak modes appeared at 2855 and 2815 cm^{-1} (Figure 2.5 b). The two νCO modes experienced blueshifts of 9 and 19 cm^{-1}, moving them to 1145 and 1057 cm^{-1}. The CH_3 rocking mode underwent a minor blueshift to 1084 cm^{-1} and a new peak appeared at 1107 cm^{-1}.

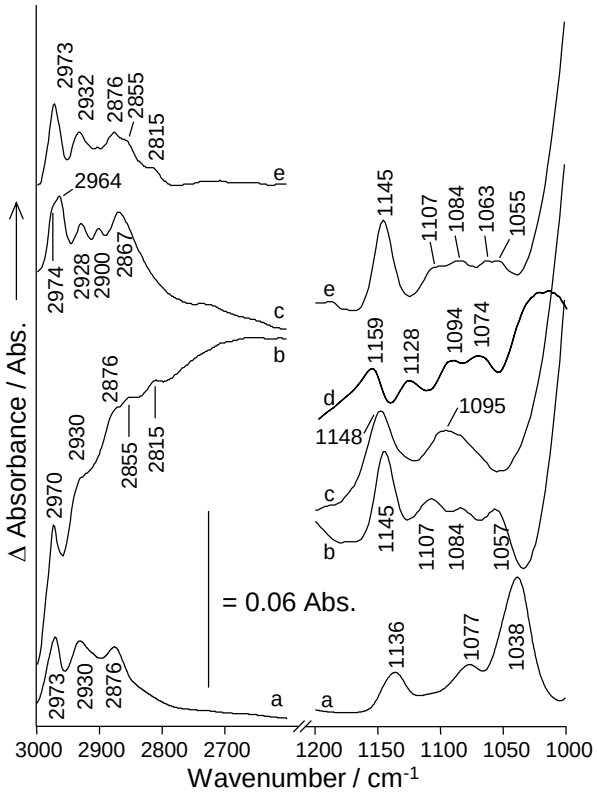

Figure 2.5 IR spectra of pure 1,2-PDO and 1,2-PDO on γ-Al_2O_3. Pure 1,2-PDO, a. 1,2-PDO on γ-Al_2O_3 at RTP, b. 1,2-PDO on γ-Al_2O_3 after 1 h spent at RTHV, c. Difference spectrum of c and b, d. 1,2-PDO on γ-Al_2O_3 after 1 h spent at 1.00 mbar of H_2O vapor, e. Spectra b, c, and e are difference spectra in which the spectrum of γ-Al_2O_3 was subtracted from the 1,2-PDO loaded sample.

After the 1.3 wt% 1,2-PDO on γ-Al_2O_3 sample had been under HV at RT for 1 h, the νCH_3 mode shifted to 2964 cm^{-1} and gained a shoulder at 2974 cm^{-1} (Figure 2.5 c). The $\nu_{asym}CH_2$ mode redshifted slightly to 2928 cm^{-1}, a new νCH mode appeared at 2900 cm^{-1}, and the $\nu_{sym}CH_2$ mode shifted to 2867 cm^{-1}. The νCO mode previously at 1145 cm^{-1} broadened significantly and underwent a slight blueshift to 1148 cm^{-1}. One broad and fairly poorly defined mode at 1095 cm^{-1} also developed. The changes induced by placing this sample under HV conditions for 1 h in the νCO region of the spectrum are largely hidden by the relatively strong and broad νCO modes in the spectrum. In order to make

the changes induced by the HV treatment in the νCO region of the spectrum more observable, the spectrum of the sample at RTP (Figure 2.5 b) was subtracted from the spectrum of the sample at RTHV (Figure 2.5 c) which resulted in a difference spectrum where positive peaks indicate growth in new wavenumbers induced by the HV treatment (Figure 2.5 d). This spectrum clearly illustrates growth of new peaks at 1159, 1128, 1094 and 1074 cm^{-1} induced by the HV treatment.

When the sample was exposed to 1.00 mbar of water vapor for 1 h, the $\nu_{asym}CH_3$ mode again exhibited a single peak at 2973 cm^{-1}. The $\nu_{asym}CH_2$ peak was evident at 2932 cm^{-1}, and the $\nu_{sym}CH_2$ mode was again evident at 2876 cm^{-1}, with two small shoulders at 2855 and 2815 cm^{-1} (Figure 2.5 e). In the νCO region, the large, broad peak at 1095 cm^{-1} that existed in the RTHV spectrum disappeared, and again two νCO modes were clearly resolved at 1145 and 1107 cm^{-1} as was the CH_3 rocking mode at 1084 cm^{-1}. The νCO mode that existed at 1057 cm^{-1} at RTP (Figure 2.5 b) has been replaced by two strongly overlapping peaks at 1063 and 1055 cm^{-1}.

2.3.4.4 1,3-Propanediol on γ-Al_2O_3

Pure 1,3-PDO exhibited $\nu_{asym}CH_2$ and $\nu_{sym}CH_2$ modes at 2941 and 2880 cm^{-1}, respectively, as well as two overlapping νCO modes at 1056 and 1034 cm^{-1} (Figure 2.6 a). In the νCH region of 1,3-PDO on γ-Al_2O_3 at RTP, the $\nu_{asym}CH_2$ split into two peaks at 2933 and 2914 cm^{-1}, and the $\nu_{sym}CH_2$ mode at 2880 cm^{-1} developed a very weak shoulder at 2835 cm^{-1} (Figure 2.6 b). A peak was resolved at 2728 cm^{-1}. The νCO region of the spectrum developed three clearly defined peaks at 1144, 1115, and 1074 cm^{-1}. There was no evidence of the νCO modes of bulk 1,3-PDO at 1056 and 1034 cm^{-1} in this spectrum.

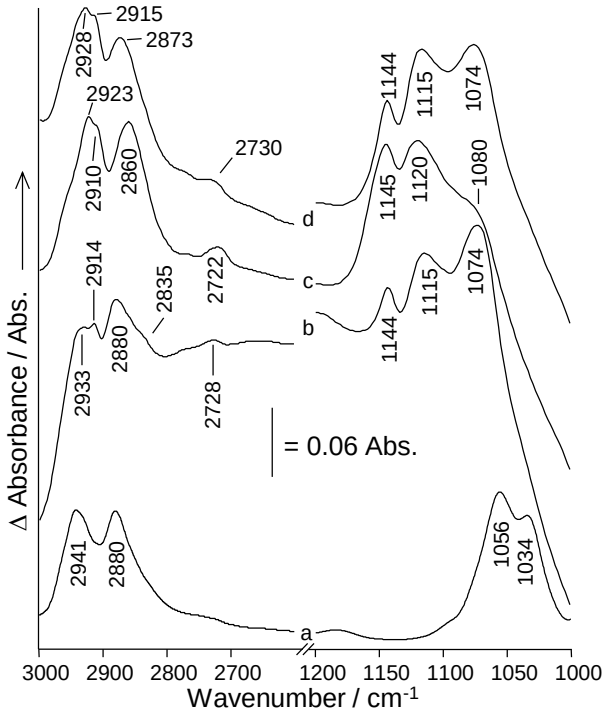

Figure 2.6 IR spectra of pure 1,3-PDO and 1,3-PDO on γ-Al_2O_3. Pure 1,3-PDO, a. 1,3-PDO on γ-Al_2O_3 at RTP, b. 1,3-PDO on γ-Al_2O_3 after 1 h spent at RTHV, c. 1,3-PDO on γ-Al_2O_3 after 1 h spent at 1.00 mbar of H_2O vapor, d. Spectra b-d are difference spectra, where the spectrum of γ-Al_2O_3 was subtracted from the 1,3-PDO loaded sample.

When 1,3-PDO on γ-Al_2O_3 had been under HV at RT for 1 h (Figure 2.6 c), the $\nu_{asym}CH_2$ modes shifted to 2923 and 2910 cm^{-1} and the $\nu_{sym}CH_2$ mode broadened and experienced a red shift to 2860 cm^{-1}. The νCH mode centered at 2728 cm^{-1} at RTP shifted to 2722 cm^{-1} in and increased in intensity as a result of HV exposure. The νCO modes that were at 1144 and 1115 cm^{-1} at RTP underwent minor blue shifts to 1145 and 1120 cm^{-1}, respectively. The peak at 1074 cm^{-1} also underwent a blue shift to 1180 cm^{-1} and exhibited a large decrease in intensity relative to the other νCO peaks.

The introduction of 1.00 mbar of water vapor to the sample after the HV period (Figure 2.6 d) induced blue shifts in the $\nu_{asym}CH_2$ peaks, to 2928 and 2915 cm^{-1}. The $\nu_{sym}CH_2$ peak also underwent a slight blue shift to 2873 cm^{-1}. The peak observed at 2722 cm^{-1} under HV is less resolved, and is shifted to 2730 cm^{-1} during the water exposure. The three νCO modes return to the same relative intensities and positions at 1144, 1115, and 1074 cm^{-1} as observed at RTP.

2.3.4.5 Glycerol on γ-Al_2O_3

Pure glycerol exhibited $\nu_{asym}CH_2$ and $\nu_{sym}CH_2$ modes at 2934 and 2878 cm^{-1}, respectively, as well as the νCO modes of the 1° carbon and the 2° carbon C-O bonds at 1030 and 1108 cm^{-1}, respectively (Figure 2.7 a).[79] In the νCH region of the spectrum of 1.3 wt% glycerol on γ-Al_2O_3 at RTP, the $\nu_{asym}CH_2$ at 2934 cm^{-1} broadened compared to pure glycerol, and the $\nu_{sym}CH_2$ mode at 2880 cm^{-1} developed two shoulders, one at 2900 cm^{-1} and the other at 2855 cm^{-1} (Figure 2.7 b). The νCO region of the spectrum showed three clearly defined modes at 1151, 1122, and 1075 cm^{-1} develop. There was no evidence of the νCO modes of bulk glycerol at 1108 and 1030 cm^{-1} in this spectrum.

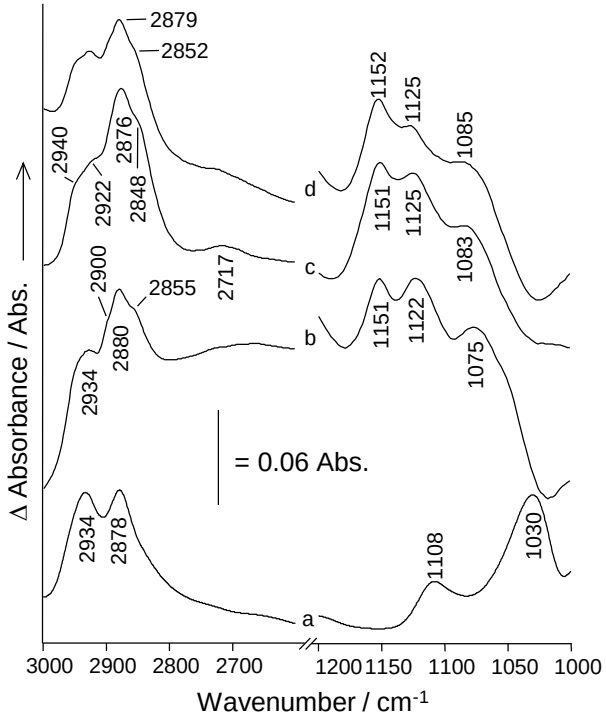

Figure 2.7 IR spectra of pure glycerol and glycerol on γ-Al_2O_3. Pure glycerol, a. glycerol on γ-Al_2O_3 at RTP, b. glycerol on γ-Al_2O_3 after 1 h spent at RTHV, c. glycerol on γ-Al_2O_3 after 1 h spent at 1.00 mbar of H_2O vapor, d. Spectra b-d are difference spectra, where the spectrum of γ-Al_2O_3 was subtracted from the glycerol loaded sample.

After 1 h spent under HV at RT, the $\nu_{asym}CH_2$ mode broadened further into at least two overlapping modes at 2940 and 2922 cm^{-1} (Figure 2.7 c). The largest $\nu_{sym}CH_2$ mode shifted to 2876 cm^{-1} with a single resolvable shoulder at 2848 cm^{-1}. A very weak and broad peak centered at 2717 cm^{-1} became evident. The νCO mode observed at 1151 cm^{-1} when at RTP did not change when under HV, the mode observed at 1122 cm^{-1} when at RTP underwent a marginal shift to 1125 cm^{-1} under HV. The mode observed at 1075 cm^{-1} in RTP decreased in intensity and blueshifted to 1083 cm^{-1} when under HV.

The introduction of 1.00 mbar of water to the sample after the HV treatment did not affect the $\nu_{asym}CH_2$ modes (Figure 2.7 d). The $\nu_{sym}CH_2$ peak underwent a slight blue shift to 2879 cm^{-1}, and the corresponding shoulder also underwent a blue shift to 2852 cm^{-1}. The peak observed at 2717 cm^{-1} under HV is less resolved, and is shifted to 2727 cm^{-1} during the water exposure. The three νCO modes were largely unaffected by the water treatment, and were observed at 1152, 1125, and 1085 cm^{-1}. These peaks did not change even after 48 h spent under 10.0 mbar of water vapor (not shown).

2.3.5 DFT Calculations of Glycerol/γ-Al_2O_3 interactions

Although many different interactions were considered for how glycerol could interact with the γ-Al_2O_3 surface, only those that were found to be the most energetically favorable in each scenario are discussed here. Figure 2.8 depicts the optimized structures in the cases of molecular adsorption (a), adsorption with a single H atom dissociated from a glycerol hydroxyl group (b), dissociation of multiple H atoms from the glycerol hydroxyls (c), and various ways that the H atom could then leave the γ-Al_2O_3 surface (d, e). In the case of molecular adsorption, the optimized structure exhibits a single alkoxy bond formed between a coordinatively unsaturated (CUS) Al atom and one of the 1° hydroxyl groups (Figure 2.8 a). Molecular adsorption resulted in an adsorption energy of -2.01 eV relative to gas phase glycerol.

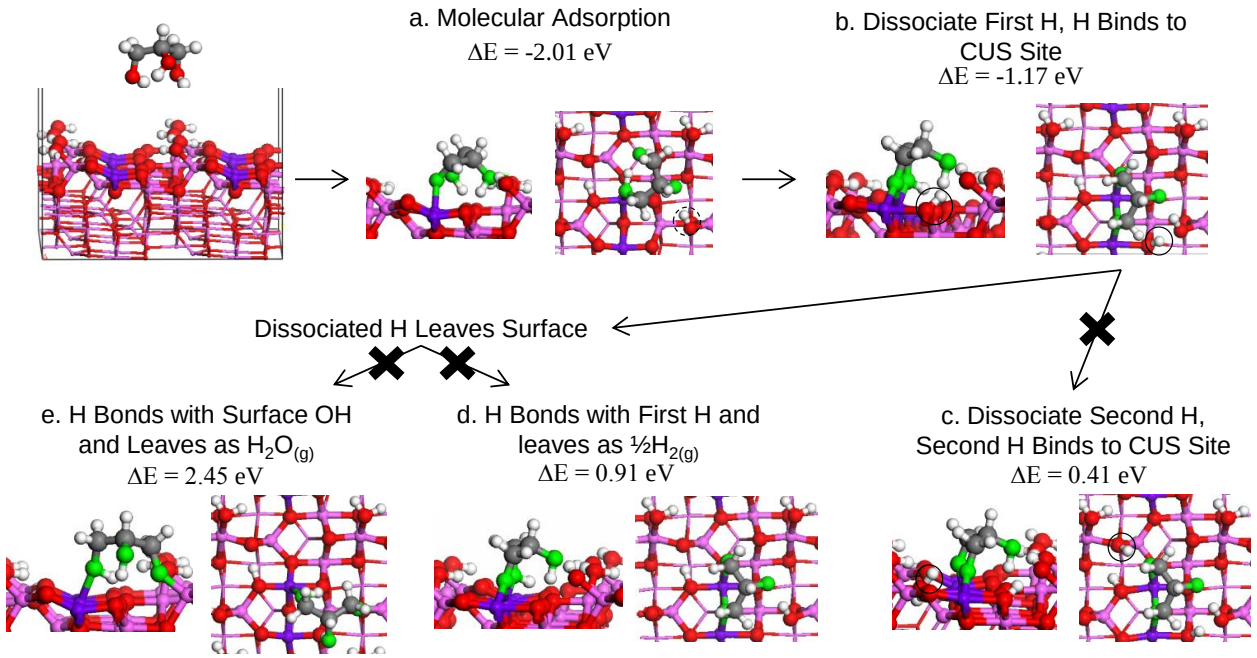

Figure 2.8 Side and top views of the most energetically favorable surface species of glycerol on γ-Al_2O_3 (110). Energies are relative to the previous step. Molecular adsorption, a. Adsorption with dissociation of one H atom, b. Adsorption with dissociation of a second H atom, c. Single dissociated H leaving as $½H_{2(g)}$, d. Single dissociated H forming H_2O with a surface OH of γ-Al_2O_3 and leaving as $H_2O_{(g)}$, e.

When dissociation of a single H atom from one of the glycerol hydroxyl groups was considered, the dissociation of the H atom from the 1° hydroxyl group involved in the alkoxy bond was found to be energetically favorable (Figure 2.8 b.). This dissociation resulted in a structure that is further stabilized by -1.17 eV. The dissociated H atom formed a bond to a nearby lattice O atom to form a surface hydroxyl group as indicated in Figure 2.8 b. The resulting adsorbed species exhibited two bonds to the γ-Al_2O_3 surface, one single and one bridging alkoxy bond to CUS Al atoms. This molecule also exhibited a hydrogen bonding interaction between the 2° OH group and the γ-Al_2O_3 surface. The bridging alkoxy bond formed from the O atom that dissociated the H atom to two CUS Al atoms. The hydroxyl group attached to the opposite 1° C atom strongly coordinated to one of the CUS atoms that was involved with the aforementioned dissociative bridging alkoxy group. Further dissociation of either of the H atoms from the remaining two hydroxyl groups of the surface bound glycerol species was found to be energetically unfavorable by at least 0.41 eV. The least unfavorable optimized surface species in this scenario is shown in Figure 2.8 c.

Alternative fates of the dissociated H atom were considered. Having the dissociated H atom leave the surface as $\frac{1}{2}H_{2(g)}$ was found to be energetically unfavorable by at least 0.91 eV (Figure 2.8 d). Having the dissociated H atom combine with a surface hydroxyl of γ-Al_2O_3, indicated by the dashed circle in Figure 2.8 b, and leave the surface as $H_2O_{(g)}$ was also found to be energetically unfavorable by at least 2.45 eV (Figure 2.8 e).

The vibrational modes observed experimentally and calculated in the νCO region of pure glycerol and of the lowest energy conformation of glycerol on the γ-Al_2O_3 surface

are shown in Table 2.1.The atoms involved in the calculated vibrational modes referred to in Table 2.1 are illustrated in Figure 2.9. The experimental peaks reported for the pure glycerol sample were collected from pure glycerol in the liquid phase, and the calculated frequencies were based on the αα conformation of a single glycerol molecule (Figure A.6). The calculated frequencies lie in excellent agreement with the experimental data for both pure glycerol, and glycerol adsorbed on γ-Al_2O_3.

Table 2.1 Comparison of experimentally observed and calculated vibrational modes of pure, liquid glycerol and glycerol on γ-Al_2O_3 in the 1200-1000 cm^{-1} region.

Pure Glycerol			Surface Species		
Experimental / cm^{-1}	Calculated ($\alpha\alpha$) / cm^{-1}	Mode	Experimental / cm^{-1}	Calculated / cm^{-1}	Atoms Involved
1108	1107	2° OH νCO	1151	1151	H3 H8 C2 O1
1030	1044	1° OH νCO	1125	1124	H1 H2 H4 H6 H7 H8 C1 C2 C3 O2 O3
	1043	1° OH νCO	1083	1090	H3 H4 H6 H7 H8 C2 C3 O4
				1070	H3 H8 O1

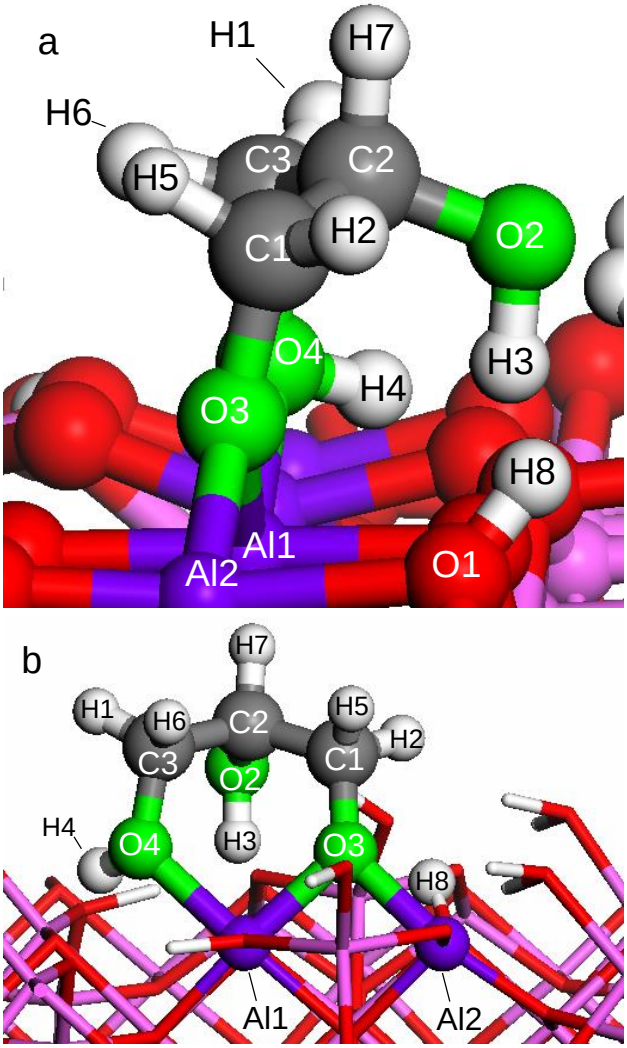

Figure 2.9 Most energetically favorable conformation of glycerol adsorbed on γ-Al_2O_3 in the case of single H dissociation, a. Molecule rotated 90° for clarity, b. Atoms are labeled for vibrational mode analysis in Table 2.1.

2.4 Discussion

2.4.1 Adsorption Behavior of Polyols on γ-Al_2O_3

Adsorption steps play a critical role in heterogeneous catalysis and separations. Adsorption studies of biomass derived oxygenates are typically performed with an aqueous solution of the oxygenate,[32-34,80] and in many cases water will compete with the oxygenate for adsorption sites on the surface.[81] A recent series of publications provided a notable insight into the adsorption of biomass derived oxygenates, including polyols on zeolites, which consist of a crystalline micropore network.[32,33] Dispersion forces between a polyol and the pore walls of the zeolite are the most influential factor on adsorption behavior of these systems.[32,33] The uptake of polyols decreases with an increasing number of OH groups in a sorbate molecule of constant carbon chain length suggesting that OH groups hinder the interactions of the sorbate with zeolite pore walls. The position of the OH groups on the carbon chain of the polyol, however, had little influence on the uptake. Additionally, water-sorbate interactions have a minor influence on the uptake behavior of such molecules on various zeolites.[33]

For comparison to γ-Al_2O_3, aqueous phase adsorption isotherms of polyols on ZSM-5 were included in the present study. The isotherms generally agreed with the previously mentioned trends (Figure 2.1).[32,33] 1,3-propanediol (1,3-PDO) experienced the highest uptake on ZSM-5, ethylene glycol (EG) and 1,2-propanediol (1,2-PDO) experienced very similar uptakes, that were greater than that of glycerol, which experienced the lowest uptake on ZSM-5. By contrast, the only molecule to exhibit a detectable uptake on γ-Al_2O_3 in an aqueous environment was glycerol. The lack of uptake of the polyols on γ-Al_2O_3 is not surprising, as the γ-Al_2O_3 used in the current study is an

amorphous, mesoporous material with an average pore diameter of ca. 12 nm compared to that of ZSM-5 which is ca. 0.55 nm.[82] Therefore, the γ-Al_2O_3 lacks the well-defined and confined micropore structure that would be needed for the sorbate molecule to experience significant dispersion forces.

The molecule with the most OH groups analyzed in the current study, glycerol, exhibited the strongest uptake on γ-Al_2O_3 out of all of the polyols, opposite the trend witnessed with ZSM-5. Therefore, it is clear that the adsorption of polyols on γ-Al_2O_3 is governed by different forces than the adsorption on zeolites. In addition to porosity, a major difference between zeolite and γ-Al_2O_3 is the different hydrophobicity/hydrophilicity of these materials. Zeolites become very hydrophobic as the Si/Al ratio increases.[75] Since the zeolites used by Mallon et al. had reasonably high Si/Al ratios (i.e. 11-140) they provided a hydrophobic environment, in which higher uptakes for polyols with fewer OH groups is expected.[32,33]

In contrast, the surface of γ-Al_2O_3 is much more polar than that of high silica zeolites because it contains various types of OH groups and coordinatively unsaturated Al sites.[72,73,83] As a result, γ-Al_2O_3 is significantly more hydrophilic than most zeolites and competitive adsorption between water and polyols limits the adsorption of polyols. The hydrophilic surface of γ-Al_2O_3 is also the reason that glycerol is absorbed to the largest extent. As glycerol has the most OH groups, one for every carbon in the molecule, it is best able to compete with water for adsorption sites on γ-Al_2O_3 and results in the greatest uptake observed of all the polyols in the current study. The fact that none of the other molecules were adsorbed to a measureable extent suggests that both total number of OH

groups, and the position of each OH group have an influence on surface interactions between polyols and γ-Al_2O_3.

The results of the ^2H solid echo pulse NMR analyses also suggest that polyol/γ-Al_2O_3 interactions occur at 25 °C, and are dependent on both polyol structure and amount of co-adsorbed water present. EG on γ-Al_2O_3 exhibited purely liquid like behavior (i.e. the molecule experienced no reduction of mobility relative to pure or aqueous EG) after the impregnation procedure (Figure 2.2 a). This indicates that while residual, physisorbed water from the impregnation procedure is present, the EG primarily interacts with the water and not the γ-Al_2O_3 surface. After 12 h in dry air flow, the sample exhibited a Pake signal, indicative of strong interactions between EG and the γ-Al_2O_3 induced by the removal of physisorbed water (Figure 2.2 b). After equilibration with ambient air, the Pake signal decreased, suggesting that some of the EG was replaced of the surface of γ-Al_2O_3 by water, but other EG molecules remained bound to the surface (Figure 2.2 c).

Glycerol interacted with the surface more strongly than EG even in the presence of physisorbed water, as evidenced by the presence of a Pake pattern after impregnation (Figure 2.2 d). Removing a portion of the physisorbed water with dry air flow resulted in stronger interactions with the surface, as evidenced by the increased Pake pattern (Figure 2.2 e). Exposure of the sample to ambient air resulted in a complete reversal to its initial state after the impregnation procedure (Figure 2.2 f). Glycerol with strongly hindered mobility was still present on the surface of γ-Al_2O_3.

Consequently, both the structure of the polyol and the presence of physisorbed water dictate the degree of interaction between the polyol and the γ-Al_2O_3 surface. The competitive adsorption of water and EG on γ-Al_2O_3 requires that the relative

concentration of water be reduced in order for strong interactions between EG and γ-Al_2O_3 to form at 25 °C. As a result, aqueous phase adsorption isotherms show little uptake of EG on γ-Al_2O_3. Glycerol, however, interacts to a significant extent with the γ-Al_2O_3 surface even in the presence of physisorbed water resulting in a measureable uptake in an aqueous phase adsorption isotherm. It is important to note that surface interaction may be different under reaction conditions (i.e. elevated temperature) because adsorption equilibria shift with changing temperature and it becomes easier to overcome the activation barrier for the formation of certain chemisorbed surface species.

2.4.2 Surface Species Formed by Polyols on γ-Al_2O_3

Surface species formed from mono-functional alcohols with up to three carbon atoms on γ-Al_2O_3 have been well documented in the absence of coadsorbed water.[52,54,56,84,85] At RT, methanol predominantly forms both linearly bound and bridging methoxy species on γ-Al_2O_3. The linearly bound methoxy species gives rise to peaks at 1190 and 1150 cm^{-1}, and the bridging species gives rise to a peak at 1090 cm^{-1} in the νCO region.[85] Similarly, at RT, ethanol will form linearly bound and bridging ethoxy species on γ-Al_2O_3.[52,54] The linearly bound ethoxy group gives rise to a νCO mode with a frequency of 1115 cm^{-1}, and the bridging ethoxy group gives rise to two νCO modes with frequencies of 1070 and 1052 cm^{-1}. 1-propanol will form linear and bridging 1-propoxy species on γ-Al_2O_3.[84] 2-propanol will also form both linearly bound and bridging propoxy species on γ-Al_2O_3 at RT.[56] The linearly bound 2-propoxy species is evidenced by a νCO mode with a frequency of 1170 cm^{-1}, and the bridging 2-propoxy species is evidenced by a νCO mode with a frequency of 1131 cm^{-1}.[56]

In the current study, multiple new νCO modes were observed in the 1200-1000 cm^{-1} range when γ-Al_2O_3 was impregnated with polyols and subjected to RTHV. The spectra at RTHV are most comparable to those of the previously mentioned studies of mono-functional alcohols as residual, physisorbed water was removed by the HV environment (Figure 2.4 through Figure 2.7). The minor changes witnessed in the νCH regions of the spectra of adsorbed polyols are attributed to redistribution of electron density within the sorbate upon interaction of the molecule with the surface of γ-Al_2O_3. The new peaks in the 1200-1000 cm^{-1} region of all of the different polyols on γ-Al_2O_3 are in general agreement with the formation of linearly bound and bridging alkoxy species of mono-functional alcohols. However, the fact that the polyols have multiple OH groups allows for the formation of many possible monodentate, bidentate, or tridentate surface alkoxy species. As a result, a more detailed assignment of these νCO peaks based on the IR spectroscopy alone is difficult.

The results of our DFT calculations of glycerol on γ-Al_2O_3 provide valuable insight into the assignments of the observed νCO modes. Using the present model of γ-Al_2O_3 (110), the most stable surface species was formed after dissociation of a single H atom from one of the 1° OH groups of glycerol, while the other two OH groups interact with the surface (Figure 2.8 b). Note that the surface interaction of 1° OH group is stronger than that of the 2° OH group. The calculated vibrational frequencies of this surface species gives rise to four fundamental vibrations in the 1200-1000 cm^{-1} region with frequencies that are in excellent agreement with the experimentally observed frequencies of this region (Table 2.1). The atoms that experienced the greatest displacements in a fundamental mode with a frequency of 1151 cm^{-1} were the C2, H3,

H8, and O1 atoms. This suggests that this is a mode that includes the νCO stretch of the 2° OH group of glycerol that is involved in a hydrogen bond to the γ-Al_2O_3 surface. These atoms were also involved in two calculated fundamental frequencies at 2830 and 2645 cm^{-1} which are attributed to the peak observed at 2717 cm^{-1} (Figure 2.7 c), supporting the assignment of this peak to hydrogen bonding between the polyol and the γ-Al_2O_3 surface. It should be noted that the discrepancies in these frequencies is likely due to the fact that this DFT model is prone to error in calculating frequencies molecules involved in hydrogen bonds.[86] The fundamental vibration with a calculated frequency of 1124 cm^{-1} included the C1, C2, C3, O2, and O3 atoms. This suggests that the experimentally observed peak at 1125 cm^{-1} is due to a coupled νCO/νCC mode that includes the νCO vibration of the bridging alkoxy bond involving O3. The fundamental vibration with a calculated frequency of 1090 cm^{-1} includes the C2, C3, and O4 atoms, which suggests that the experimentally observed peak at 1083 cm^{-1} is likely due to a coupled νCO/νCC mode that includes the displacement of O4, which strongly interacts with Al1. The aforementioned hydrogen bonding interaction between atoms O2, H3, H8, and O1 exhibits a calculated mode with a frequency of 1070 cm^{-1} that may contribute to the experimentally observed peak at 1083 cm^{-1}.

Since 1,3-PDO has 1° OH groups in the same positions as glycerol, and the strongest surface interactions occurred through the 1° OH groups, it is reasonable to expect the formation of a comparable surface species. This is the basis for the strong similarities between the two species' respective IR spectra. The fact that 1,3-PDO lacks the additional 2° OH group surface may be the basis for a weaker surface interaction and explain its weaker uptake than glycerol in the adsorption isotherms.

The IR spectra of adsorbed EG and 1,2-PDO strongly suggest the formation of surface alkoxy species with similar νCO modes to that of the surface species formed by 1,3-PDO and glycerol. However, they contained a significantly larger number of peaks in 1200-1000 cm^{-1} region. Specifically, they exhibit peaks at ca. 1160 and 1130 cm^{-1}. The surface alkoxy species formed by ethanol, 1-propanol, and 2-propanol all also exhibit alkoxy νCO modes with nearly identical frequencies.[52,54,56,84] As a result, IR spectroscopy alone cannot determine whether interactions through the 1° or 2° OH group of 1,2-PDO is the dominant interaction. A detailed assignment of the origins of these peaks would require additional DFT calculations that were beyond the scope of this work.

2.4.3 Influence of the Presence of Water on the Surface Species Formed by Polyols on γ-Al_2O_3

In contrast to the adsorption of polyols on zeolites,[32,33] the combination of large pore diameter, and a highly hydroxylated surface in the case of γ-Al_2O_3 provide an environment in which competitive adsorption between polyols and water has a large influence on polyol uptake by γ-Al_2O_3. In fact, a previous study of EG and water co-adsorbed from gas phase onto the γ-Al_2O_3 (0001) surface found that EG primarily interacted with water on the alumina surface, rather than with the alumina directly.[87]

Glycerol on γ-Al_2O_3 at RTP exhibited three peaks in the νCO region attributed to a multidentate alkoxy species (Figure 2.7 b). Since this sample contained residual water from the impregnation procedure, this implies that glycerol is capable of forming chemisorbed surface species when physisorbed water is present. Neither the removal of the physisorbed water by HV treatment (Figure 2.7 c), nor the reintroduction of water vapor resulted in significant changes to the νCO region of the spectrum, suggesting that

small amounts of water had little effect on the formation of the surface species in the case of glycerol (Figure 2.7 c). Similarly, 1,3-PDO exhibited a loss of its native νCO peaks and the appearance of three new peaks at RTP (Figure 2.6 b). The new peaks are also attributed to the formation of a multidentate alkoxy species, which occurred in the presence of physisorbed water. The intensity of the peak at 1074 cm^{-1} showed a dependence on co-adsorbed water (Figure 2.7 b, c, d), but the other alkoxy modes in the νCO region were unaffected, suggesting that the 1,3-PDO surface species and co-adsorbed water only interacted very weakly.

By contrast, the surface species formed from the polyols with OH groups only on the first and second carbons were strongly dependent on the presence of physisorbed water. EG experienced shifts in its νCO modes at RTP, attributed to weak interactions with the γ-Al_2O_3 surface (Figure 2.4 b). The formation of peaks that are consistent with the formation of a mulitdentate alkoxy species required the removal of physisorbed water by HV treatment (Figure 2.4 c). Upon the reintroduction of water to the sample (Figure 2.4 d), the high frequency νCO peaks attributed to an alkoxy species of EG are almost completely removed, and the spectrum largely resembles that of the sample prior to the HV treatment. This dynamic behavior in the νCO region indicates that alkoxy bond formation is inhibited by co-adsorbed water in the case of EG, and that the formation of alkoxy bonds by removing water is reversible upon reintroduction of water.

Similarly, 1,2-PDO exhibits minor changes in the νCO region after impregnation at RTP (Figure 2.5 b). The minor changes are again attributed to relatively weak interactions with the γ-Al_2O_3 surface in the presence of physisorbed water. Growth of peaks that lie in agreement with an alkoxy species similar to that formed by glycerol only

occur after water was removed by HV treatment (Figure 2.5 c, d), and are almost completely reversed by the reintroduction of water to the sample (Figure 2.5 e). Like with EG, 1,2-PDO only forms peaks indicative of a mulitdentate alkoxy surface species in the absence of physisorbed water, and the formation of the species is reversible in the presence of water.

The differences observed in the formation of surface alkoxy species observed in the current study are attributed to steric constraints in the sorbate molecules and their corresponding surface alkoxy species. As the most stable surface species of glycerol involved a bridging alkoxy bond formed by one 1° OH group and a strong interaction with the other 1° OH group, 1,3-PDO also formed a similar surface species. EG and 1,2-PDO, however, are not capable of forming such a surface species, but can only form a multidentate alkoxy structure with bonds from the vicinal OH groups. All attempts a forming a multidentate alkoxy structure from glycerol involving bonds formed from the OH groups of the first and second carbon in DFT calculations resulted in the desorption of the glycerol from the surface to a lower energy state. In this case, the formation of any surface species was very energetically unfavorable because the molecule had to be very strongly distorted in order to form such a surface species. As a result, EG and 1,2-PDO only weakly interacted with surface sites on alumina while competing with water. When the water was removed by HV, strained bidentate and/or monodentate surface species were formed. The formation of these species was readily reversed by reintroducing water to the sample.

2.4.4 Sites for Alkoxy Bond Formation on γ-Al_2O_3

Previous studies suggested that the formation of surface alkoxy groups from mono-functional alcohols on various metal oxides, including γ-Al_2O_3, can occur by either of two pathways:[88] dissociation of the H atom of the alcohol group and the formation of the alkoxy bond formation with a coordinatively unsaturated Al atom of γ-Al_2O_3, and also, a condensation reaction between an alcohol group and a surface hydroxyl of γ-Al_2O_3 forming water as by-product. Although water is expected to interact with the CUS sites of γ-Al_2O_3, a previous study found that at least some of these CUS sites remain very reactive even in the presence of adsorbed water.[89]

Interactions of the polyols with the surface OH groups of γ-Al_2O_3 are evidenced by changes in the νOH region of the difference spectra of the polyol loaded γ-Al_2O_3 samples (Figure 2.3). Unfortunately, precise assignment of these peaks to specific surface OH groups of γ-Al_2O_3 is not straightforward, as there is still an ongoing dispute in the literature. Moreover, the termination of alumina surfaces changes upon exposure to water.[89] The results in the current study will be discussed in the light of two of the more popular models for the surface OH groups of γ-Al_2O_3 (Table A.3).[72,90] Assignments from Knözinger et al. are in good agreement with the peaks seen in the OH region of the IR spectrum of γ-Al_2O_3 in the current study. However, the basis for these assignments, an empirical net electric charge calculation, has been called into question in recent publications.[72] The more recent study by Digne et al. provides a model that also explains the experimentally observed peaks from the current study with one exception: multiple peaks are assigned to OH groups bonded to Al atoms in pentahedral coordination.[72] As there is no evidence of such Al atoms in the ^{27}Al MAS-NMR spectrum of the γ-Al_2O_3

used in the current study, these assignments do not fully explain the OH modes of γ-Al_2O_3 observed in the current study.

Regardless of the exact assignments, the νOH region of all of the IR spectra of different polyols on γ-Al_2O_3 showed clearly defined interactions between the polyols and the OH groups of γ-Al_2O_3 (Figure 2.3). The spectra of all of the polyol-loaded samples collected at RTP exhibited negative peaks of comparable intensity at 3772 and 3700 cm^{-1} (Figure 2.3 c, e, g, i), which indicates interaction with these specific surface OH groups of γ-Al_2O_3. Interactions between the polyol molecules and physisorbed water were evidenced by the hydrogen bonding νOH mode with a frequency at ca. 3475 cm^{-1}. The assignment of these peaks to hydrogen bonding interactions between the polyols and water is supported by the fact that these peaks were completely removed by exposure to HV (Figure 2.3 b, d, f, h). HV treatment also induced interaction between the polyol molecules and the γ-Al_2O_3 OH group with a frequency at 3730 cm^{-1}. It is important to emphasize that the all polyols studied here interacted with surface OH groups of γ-Al_2O_3 in the same way and that changes in this region of the spectra only depended on the presence of physisorbed water.

In contrast, the formation of alkoxy species from polyols on γ-Al_2O_3 was affected by both the structure of the polyol, and the presence or absence of physisorbed water. This indicates that the interactions between the surface hydroxyls of γ-Al_2O_3 and a polyol are not coupled to the formation or presence of alkoxy species. Consequently, it is proposed that the formation of alkoxy species from polyols with two or three carbon atoms occurs through interactions with the CUS sites of γ-Al_2O_3, and not through condensation with surface OH groups.

2.4.5 Implications for the Stability of γ-Al_2O_3 in Hot Liquid Water

A series of previous studies showed that pure γ-Al_2O_3 and γ-Al_2O_3 supported metal catalysts are unstable in hot liquid water because γ-Al_2O_3 is eventually converted to boehmite.[30,31,74,91] As γ-Al_2O_3 deteriorates, supported metal particles agglomerate to some extent, and some are encapsulated by the boehmite phase, reducing the number of catalytic sites.[30] In the presence of model biomass compounds, specifically polyols, the stability of γ-Al_2O_3 against this transformation increased notably due to the formation of carbonaceous species, which protect the support against hydrolytic attack.[31,92] These carbonaceous species were proposed to have formed by a variety of reactions, including dehydration and condensation reactions. The stabilizing effect increased with increasing carbon chain length and number of OH groups of the polyol. It was speculated that this trend was due to the formation of multidentate surface species.

The results of the current study provide insight on the stabilizing effect of the polyols on the phase transformation of γ-Al_2O_3 in hot liquid water. The current study established that polyols with OH groups separated by at least three carbon atoms irreversibly formed multidentate alkoxy surface species bonded to the CUS Al sites of γ-Al_2O_3 in the presence of co-adsorbed water at RTP. As alcohols are known to undergo acid catalyzed dehydration reactions on the Lewis acidic CUS Al sites of γ-Al_2O_3, it seems very likely that these alkoxy species are either the carbonaceous deposits that protected γ-Al_2O_3 from hydrolytic attack, or the precurors to these species. The longer the carbon chain of the polyol, the more readily it forms a stronger, multidentate alkoxy species with more bonds to the γ-Al_2O_3 surface, and thus is more effective at blocking γ-Al_2O_3 from hydrolytic attack.

2.5 Conclusions

In the present study, I present a method for studying the role of coadsorbed water on the formation of surface species formed by water soluble model biomass compounds, with low vapor pressures, on γ-Al_2O_3. Competitive adsorption between coadsorbed water and the polyols (i.e. ethylene glycol, 1,2-propanediol, 1,3-propanediol, and glycerol) limits their uptake from aqueous solutions on the γ-Al_2O_3. Polyols with more hydroxyl groups experience stronger surface interactions and greater uptake than those with fewer hydroxyl groups, opposite the trend with ZSM-5 (Si/Al = 60). While adsorption of polyols on hydrophilic (high Si/Al ratio) ZSM-5 materials is governed largely by pore confinement effects, the large pore size and hydrophilic, hydroxyl containing surface of γ-Al_2O_3 requires interaction with multiple hydrophilic hydroxyl groups of biomass derived oxygenates in order to overcome competitive adsorption with water.

A combination of IR and DFT analysis indicates that glycerol is able to form a multidentate alkoxy species with two coordinatively unsaturated Al atoms on the surface of γ-Al_2O_3 in the presence of physisorbed water. One of the primary alcohol groups of glycerol dissociates a hydrogen atom and forms a bridging alkoxy bond to the surface, and the other primary alcohol group strongly coordinates to the same surface site. The secondary alcohol group is involved in a hydrogen bond to the surface. The IR spectrum of 1,3-propanediol on alumina contains nearly identical alkoxy modes compared to the spectrum of adsorbed glycerol, suggesting that it too forms a multidentate alkoxy species to coordinatively unsaturated Al surface atoms in the presence of physisorbed water. By contrast, both ethylene glycol and 1,2-propanediol require that the physisorbed water be removed before alkoxy species can form. Having hydroxyl groups on the one and three

carbon atoms of a polyol allows for the formation of a strongly bound multidentate alkoxy species in the presence of water. However, when hydroxyl groups are only present on the one and two carbon atoms of a polyol it does not allow for the formation of such strongly bound multidentate alkoxy species, likely due to steric constraints. By extrapolation, longer polyols with more hydroxyl groups are expected to exhibit even stronger interactions with γ-Al_2O_3 in the presence of water. This explains the stabilizing effect of polyols against the transformation of γ-Al_2O_3 to boehmite in hot liquid water observed in previous studies.

CHAPTER 3

SURFACE INTERACTIONS OF GLYCEROL WITH ACIDIC AND BASIC METAL OXIDES

3.1 Background

Aqueous phase catalytic processes for converting and upgrading biomass derived oxygenates into value added products such as fuels,[17] platform chemicals,[15] or specialty chemicals[22] have received a great deal of attention recently as a potentially green and carbon neutral means of supplementing or replacing many fossil fuel derived chemicals. Additionally, there are a number of recent studies that investigate the adsorption and reaction of dilute oxygenates in aqueous systems on metal oxides or zeolites as they pertain to advanced water purification methods.[93,94] Polyols have also recently been shown to be effective structure directing agents in the synthesis of zeolites.[95] Consequently, the surface chemistry of oxygenates on metal oxide and heterogeneous catalyst surfaces in aqueous systems is a topic of increasing importance to many fields.

Many multi-functional oxygenate molecules are soluble in water because their oxygen containing functional groups provide polarity to the molecules. This property, combined with the abundance and environmentally friendly nature of water, make water an ideal solvent for the conversion of oxygen containing compounds. Metal oxides are very commonly studied and industrially utilized as solid acids, solid bases, or as supports for metal catalysts used in the production of chemicals and in oil refining.[28] As a result, they are a natural choice as a starting point for designing catalysts for lesser understood reactions in aqueous phase. The presence of water can significantly alter how a molecule

interacts or adsorbs to a surface.[96-98] Specifically, in the case of γ-Al_2O_3,[89,99] water can create highly reactive sites not native to the dry metal oxide. The role of water on surface interactions of oxygenated molecules has not been thoroughly investigated and is of clear importance.

In order to efficiently and effectively design catalytic systems for the aqueous phase conversion of oxygen containing compounds, an in depth understanding of the relevant surface chemistry must be obtained. Note that an in-depth knowledge of the relevant surface chemistry was essential to the development of catalytic processes for oil refining.[28] However, analogous studies in literature regarding aqueous phase conversion of biomass are few in number.[32,33,36,37,49,100] Perhaps the largest and most nearly related body of knowledge regards the adsorption of mono-alcohols on metal oxides. Methanol, ethanol, 1-propanol, and 2-propanol are all known to form linear and bridging alkoxy species to metal oxide surfaces, including γ-Al_2O_3, TiO_2, ZrO_2, and CeO_2.[52-54,56,58,84,85,88,101] The alkoxy bonds have been proposed to form from the alcohol groups of the molecules to either a Lewis acid site on the metal oxide through deprotonation, or through a dehydration reaction with a surface hydroxyl group of the metal oxide.[88]

The lack of studies regarding the surface chemistries of multi-functional oxygenates is, in part, due to the experimental complications associated with studying such molecules in the presence of water using traditional surface science techniques. Many spectroscopic techniques used for studying surface chemistry require dosing the probe molecule in gas or vapor phase onto the surface being studied.[52-54,56,58,84,85,88,101] However, this method is extremely challenging with many oxygenates as they have little or no vapor pressure at room temperature, and often decompose before volatilizing when

heated.[20] Additional complications arise due to the presence of water. Water is a dense medium and makes many common spectroscopic techniques useful for studying surface chemistry either difficult or impossible.[102]

Despite the challenges associated with studying the surface chemistry of oxygenates and water on catalyst surfaces and supports, there are a few studies that have provided insight on the subject. One series of studies investigated the adsorption of oxygen containing compounds, including polyols, from aqueous solutions onto hydrophobic (relatively high Si/Al ratio) zeolites. These studies primarily relied on adsorption isotherms and concluded that dispersive forces formed when a polyol is confined in the pore of a zeolite are the primary means of interaction and dictate the degree of adsorption.[32,33] Consequently, polyols with increasing numbers of hydroxyl groups exhibited less uptake, and the position of the hydroxyl group had little effect on the degree of adsorption.

A different study which investigated the adsorption of polyols from aqueous solution by a hydrated Al_2O_3 found that uptake increased with increasing number of hydroxyl groups, and that the position of the hydroxyls on the polyol had a large effect on adsorption.[34] As a result, the adsorption phenomena of polyols on lower surface area, larger pore diameter, hydrophilic metal oxides are clearly different from those of polyols on larger surface area, smaller pore diameter, hydrophobic zeolites. Both reaction studies of selective dehydration of alkanediols over CeO_2 and adsorption studies of such molecules on CeO_2 by density functional theory (DFT) suggested that both oxygen atoms of the diol will interact with coordinatively unsaturated (CUS) cerium atoms.[35] Another DFT study of the adsorption of ethylene glycol on basic metal oxides found that ethylene

glycol would interact strongly with the CUS magnesium atoms of MgO through both of its alcohol groups, but the alcohol groups would not deprotonate and form alkoxy bonds to the surface.[36]

Studies that provide information regarding surface interactions of polyols with metal oxides through direct observation of surface species are exceedingly rare. One such study investigated the interactions of two and three carbon polyols with γ-Al_2O_3 primarily using Fourier transform infra-red (FT-IR) spectroscopy and DFT calculations.[100] Glycerol and 1,3-propanediol formed multidentate structures whose main interactions were a bridging alkoxy bond and an acid/base interaction formed by the primary alcohol groups to CUS aluminum surface atoms. Additionally, the secondary alcohol of glycerol was found to interact with the γ-Al_2O_3 surface through a hydrogen bond. These surface species were able to form in the presence of coadsorbed water. In contrast, ethylene glycol and 1,2-propanediol only formed surface species with alkoxy bonds to the Lewis acid sites of γ-Al_2O_3 after coadsorbed water was removed from the surface, and were removed by re-adsorbing water on the sample. Consequently, both the number and the location of hydroxyl groups had a large influence on the surface species formed by polyols on γ-Al_2O_3. Such interactions have been found to have profound effects on the material stability of γ-Al_2O_3 supported Pt and Ni catalysts in aqueous phase reforming conditions.[29-31,74]

The purpose of the present study is to understand how the properties of different metal oxides affect the surface species formed by glycerol. Specifically, γ-Al_2O_3, basic surface enhanced γ-Al_2O_3, TiO_2 anatase, a commercial and a synthesized ZrO_2, MgO, and CeO_2 are studied. These different metal oxides are all common catalysts and catalyst

supports, and provide a range of surface properties, such as acidity, basicity, and degree of surface hydroxylation. The range of surface properties provided by the materials allows for the investigation of how metal oxide characteristics influence the surface species formed by glycerol. There is a particular focus on how acidity and basicity affect the surface interactions of glycerol with the metal oxide, as interactions with Lewis acid sites were found to be essential for alkoxy bond formation in a previous study.[100] The effect of coadsorbed water on these surface interactions is also explained.

3.2 Materials and Methods

3.2.1 Materials

Glycerol (99%) was purchased from Sigma Aldrich and was used as received. HPLC grade pyridine (≥ 99.9%) was purchased from Sigma Aldrich and was further purified by three freeze-pump-thaw cycles before use. Water was procured from a Barnstead NANOpure ultrapure water system which purified house deionized water to 18.2 MΩ/cm. Ultra high purity grade CO_2 (UHP, Grade 5) was purchased from Airgas and was used as received.

γ-Al_2O_3 (99.5% metals basis) was purchased from Sigma Aldrich, calcined at 500 °C for 4 h with 5 °C/min ramp rates and stored in a desiccant jar before use. ZrO_2 "for catalyst support" (Alfa ZrO_2) and TiO_2 anatase were purchased from Alfa Aesar and were used as received.

MgO was synthesized by calcining a reagent grade $Mg(OH)_2$ purchased from Sigma Aldrich at 500 °C for 4 h with 5 °C/min ramp rates.[103] Both CeO_2 and ZrO_2 were prepared by precipitation from precursors with 99% trace metals purity purchased from

Sigma Aldrich. Either $Ce(NO_3)_3 \cdot 6H_2O$ or $ZrO(NO_3)_2 \cdot H_2O$ was dissolved in deionized water to form a 0.1 M solution. The solution was added drop-wise to A.C.S. reagent grade NH_4OH while continuously stirring. The precipitate was vacuum filtered, rinsed with deionized water, and dried in an oven overnight at 100 °C. The resulting dry powder was calcined in 200 mL/min zero grade air at 500 °C (5 K/min) for 4 h. A basic surface enhanced γ-Al_2O_3 was synthesized in accordance with previously reported procedures using surfactant P-123® mediated self-assembly of pseudoboehmite nano particles.[104,105] Typically, 13.75 g of pseudoboehmite from Sasol North America (Catapal B, 74.3% Al_2O_3) was peptized in a mixture of 0.9 mL nitric acid (Fischer Scientific, ~70%) and 200 mL deionized water. The resulting suspension was sonicated for 90 min at room temperature followed by stirring at 60 °C for 17 h. The suspension was subsequently cooled to room temperature. The peptized alumina obtained was added to a solution made by dissolving 15.30 g Pluronic P123® in 200 mL ethanol (200 proof). This solution was further stirred for 24 h at room temperature. After the stirring, the solvent was evaporated at 60 °C and the alumina composite was further dried at 75 °C for 24 h. The white sol-gel derived γ-Al_2O_3 was obtained by calcination of this composite at 700 °C for 4 h with a heating ramp of 1 °C/min and an intermediate step of 150 °C for 1 h for the removal of both water and ethanol.

3.2.2 Catalyst Characterization

N_2 physisorption measurements were carried out on a Micromeritics 2020 ASAP physisorption analyzer. Before analysis, samples were degassed under vacuum at 200 °C for 4 h. The Brunauer-Emmet-Teller (BET) surface area was calculated from five adsorption data points in the $0.05 \leq P/P_0 \leq 0.3$ region of the isotherm.[60] Pore volumes

were calculated using the desorption branch of the isotherm utilizing the Barrett-Joyner-Halenda (BJH) method.[61] X-ray diffractograms were collected using a Phillips X'pert diffractometer which utilized a X'celerator module and Cu Kα radiation. Diffractograms were collected between incident angles of 2θ = 5° and 70° with a step size of 0.0167°.

In situ CO_2, and pyridine adsorption followed by temperature programmed desorption (TPD) FT-IR spectroscopy were all carried out using a self-built ultra-high vacuum (UHV) setup connected to a self-built temperature controlled transmission infra-red (IR) cell, which are described in detail elsewhere.[100] The FT-IR spectrometer used was a Thermo Nicolet 8700 FT-IR spectrometer which utilized a MCT/A detector. For each spectrum, 64 scans were collected at a resolution of 4 cm^{-1}. Activation of samples for these techniques consisted of activating at 500 °C while under vacuum, pressure ≤ 1 x 10^{-6} mbar. Sample wafers were produced by pressing the sample in an in-house built stainless steel die set with a 0.5 in diameter at 4 kN for 30 s resulting in wafers with a density of ca. 25 mg/cm^2 (Table B.1). In situ heating of the samples carried out at 10 °C /min using a coiled resistive heating wire in which the sample wafer sat and was controlled by a K type thermocouple in contact with the heating wire inside the cell. Samples were cooled at the natural rate at which the cell cooled. When pyridine was adsorbed, the temperature was reduced to 100 °C after activation, and an "activated" sample spectrum was collected. Pyridine was then introduced into the chamber, and the pressure maintained at 0.1 mbar for 20 min. After the dosing period, the sample was subjected to vacuum for 30 min and the "100 °C" spectrum was collected. The sample was then heated to 200 °C, held for 1 h, and the temperature was reduced to 100 °C before collecting the "200 °C spectrum". This temperature program and spectrum

collection was repeated for 300, 400, and 500 °C. The averaged extinction coefficient for pyridine adsorption on Lewis acid sites from Tamura et al. were used to quantify the Lewis acid site concentrations of the materials.[106]

In the case of CO_2 adsorption, after the activation period, the temperature was reduced to 30 °C and the "activated spectrum" was collected. Subsequently, CO_2 was dosed at incrementally increasing pressures. The pressure was maintained for 5 min before collecting the spectrum at a given pressure, and subsequently increasing the CO_2 pressure. After the highest pressure was achieved, ca. 10 mbar, and the corresponding spectrum collected, the CO_2 was removed by pulling vacuum on the sample for 30 min, and the "30 °C" spectrum was subsequently collected. A similar temperature profile and spectrum collection procedure was used with CO_2 adsorption as was used with pyridine, except that the lowest temperature spectra were collected at 30 °C. The temperature steps and spectra collection were carried out in 100 °C increments to a maximum temperature of 500 °C. Proton induced x-ray emission (PIXE) measurements were carried out by Elemental Analysis Inc.

3.2.3 IR Spectroscopy of Adsorbed Glycerol

The metal oxides were impregnated with glycerol via an ex-situ wet impregnation method. An amount of a metal oxide, typically 250 mg, was added to a glycerol solution of a known volume, typically 2 mL, and known concentration in order to deposit the desired amount of glycerol (typically 1.3 wt/wt% glycerol to dry γ-Al_2O_3). The resulting slurry was mixed with a vortexer for 30 s, and was then mixed on a shaker table for 4 h. The slurry was then poured onto a watch glass and placed in a desiccant jar for 48 h. The

impregnated sample was then scraped from the watch glass and stored in a 20 mL scintillation vial.

A detailed description of how the difference spectra were obtained can be found elsewhere,[100] but the method is briefly described here. Spectra were collected of a water loaded and a glycerol loaded metal oxide (1.3 wt/wt% glycerol) using the previously mentioned UHV transmission cell and FT-IR spectrometer either at room temperature and pressure (RTP), after 1 h spent under UHV, or 1 h of 0.1 mbar water vapor. The backgrounds were collected with the transmission IR cell in the beam path with no sample wafer either at RTP or under UHV. After IR analysis, the sample wafer was removed from the chamber and a circle of 6.35 mm in diameter was massed in order to find the area density of the sample wafer. The spectrum of the water loaded sample under a given environment was subtracted from the spectrum of the glycerol loaded sample under the same environment, after it was normalized for any differences in optical thickness (wafer area density). The resulting difference spectrum primarily exhibits the glycerol surface species formed on the metal oxide, and any difference induced in the spectrum of the metal oxide by the presence of the glycerol surface species.

3.3 Results

3.3.1 Catalyst Characterization

The results of N_2 physisorption analysis indicated that all of the materials used in the present study were of moderate surface area, 54.1 to 224.6 m^2/g (Table B.2). The x-ray diffractograms of the metal oxides indicate that all of the materials have some degree of crystallinity (Figure B.1). The broad peaks of low intensity observed in γ-Al_2O_3, basic γ-Al_2O_3, ZrO_2, and CeO_2 suggest that the crystallites are relatively small, and that the

majority of the bulk materials are amorphous. By contrast, the TiO_2, Alfa ZrO_2, and the MgO samples have at least one peak of significant intensity and relatively narrow width, suggesting these materials have a higher proportion of crystalline domains relative to amorphous domains.

PIXE measurements of the two ZrO_2 materials revealed small, but significant differences in the trace components of the two metal oxides. The in-house prepared ZrO_2 had a Hafnium impurity of 1.95% ± 0.02% compared to that of the Alfa ZrO_2 which was 1.79% ± 0.02%. ZrO_2 typically does have a hafnium impurity as zirconium and hafnium are commonly found together in nature and are very difficult to separate.[107] The difference between the hafnium content of the two samples is relatively small, and is not likely the basis of any differences in properties of the two materials. The most significant difference in composition of the two samples was in titanium content. The in house prepared ZrO_2 had a titanium content of 260 ppm ± 100 ppm while the Alfa ZrO_2 had a titanium content of 615 ± 120 ppm.

Every metal oxide analyzed in the current study exhibited a measurable concentration of Lewis acid sites (LAS), as determined by pyridine adsorption followed by FT-IR spectroscopy (Figure 1.1 and Table B.3). No Brønsted acid sites (BAS) were observed in any of the metal oxides (Figure B.2). The acid site concentration at a desorption temperature of 100 °C is defined as the total site concentration, and the acid site concentration after desorption at 500 °C is defined as the strong acid site concentration. The strong acid site concentration of the materials increases as follows: MgO < basic γ-Al_2O_3 < ZrO_2 < TiO_2 < γ-Al_2O_3 < CeO_2. The acid site concentrations of Alfa ZrO_2 at the various desorption temperatures were ca. 18 times that of the

synthesized ZrO_2, and were many times higher than that of the other metal oxides. This abnormally high apparent acid site concentration of Alfa ZrO_2 , relative to the other metal oxides,[106] is attributed to an increase of the extinction coefficient for a ZrO_2 due to a significant titanium impurity. As a result, the acid site concentration of this material was not quantified. The wafer mass normalized integrated peak areas of the peak indicative of pyridine coordinated to a Lewis acid site at ca. 1445 cm^{-1} for the two ZrO_2 samples are shown in Figure B.3, for comparison.

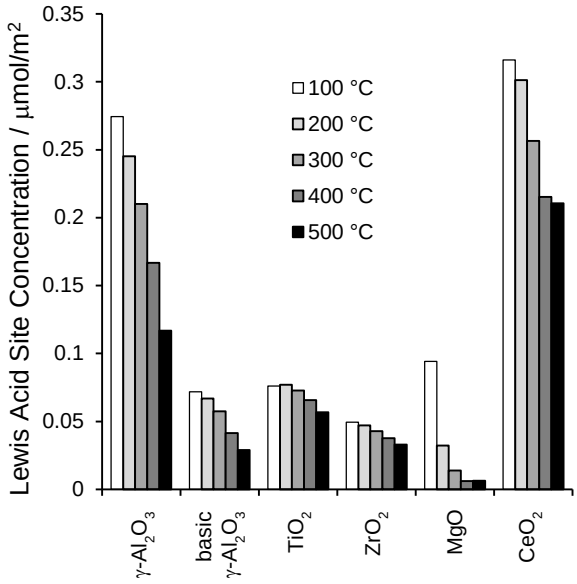

Figure 3.1 Lewis acid site concentrations of the metal oxides according to pydridine adsorption/TPD followed by IR spectroscopy.

The relative strength of the Lewis acid sites of the metal oxides was determined by temperature programmed desorption of pyridine followed by FT-IR spectroscopy (Figure B.4). TiO_2, CeO_2, and ZrO_2, have the highest fractions of strong acid sites with 74.5%, 66.6%, and 66.5%, respectively. γ-Al_2O_3, basic γ-Al_2O_3, and Alfa ZrO_2 had a

smaller fraction of strong acid sites than the aforementioned materials with 42.6%, 40.5%, and 32.3%, respectively. MgO had the smallest fraction of strong sites, 6.7%.

In situ CO_2 adsorption and temperature programmed desorption followed by FT-IR spectroscopy were used to investigate the basic character of the metal oxides. According to literature, interaction of CO_2 with relatively weakly basic hydroxyl groups of a metal oxide results in a bicarbonate surface species with a $\nu_{asym}OCO$, $\nu_{sym}OCO$, and δCOH modes at ca. 1650, 1480, and 1220 cm^{-1}, respectively.[108-110] Interaction of CO_2 with an intermediate strength basic site, comprised of a basic surface oxygen atom, results in a bidentate carbonate surface species with a $\nu_{asym}OCO$ mode and a $\nu_{sym}OCO$ mode with frequencies separated by ca. 300 cm^{-1}.[109] Interaction of CO_2 with the strongest type of basic surface oxygen atoms produces a unidentate carbonate surface species with a $\nu_{asym}OCO$ mode and a $\nu_{sym}OCO$ mode with frequencies separated by ca. 150 cm^{-1}.[109]

Only bicarbonate surface species formed on γ-Al_2O_3 and basic γ-Al_2O_3 when they were exposed to CO_2 (Figure B.5 a, b and Table 3.1). This indicates that both of these metal oxides have only weakly basic surface hydroxyls and have no other types of basic sites. Both ZrO_2 and Alfa ZrO_2 formed bicarbonate, bidentate carbonate, and unidentate carbonate surface species when exposed to CO_2 (Figure B.5 c, d and Table 3.1). These adsorbed CO_2 surface species indicate that both the ZrO_2 and the Alfa ZrO_2 have basic hydroxyls and basic surface oxygen atoms. The carbonate band structure of Alfa ZrO_2 is visibly more complicated than that of ZrO_2, particularly between 1625 and 1547 cm^{-1}, suggesting that it may have a more complex variety of basic surface oxygen atoms than ZrO_2.

Table 3.1 Carbonate mode assignment from CO_2 adsorption and desorption. All frequencies are in cm^{-1}.

	Bicarbonate			Bidentate Carbonate		Unidentate Carbonate	
	$\nu_{asym}OCO$	$\nu_{sym}OCO$	δCOH	$\nu_{asym}OCO$	$\nu_{sym}OCO$	$\nu_{asym}OCO$	$\nu_{sym}OCO$
γ-Al_2O_3	1647	1435	1229				
Basic γ-Al_2O_3	1647	1434	1228				
TiO_2	1603	1437	1237			1547	1376
	1584	1423	1225				
ZrO_2	1624	1431	1218	1600	~1325	1568	~1325
Alfa ZrO_2	1625	1416	1218	1563	1330	1547	1385
MgO	1629	1403	1218	1682	1330		
				1663	1300		
CeO_2	1610	1395	1216	1579	1287		

A bicarbonate species and two distinct bidentate carbonate species formed on MgO when exposed to CO_2 (Figure B.5 e and Table 3.1). Consequently, the MgO used in the present study had basic surface hydroxyls and two distinct moderately basic surface oxygen atom sites. There was no evidence of a unidentate carbonate species however, indicating that the MgO lacked strongly basic surface oxygen atoms. One bicarbonate species and one bidentate carbonate species formed on CeO_2 when introduced to CO_2 (Figure B.5 f and Table 3.1). There was no evidence of a unidentate carbonate species. As a result, the CeO_2 used in the present study had weakly basic surface hydroxyls, and moderately basic surface oxygen atoms, but no strongly basic surface oxygen atoms according to the in situ CO_2 TPD IR spectroscopy technique.

In the case of TiO_2, two resolvable bicarbonate species and a unidentate carbonate species formed with increasing partial pressure of CO_2 during CO_2 adsorption (Table 3.1 and Figure B.6). After desorption at 30 °C (Figure B.6 g), only very weak bands corresponding to a bicarbonate species and a unidentate carbonate species remained, unlike any of the other metal oxides analyzed. At desorption temperatures greater than 30 °C, bands corresponding to adsorbed CO_2 species are completely removed.

Consequently, TiO_2 has weakly basic surface hydroxyls and basic surface oxygen atoms, but these species can only very weakly adsorb CO_2, implying that they are very weak base sites.

The IR spectra of the metal oxides after impregnation with water exhibit the νOH and HOH scissor modes through the strong, broad peak ca. 3400 cm^{-1} and the peak at 1638 cm^{-1}, respectively (Figure B.7). These modes indicate that the wetted metal oxides have water on their surfaces and in their pores, despite the fact that they appear to be dry powders. Additionally, the spectra exhibit various broad peaks in the carbonyl region attributed to carbonates both on the surfaces of the materials, and likely also dissolved in the physisorbed water.

The IR spectra of the wetted metal oxides after one hour spent under UHV lack the broad and strong νOH mode and the HOH scissor mode of water, at ca. 3400 and 1638 cm^{-1}, respectively (Figure 3.2 and Figure B.7). Consequently, the vacuum treatment successfully removed the bulk H_2O from the metal oxides. The lack of multilayer, bulk water on the metal oxides makes observing the IR modes of bulk and surface functional groups possible even though monolayer or sub-monolayer water is likely still present.[111-115] It should be noted that the UHV treatment was not sufficient to remove all of the carbonates from surface basic sites on the materials, as evidenced by the various carbonate vibrational frequencies between 1700 and 1200 cm^{-1}, except in the case of γ-Al_2O_3 and the basic γ-Al_2O_3 (Figure B.8). These carbonates were formed during exposure to atmospheric CO_2 while handling the materials. The bulk phonon modes of all of the metal oxides used in the present study these materials all appeared below ca. 1100 cm^{-1} and absorb all of the IR beam, and as a result are not shown. A strong and very broad

peak at ca. 3400 cm^{-1} due to hydrogen bonding surface hydroxyl groups of the metal oxides and residual surface bound water can be seen in all of the metal oxides when under UHV (Figure 3.2) except in the case of MgO (Figure 3.2 f). MgO exhibits a weak and very broad peak centered near 3300 cm^{-1} with a more distinct peak at 3269 cm^{-1} overlaid. Both of these peaks are assigned to various surface hydroxyls of MgO involved in hydrogen bonds.

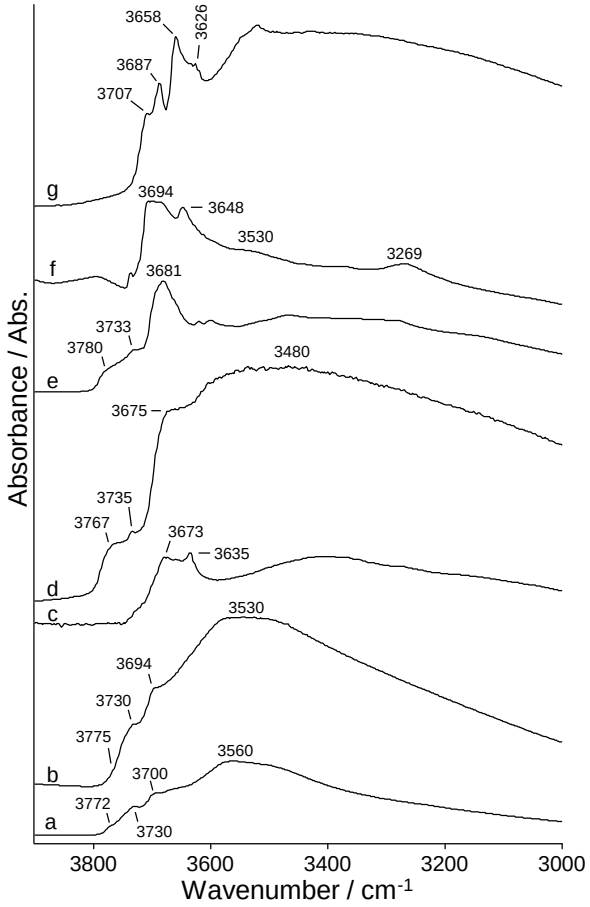

Figure 3.2 IR spectra showing the νOH region of the metal oxides used in the present study after one hour spent under UHV conditions: γ-Al_2O_3 (a), basic γ-Al_2O_3 (b), TiO_2 (c), ZrO_2 (d), Alfa ZrO_2 (e), MgO (f), CeO_2 (g).

Peaks attributed to vibrational modes of surface species that can be seen in the IR spectra of the metal oxides in Figure 3.2 are νOH modes of specific surface hydroxyls not involved in hydrogen bonding interactions, ca. 3800 to 3500 cm^{-1}. These peaks are assigned in Table 3.2. The peaks observed in the present study agree with previous studies with two notable exceptions. Firstly, the peaks positions of the νOH modes of surface hydroxyls of γ-Al_2O_3 are in near perfect agreement with literature.[72,90] However, there is uncertainty in the literature as to which surface hydroxyl the observed peaks belong. Two of the more common assignments for these modes are shown in Table 3.2. Secondly, in the case of the ZrO_2 samples, the νOH mode with a frequency at 3735 and 3733 cm^{-1}, for ZrO_2 and Alfa ZrO_2, respectively, has not been fully assigned. These peaks have been assigned to a νOH mode of a Si-OH group from a silicon impurity in the sample in a previous study.[63] However, this assignment is highly improbable in the present study as the PIXE analysis showed no detectable silicon impurity down to a detection limit of 438.7 ppm. As a result, these peaks are assigned to the νOH mode of a surface hydroxyl doubly coordinated to zirconium atoms in fourfold coordination (OH-μ_2-Zr_{IV}), as surface hydroxyls with such coordination in other metal oxides also give rise the to a νOH mode with a frequency between that of the singly and the triply coordinated surface hydroxyl groups (Table 3.2).

Table 3.2 Assignments of the νOH vibrations observed in the IR spectra of the metal oxides.

	νOH / cm^{-1}	**Ref. [90]**	**Ref. [72]**	
γ-Al_2O_3	3772	OH-μ_1-Al_{IV}	OH-μ_1-Al_{VI} (100)	
	3730	OH-μ_2-Al_{VI},Al_{IV}	OH-μ_1-Al_{IV} (110)	
	3700	OH-μ_3	OH-μ_2-Al_{VI} (110)	
	3560	H bonded	OH-μ_3-Al_{VI} (100)	
		Ref. [90]	**Ref. [72]**	
Basic γ-Al_2O_3	3775	OH-μ_1-Al_{IV}	OH-μ_1-Al_{VI} (100)	
	3730	OH-μ_2-Al_{VI},Al_{IV}	OH-μ_1-Al_{IV} (110)	
	3694	OH-μ_3	OH-μ_2-Al_{VI} (110)	
	3530	H bonded	OH-μ_3-Al_{VI} (100)	
		Ref. [63]		
TiO_2	3673	OH-μ_1-Ti_{IV}		
	3635	OH-μ_2-Ti_{IV}		
		Ref. [63]		**Present Work**
ZrO_2	3767	OH-μ_1-Zr_{IV}		
	3735	Si-OH impurity		OH-μ_2-Zr_{IV}
	3675	OH-μ_3-Zr_{IV}		
	3480			H bonded
		Ref. [63]		**Present Work**
Alfa ZrO_2	3780	OH-μ_1-Zr_{IV}		
	3733	Si-OH impurity		OH-μ_2-Zr_{IV}
	3681	OH-μ_3-Zr_{IV}		
		Ref. [116]	**Ref. [117]**	**Present Work**
MgO	3694	OH-μ_1-Mg_{VI}	OH-μ_1-Mg_{VI}	
	3648		OH-μ_1-Mg_{VI}	
	3530	OH-$\mu_{>1}$-Mg_{VI}	H bonded	
	3269			H bonded
		Ref. [63]		**Present Work**
CeO_2	3707			OH-μ_1-Ce_{IV}
	3687	OH-μ_1-Ce_{IV}		
	3658	OH-μ_2-Ce_{IV}		
	3626	OH-μ_3-Ce_{IV}		

3.3.2 Surface Hydroxyl Interactions Evidenced by IR Spectroscopy

The νOH region of the difference spectra of the glycerol solution loaded metal oxides with the water only loaded metal oxides spectra subtracted exhibit features indicative of interactions between glycerol and the surface hydroxyls of the metal oxides (Figure 3.3). In the cases of γ-Al_2O_3, basic γ-Al_2O_3, TiO_2, ZrO_2, and CeO_2 at RTP, glycerol interacted with a single surface hydroxyl group of no consistent coordination or relative frequency. UHV treatment induced interactions with additional surface hydroxyls as evidence by the additional negative peaks (Figure 3.3). These additional interactions were irreversible when water vapor was reintroduced. Impregnating Alfa ZrO_2 with glycerol also resulted in interactions with a single surface hydroxyl at RTP (Figure 3.3 e_1), and additional surface hydroxyls at UHV (Figure 3.3 e_2). Unique to this sample, the interactions with the additional surface hydroxyls were reversed by reintroducing water vapor to the sample. The impregnation of glycerol on MgO resulted in strong hydrogen bonding interactions experienced by the surface hydroxyls of MgO as evidenced by the broad, positive peak across the νOH region (Figure 3.3 f). This broad feature exhibited only minor changes in intensity with respect to the presence of coadsorbed water.

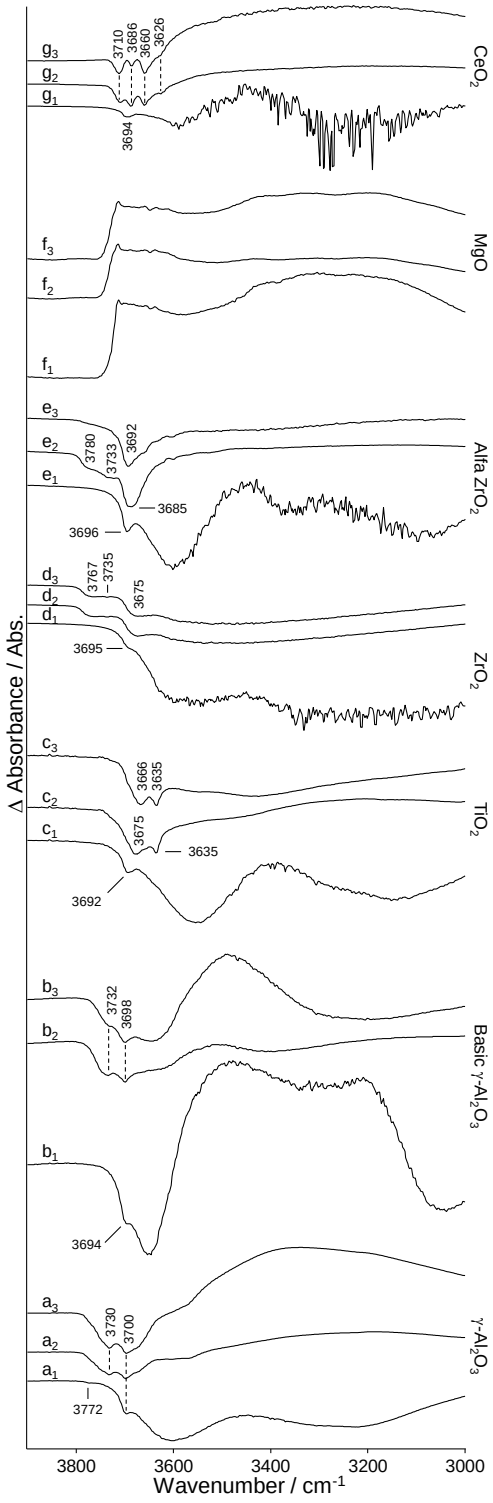

Figure 3.3 νOH Difference IR spectra of glycerol loaded metal oxide minus wetted metal oxide. Metal oxides include: γ-Al_2O_3 (a), basic γ-Al_2O_3 (b), TiO_2 (c), ZrO_2 (d), Alfa ZrO_2 (e), MgO (f), CeO_2 (g). The subscripts indicate the environment that the sample was exposed to at the time the spectrum was collected: RTP (1), UHV (2), and 0.1 mbar water vapor (3).

3.3.3 Glycerol Surface Species by IR Spectroscopy

When glycerol solution was loaded on all of the metal oxides, both its νCH and νCO modes changed significantly (Figure 3.4) relative to bulk glycerol (Figure 3.4 a), indicating significant interaction with the surface. These shifts are attributed to surface interactions as they are much greater and different in nature than shifts induced by glycerol-water interactions.[48,118] For all of the metal oxides, except MgO, loading glycerol solution on the metal oxide resulted in the disappearance of bulk glycerol 2° and 1° alcohol νCO peaks, at 1108 and 1030 cm^{-1}, respectively. Instead, two or three new peaks indicative of strong surface interactions through these alcohol groups were observed depending on the metal oxide, and the presence of bulk water. Three new peaks in the νCO region of the spectra (1200-1000 cm^{-1}) were observed at RTP in the case of glycerol adsorbed on γ-Al_2O_3, basic γ-Al_2O_3, and CeO_2 (Figure 3.4 b_1, c_1, h_1). For these materials, the highest frequency peak is attributed to a hydrogen bonding interaction that occurs between the 2° alcohol group of glycerol and the metal oxide surface (β interaction, Figure 3.5). The peak of intermediate frequency is attributed to a bridging alkoxy bond formed from a 1° alcohol group of glycerol and two Lewis acidic CUS metal surface atoms (α interaction, Figure 3.5). The peak of the lowest frequency in the νCO region of the spectra is attributed to a Lewis acid/base interaction through the other 1° alcohol group of glycerol to one of the CUS metal surface atoms involved in the bridging alkoxy interaction (γ interaction, Figure 3.5).[100] At RTP, all of the samples exhibited a negative peak at ca. 1640 cm^{-1} (not shown) due to the displacement of water from the pores and/or surface of the metal oxides by glycerol relative to the samples used for spectral subtraction, the metal oxides impregnated with only water.

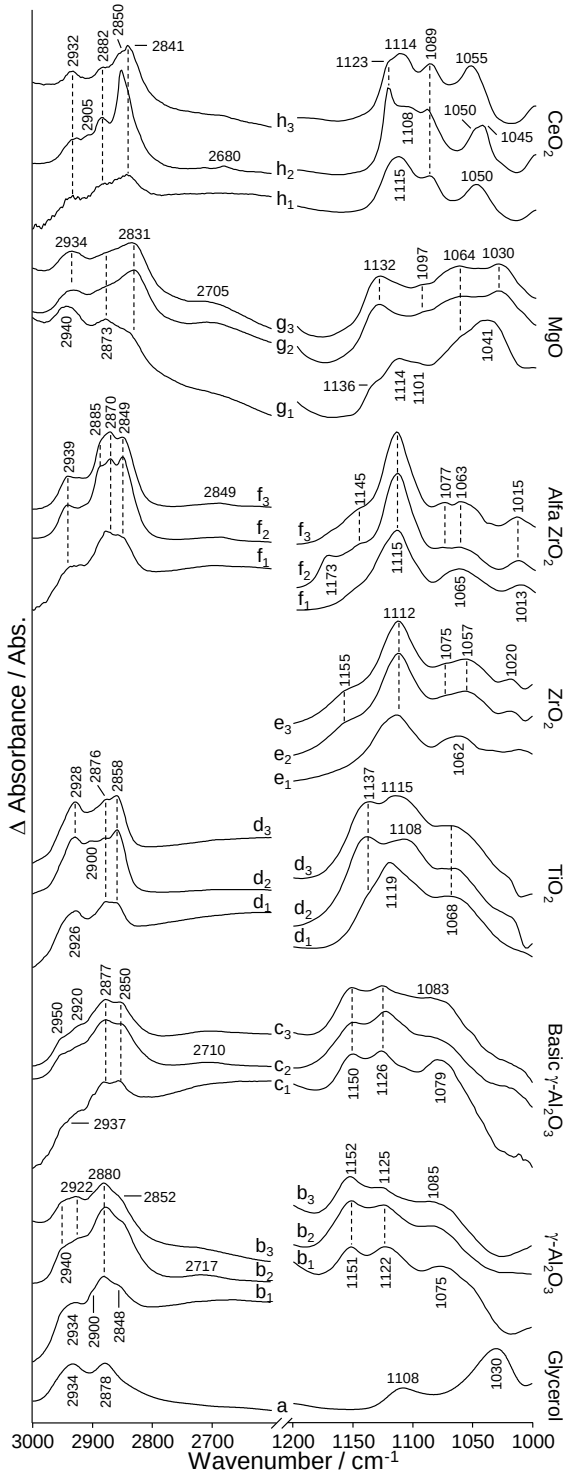

Figure 3.4 νCH and νCO regions of the difference IR spectra of glycerol loaded metal oxide minus wetted metal oxide. Metal oxides include: γ-Al_2O_3 (a), basic γ-Al_2O_3 (b), TiO_2 (c), ZrO_2 (d), Alfa ZrO_2 (e), MgO (f), CeO_2 (g). The subscripts indicate the environment that the sample was exposed to at the time the spectrum was collected: RTP (1), UHV (2), and 0.1 mbar water vapor (3).

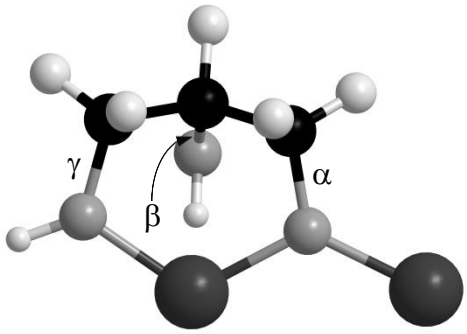

Figure 3.5 Depiction of glycerol adsorbed to CUS sites of a metal oxide. The white spheres indicate hydrogen atoms, the light grey spheres indicate oxygen atoms, the dark grey spheres indicate CUS surface metal atoms of a metal oxide, and the black spheres indicate carbon atoms.

Neither the removal of bulk water by UHV treatment nor the subsequent reintroduction of water vapor had a significant effect on these surface interactions in the cases of γ-Al_2O_3 and basic γ-Al_2O_3, as the peaks were largely unchanged by these environments (Figure 3.4 b_2, b_3, c_2, c_3). In the case of CeO_2 however, UHV treatment induced a splitting of the peak at 1115 cm^{-1} attributed to the β hydroxyl group. This split was reversed when water was re-adsorbed (Figure 3.4 h_3). The β interaction's dependence on the presence of coadsorbed water was unique to CeO_2.

Glycerol solution loaded on TiO_2, ZrO_2, and Alfa ZrO_2 at RTP resulted in a surface species that only exhibited the intermediate and low frequency peaks in the νCO region, indicating that only the α and γ interactions occurred between glycerol and these metal oxides (Figure 3.4 d_1, e_1, f_1). No hydrogen bonding between the 2° alcohol group of glycerol and the metal oxide surfaces occurred, and as a result the relatively weak peak of the 2° alcohol group of glycerol is largely masked by the peak attributed to the α alkoxy νCO mode. This β interaction was clearly induced by UHV treatment in the case of TiO_2,

but to a much lesser extent in the cases of ZrO_2 and Alfa ZrO_2. These interactions were not reversed by re-adsorbing water on the samples (Figure 3.4 d_3, e_3, f_3). Specific to Alfa ZrO_2, UHV exposure also induced the formation of a high wavenumber feature in the νCO region at 1173 cm^{-1} which was reversed by exposure to water vapor (Figure 3.4 f_2, f_3).

The νCO peaks of the α and γ interactions of each material resided at slightly different frequencies (Figure 3.4). As these surface interactions occurred between the 1° alcohol groups of glycerol and the CUS metal surface atoms of the metal oxides, the electronegativity of the metal atom is expected to have an influence on the νCO frequencies of these alcohol groups. In fact, there is a linear correlation between the νCO frequencies of the 1° νCO modes involved in alkoxy groups or Lewis acid/base interaction and the electronegativity of the surface metal atom involved in these interactions (Figure 3.6).

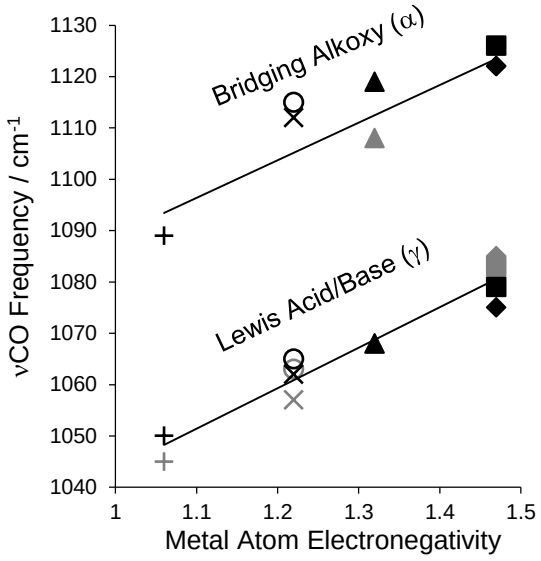

Figure 3.6 νCO frequency of alkoxy interaction vs. metal oxide metal atom electronegativity. γ-Al_2O_3 (♦), basic γ-Al_2O_3 (■), TiO_2 (▲), ZrO_2 (X), Alfa ZrO_2 (○),CeO_2 (+). RTP values shown in black, if UHV treatment induced a shift in νCO frequency, then the frequency when under UHV is shown in grey.

The νCO region of the spectrum of glycerol solution loaded on MgO largely resembles that of bulk glycerol, with weak high frequency shoulders on the 2° and 1° alcohol νCO peaks (Figure 3.4 g_1). The minor blue-shifts observed in these glycerol νCO modes indicates that the majority of the glycerol adsorbed on the MgO was primarily interacting with other glycerol molecules and/or physisorbed water on the MgO through hydrogen bonding interactions.[48] The shoulders at 1136 and 1064 cm^{-1} are assigned to the νCO modes of the 2° and 1° hydroxyl groups of glycerol, respectively, hydrogen bonding with the MgO surface. Removing the physisorbed water by UHV treatment resulted in only minor changes to the spectrum (Figure 3.4 g_2). In the νCO region, the shoulder previously at 1136 cm^{-1} shifted to 1132 cm^{-1} and significantly grew in intensity. The 2° hydroxyl νCO mode was not uniquely resolved, however a small feature at 1097 cm^{-1}

appeared. The 1° hydroxyl νCO vibration previously at 1041 shifted to 1030 cm^{-1}, and the shoulder at 1064 cm^{-1} grew in intensity. These changes suggest more hydrogen bonding occurred between the alcohol groups of glycerol and the MgO surface when bulk water was removed, but again there was no evidence of strong surface interactions like those observed with the other metal oxides. When water was reintroduced to the sample (Figure 3.4 g_3), there were no significant changes in the spectrum.

For the νCH region of the spectra, loading glycerol solution on all of the metal oxides, except MgO, resulted in splitting of the $\nu_{sym}CH_2$ and the $\nu_{asym}CH_2$ modes into two sets of $\nu_{sym}CH_2$ and the $\nu_{asym}CH_2$ modes (Figure 3.4). This is mainly attributed to inductive effects[119-121] from the strong α and γ surface interactions polarizing the CH_2 groups of glycerol to different extents, making them uniquely resolvable. Removing bulk water with UHV treatment from these metal oxides resulted in additional, minor splits and in some cases shifts of the νCH_2 modes of the surface bound glycerol. These changes are caused by additional interactions of the CH_2 groups with basic surface sites of the metal oxides made possible after bulk water was removed from these surface species. A similar behavior has been observed when methanol was adsorbed on certain zeolites.[122] The reintroduction of water to these materials only resulted in very minor changes to the νCH_2 modes of the metal oxide bound glycerol.

In the case of glycerol loaded on MgO, splitting of the νCH_2 modes occurred to a much lesser extent than the other materials (Figure 3.4 g_1). As glycerol did not form strong interactions with the surface of MgO, there were no inductive electronic effects to cause significant changes to the νCH_2 modes observed with the other metal oxides. Only weak hydrogen bonding interactions with the surface resulted in the small changes

observed in the νCH_2 vibrations of glycerol on MgO. UHV treatment again only induced minor changes to this region of the spectrum (Figure 3.4 g_2), and the reintroduction of water to the sample resulted in virtually no changes to the spectrum (Figure 3.4 g_3).

3.4 Discussion

3.4.1 Surface Properties of Metal Oxides

For the most part, the metal oxides utilized in the present study exhibited physical and chemical characteristics that were typical for the given material. All of the materials exhibited Lewis acid sites (LAS) due to coordinatively unsaturated (CUS) metal atoms and a variety of basic surface sites. None of the materials exhibited Brønsted acid sites (BAS).

The Alfa ZrO_2 was the only material that exhibited an uncharacteristically high apparent concentration of LAS according to pyridine adsorption followed by infra-red (IR) spectroscopy. The significant Ti impurity as determined by PIXE analysis suggests that the material can be thought of as a mixed oxide, rather than a pure zirconia. Even very small amounts of other metals added to the bulk structure of a metal oxide have been shown to very significantly alter the acid/base properties of the native material.[123,124] Titanium is known to aggregate on the surface of mixed titanium and zirconium oxides.[125] It is reasonable to suggest that such effects have altered the extinction coefficient for adsorbed pyridine for this sample to an unknown value that is significantly different than that for pure metal oxides. It should be noted, this impurity likely also resulted in a different distribution of surface hydroxyls relative to the self-prepared ZrO_2, as seen in their respective νOH modes by IR spectroscopy (Figure 3.2 d,e).

The combination of CUS surface metal and surface oxygen atoms, as well as the surface hydroxyls observed in all of the metal oxides used in the present study (in varying amounts), make for relatively polar, and thus hydrophilic surfaces. As a result, water is a nearly omnipresent surface species when dealing with these materials.[112,114,115] The removal of bulk water, or multilayer water, was achieved in the present study by exposure to ultra-high vacuum (UHV) at room temperature (RT) for 1 h. However, the removal of monolayer water from such materials typically requires the use of UHV and elevated temperatures for several hours.[112,114,115] Consequently, changes induced on the glycerol surface species by UHV exposure in the present study occur in the presence of monolayer, or sub-monolayer water coadsorbed with the glycerol. Additionally, exposure of the metal oxides to UHV at RT for 1 h did not remove surface carbonates formed during exposure to atmosphere from the surfaces of all metal oxides that contained basic oxygen surface sites (Figure B.8). This indicates that the basic surface oxygen atoms of moderate or strong basic strength are readily blocked by atmospheric CO_2, and are only completely liberated if activated using more severe thermal and/or chemical methods.[106]

It is noted that some of the metal oxides used in the present study are known to form hydrated phases when in contact with water. However, this typically requires elevated temperature and pressure,[29-31,74] or the presence of salts such as $NaNO_3$ and exposure times of several days to several months[126] in order for a measurable degree of hydration to occur. However, the conditions used in the current study are much less severe and no inorganic salts were present. Furthermore, biomass derived oxygenates are known to prevent such transformations,[29,31,34] and no such transformations were

witnessed in the IR spectra of the metal oxides. In conclusion, surface or bulk phase transformation of the metal oxides did not have a role in the present study.

3.4.2 Role of Lewis Acid Sites in the Formation of Surface Species from Glycerol on the Metal Oxides

In a previous study, glycerol was found to form a multidentate, chemisorbed surface species on γ-Al_2O_3 in the presence of coadsorbed, multilayer water.[100] This glycerol surface species engaged in a non-dissociative Lewis acid/base interaction from one of its 1° alcohol oxygen atoms to a Lewis acidic CUS aluminum surface atom (γ interaction, Figure 3.5), a dissociative, bridging alkoxy bond to two Lewis acidic CUS aluminum surface atoms from its other 1° alcohol group (α interaction, Figure 3.5), and a hydrogen bonding interaction between its 2° alcohol group and the γ-Al_2O_3 surface (β interaction, Figure 3.5). The formation of the two strongest surface interactions between glycerol and a metal oxide, the α and γ LAS interactions, was observed when glycerol was adsorbed on all of the metal oxides used in the present study, which exhibited strong LAS.

Only MgO was unable to form such a surface species. MgO did have a measurable concentration of weak LAS, but had virtually no strong LAS (Figure 3.1, Figure B.3). Both theoretical and experimental studies found that only defect sites on MgO dissociatively chemisorb methanol as a methoxide surface species.[127,128] Otherwise, the majority of the surface area of MgO has CUS metal sites that only physisorb methanol, as any CUS magnesium surface atoms lacked strongly acidic character. The lack of alkoxy bond formation by glycerol on MgO confirms that Lewis acid sites are required for the formation of alkoxy bonds between glycerol and a metal oxide surface. It

also supports the notion that the LAS must be of sufficient strength in order to form alkoxy bonds with a polyol, as was the case with methanol.

Surface alkoxide species formed by alcohols on metal oxides have been proposed to form by either directly interacting with a surface LAS, or through a dehydration reaction with a surface hydroxyl of the metal oxide.[88] However, a previous study found in the case of adsorbing two and three carbon polyols on γ-Al_2O_3, Lewis acidic CUS aluminum surface atoms were the predominant, if not exclusive, site for alkoxy bond formation.[100] In the present study, all of the metal oxides which exhibited a significant concentration of strong LAS formed a multidentate glycerol surface species through alkoxy bonds to the metal oxide surface in the presence of bulk water. Although water is expected to dissociatively adsorb on surface acid/base pairs on the metal oxide surfaces,[89,99] this process is a reversible one, and as such the LAS of the metal oxide are not completely blocked by adsorbed water. Evidently, glycerol is then able to access the LAS at least a small fraction of the time and is able to form relatively strong α and γ surface interactions that are stable in the presence of coadsorbed water. In fact, the displacement of relatively weakly bound hydroxyl groups from LAS which likely originate from dissociatively adsorbed water is evidenced by the negative νOH peaks observed when glycerol and water were coadsorbed on all of the metal oxides except MgO (Figure 3.3 a_1, b_1, c_1, d_1, e_1, g_1).

An additional unique peak appeared in the alkoxy bond region of the IR spectrum of Alfa ZrO_2 (Figure 3.4 f_2). This peak is tentatively attributed to additional interaction of the glycerol surface species with the LAS that give rise to the abnormally high apparent acid site concentration according to pyridine adsorption. Note that these interactions are

reversible as they no longer occurred when water vapor was re-introduced to the sample, after the evacuation step (Figure 3.4 f_3).

The electronegativity of the metal atom of the Lewis acid site to which glycerol binds has a large influence on the frequency of the observed alkoxy (α) and Lewis acid/base (γ) νCO modes of the surface species (Figure 3.6). This effect is not unexpected, as these metal atoms are directly involved in the alkoxy bonds and even a slight change in the electronegativity would be expected to change the electron density surrounding the oxygen and carbon atoms involved in the surface interactions. As the electronegativity of the metal atom with which an alcohol group oxygen atom interacts increases, it draws electron density from the oxygen atom. This in turn draws electron density from the corresponding carbon atom to a weaker extent (Figure B.9). The result is an increase in the dipole that exists between the alkoxy carbon and oxygen atoms, and thus a higher νCO frequency is observed. This polarizing effect likely has implications for Lewis acid site catalyzed dehydration reactions of polyols over metal oxides.

3.4.3 Role of Basic Oxygen Sites in the Formation of Surface Species from Polyols on the Metal Oxides

A previous study that first elucidated the surface structure of glycerol adsorbed on γ-Al_2O_3 indicated that the 2° alcohol group hydrogen bonded to the surface of γ-Al_2O_3. [100] Upon close inspection of the optimized structure, the 2° alcohol group is nearest to, and appears to interact with a basic surface oxygen group. This interaction (β hydroxyl, Figure 3.5) gave rise to the highest wavenumber feature in the νCO region of the IR spectrum of glycerol adsorbed on γ-Al_2O_3.

The materials, which formed a strongly bound glycerol surface species and lacked strongly basic surface oxygen atoms (Table 3.1), γ-Al_2O_3, basic γ-Al_2O_3, and CeO_2, were able to form this 2° hydroxyl surface interaction in the presence of bulk water. Conversely, the materials which had strongly basic surface oxygen atoms, ZrO_2 and Alfa ZrO_2, only exhibited very weak evidence of 2° hydroxyl surface interaction in any environment. TiO_2 had basic oxygen atoms of intermediate strength, and was only able to form a 2° hydroxyl hydrogen bonding interaction with glycerol after bulk water was removed by UHV treatment.

Evidently, the stronger basic oxygen sites are being poisoned and cannot form this interaction, whereas the weaker basic oxygen atoms remain available to interact with adsorbed glycerol. Due to the impregnation procedure used in the present study, the two species that are likely occupying the strong basic oxygen atoms are water and CO_2. As mentioned previously, water is known to dissociatively adsorb on metal oxides and convert a basic surface oxygen site to a surface hydroxyl, as well as associatively coordinate via Lewis acid-base interactions.[111-115] As the impregnation procedure in the present study utilized aqueous solutions of glycerol, many of the basic surface oxygen sites may have been converted to surface hydroxyls during the glycerol impregnation step.

Additionally, any basic surface oxygen atoms that might have survived exposure to water were also exposed to atmospheric CO_2 during handling of the samples. It is well known that exposure to CO_2 will result in the formation of carbonates on the basic sites of a metal oxide, effectively poisoning them. The IR spectra of all of the metal oxides after impregnation with water while at RTP and after 1 h spent under UHV exhibit

evidence of carbonates (Figure B.7 and Figure B.8, respectively) indicating that at least some fraction of the basic surface oxygen sites are actively poisoned by such carbonates. These results are also of practical consequence as any industrially utilized catalyst will undoubtedly be exposed to either atmospheric CO_2, or CO_2 dissolved in water if being used in aqueous systems.

Unique to CeO_2 in the present study, the removal of bulk water induced new surface interactions which gave rise to the IR modes nearest in frequency to the 2° hydrogen bond β νCO frequency (Figure 3.4 h_2). This suggests that, in the absence of bulk water, the glycerol surface species interacts through its 2° alcohol group with the CeO_2 surface in a manner unique to this metal oxide. CeO_2 is the most reducible metal oxide used in present study, and its oxygen defect sites are known to promote various oxidation reactions.[129] CeO_2 is also known to form multidentate alkoxide species with polyols via its Lewis acidic CUS cerium surface atoms.[35,130] Specifically, polyols with alcohol groups on the 1,3 carbons, like 1,3-butanediol, have been predicted to form a strongly bound surface species with linear alkoxy interactions through both of their alcohol groups. It was speculated that this surface conformation promotes interactions between the hydrogen atoms of the intermediate CH_2 group with the CeO_2 surface.[35] By analogy, it is reasonable that the surface conformation of glycerol, strongly bound to the surface through its two 1° alcohols, promotes interaction with the 2° alcohol group and the reducible surface oxygen atom, or oxygen defect site should it exist. It is proposed that this hydrogen bonding interaction with the uniquely reactive oxygen atoms of CeO_2 is what gives rise to the unique hydrogen bonding 2° alcohol modes seen when bulk water is not present (Figure 3.4 h_2). The reintroduction of water reversed the formation of

this interaction suggesting that it is likely very weak, and is prevented by the presence of water at room temperature.

3.4.4 Role of Basic Surface Hydroxyls in the Surface Interactions of Glycerol with Metal Oxides

In the case of the metal oxides which formed the alkoxy bonds with glycerol, all except MgO, interaction with a single, specific type of surface hydroxyl was observed while bulk water was present (Table 3.2 and Figure 3.3). As discussed in section 4.2, this could be due to displacement of hydroxyls from LAS which originated from dissociatively adsorbed water. However, a previous study showed that this interaction, in case of aqueous two and three carbon polyol solutions adsorbed on γ-Al_2O_3, did not necessarily correlate with the formation of alkoxy bonds to the surface.[100] The frequency of the surface hydroxyl involved in this interaction was not consistently the hydroxyl which is generally regarded as the most basic (highest νOH frequency)[90] or most acidic hydroxyl (lowest νOH frequency). Consequently, the reason the particular surface hydroxyl interacted with glycerol at RTP was likely due to proximity to the LAS with which glycerol most strongly interacts, not necessarily the basic strength of the surface hydroxyl.

Any additional interactions with surface hydroxyl groups for these metal oxides were only induced when bulk water was removed from the samples, and were coupled with minor changes in the νCH_2 vibrations of the adsorbed glycerol. This suggests that these ancillary surface hydroxyl interactions occur primarily through the CH and CH_2 groups of the surface glycerol species, and were prevented by the presence of bulk water. However, surface interactions of the CH group cannot be witnessed in the IR spectra as

the νCH peak of glycerol is shrouded by the much more intense νCH_2 peaks.[79] The fact that these interactions were not reversed by reintroducing water vapor to the sample suggests that once formed, the glycerol is able to effectively block not only the Lewis acid sites to which it is bound, but also the nearby surface hydroxyls of the metal oxide, hindering the adsorption of, or interaction with, water. Such interactions may be, at least in part, the source of the enhanced stability of γ-Al_2O_3 based catalysts in aqueous biomass solutions relative to pure water.[29-31]

Glycerol adsorbed with bulk water on MgO experienced the weakest interactions in the present study. Glycerol experienced hydrogen bonding interactions between the alcohol groups of glycerol and the surface hydroxyls of MgO, as well as with the bulk water. Removing the bulk water from the sample did not induce the formation of alkoxy bonds, but did marginally increase the degree of hydrogen bonding that occurred between the physisorbed glycerol and the surface hydroxyls of MgO. This behavior lies in agreement with a previous study that predicted non-dissociative surface interactions between ethylene glycol and the MgO (001) surface.[36] This indicates that interactions with surface hydroxyls alone are not enough to bind glycerol to the surface in the presence of bulk water.

3.4.5 Role of Water in the Surface Interactions of Glycerol with Metal Oxides

It is well known that water readily adsorbs to the surfaces of metal oxides, and typically requires the use of UHV and elevated temperatures to be completely removed.[111-115] More specifically, water is known to dissociatively chemisorb to a metal oxide surface, where the OH^- group from water bonds to a CUS surface metal atom, and the H^+ bonds to a basic oxygen surface atom.[111-115] Water will also physisorb on a metal

oxide surface through a Lewis acid-base interaction between the water oxygen atom and a CUS surface metal atom and also through hydrogen bonding interactions with metal oxide surface hydroxyl groups.

The fact that glycerol formed alkoxy bonds to the Lewis acidic CUS metal surface atoms in the presence of bulk water indicates that neither dissociatively adsorbed OH^- nor associatively adsorbed water molecules are adsorbed on CUS metal surface atoms in a manner that would poison these sites. This result supports recent studies which indicated that water can dissociatively adsorb on γ-Al_2O_3 while preserving highly reactive Lewis acid sites.[89,99] The fact that removing water induces hydrogen bonding interactions between the surface hydroxyls of the metal oxide and the multi-dentate glycerol surface species suggests that physisorbed water is present at RT and UHV and was hydrogen bonded to the surface hydroxyls of the metal oxide. When the bulk water is removed by vacuum, the physisorbed water is largely removed and thus the surface hydroxyls were free to interact with the already surface bound glycerol molecule. Consequently, water does not effectively block the sites for adsorption for polyols on Lewis acidic metal oxides, and plays a relatively minor role in how these polyols bond to the metal oxide surfaces as long as the polyol has a sufficient number and placement of hydroxyls with which it can bond to the metal oxide surface.

It should be noted that altering the pH of the impregnation solution might affect how glycerol interacts with metal oxide surfaces. Glycerol is a weak acid with a pKa of 14.15.[131] Consequently, lowering the pH of the impregnation solution would increase the amount of molecular glycerol and increasing the pH would increase the amount of glycerolate ion. Since the primary alcohol is the first to deprotonate, altering the

acid/base strength of this group could have a large influence on how the molecule interacts with Lewis acid sites on metal oxides. In the present case, it has to be considered that absorbed atmospheric CO_2 can slightly acidify the aqueous solution. Such effects were minimized in the present study by using ultra-purified water in the impregnation procedure. All of the samples experienced the same degree of atmospheric exposure, making any effects consistent across samples. Additionally, dissolved carbonates were removed along with the bulk water by HV exposure, eliminating any possible effects entirely from the corresponding spectra.

3.4.6 Importance of Findings for Heterogeneous Catalysis and Other Fields

While understanding the surface species/intermediates of multi-functional biomass molecules on both wet and dry metal oxide surfaces is of clear importance to heterogeneously catalyzed reactions, the knowledge gained has implications for many related fields. In the closely related area of stability of heterogeneous catalysts in aqueous reaction systems, polyols, model lignin compounds, and lignin have been shown to drastically enhance the stability of γ-Al_2O_3 supported metal catalysts against hydrolytic attack.[29-31] The formation of multidentate alkoxy bound surface species like those observed in the present study are believed to block sites for hydrolytic attack by hot liquid water, and thus stabilize the metal oxide support.

In the field of zeolite synthesis, polyols, are effective structure directing agents while synthesizing zeolite L.[95] In this case, the location of an alcohol group in a polyol had a large influence on how effectively the polyol modified the direction of crystal growth, where hydroxyls on the one and three carbons were most effective, analogous to the present study. Surface interactions of oxygen containing compounds with metal oxide

surfaces are also relevant to environmental and water quality research, as materials such as γ-Al_2O_3 are commonly found in soils and the aqueous phase interactions of oxygen containing toxic compounds are not fully understood and are an active area of research.[93] Having a better understanding of such surface chemistries will be critical to the development of sorbents that can bind toxic compounds with optimal specificity.

Finally, interactions of oxygen containing compounds and water on metal oxide and/or mineral surfaces are of great import to the pre-biotic organic chemistry community.[132-135] The experimental techniques utilized in this field, like surface-assisted laser desorption/ionization or desorption electrospray ionization mass spectrometry imaging,[132,133] are more traditional ultra-high vacuum surface science analytical techniques in that they do not lend themselves well to analyzing relatively high concentrations of water or probe molecules with low vapor pressures. The method used in the present study could provide complimentary information regarding the effects of bulk water on surface chemistries of multi-functional oxygen containing compounds on metal oxide surfaces.

3.5 Conclusions

Glycerol forms a multidentate alkoxide surface species on all of the metal oxides in the present study, which contain strong Lewis acid sites (LAS). In the case of MgO, the only material in the present study which lacks strong LAS, glycerol only experiences relatively weak hydrogen bonding interactions with the surface. This confirms that LAS are the active site for alkoxide bond formation. On all metal oxides containing strong LAS, glycerol adsorbs dissociatively forming a bridging alkoxy bond to a LAS from a 1° alcohol group, and engages in a non-dissociative Lewis acid/base interaction with a LAS

through its other 1° alcohol group. These strong LAS are not blocked by adsorbed water and retain their activity for forming bonds to glycerol. The frequencies of the νCO vibrations of the 1° alcohol groups participating in these interactions scale linearly with the electronegativity of the metal atom of the metal oxide. The glycerol surface species has an additional surface interaction via a hydrogen bond from its 2° alcohol group with a metal oxide basic surface oxygen atom provided that the oxygen atoms are not so strongly basic that they are poisoned by adsorbed water and/or CO_2. This hydrogen bonding interaction is prevented by coadsorbed water if the metal oxide basic surface oxygen atoms are of intermediate basic strength, as is the case in TiO_2. The role of the basic surface hydroxyls in interacting with the glycerol molecule is largely limited to relatively weak hydrogen bonding interactions.

CHAPTER 4

IN SITU ATR-IR STUDY ON AQUEOUS PHASE REFORMING REACTIONS OF GLYCEROL OVER A Pt/γ-Al_2O_3 CATALYST

4.1 Background

The need to replace petroleum derived chemicals with ones that can be produced in a renewable and carbon neutral fashion has resulted in a large body of research dedicated to converting biomass into value added products.[44,45] Of the myriad ways to upgrade biomass, heterogeneously catalyzed aqueous phase reforming (APR) has shown great promise for the production of H_2 and various alkanes using several biomass derived oxygenates and metal supported catalysts.[15,17,22]

Pt/γ-Al_2O_3 is among the most studied catalysts for these APR reactions.[18,26,39,47,136-139] One study investigated the APR kinetics of various biomass derived oxygenates using a 3 wt% Pt on γ-Al_2O_3 and found that selectivity toward hydrogen production increased in the order: glucose < sorbitol < glycerol < ethylene glycol < methanol.[26] The alkane selectivity followed the opposite trend. The mechanism behind these trends was not fully explored. Multiple experimental and theoretical studies have shown that dehydrogenation is the first reaction that various polyols undergo during APR.[38,140-142] In the case of APR of ethylene glycol over Pt, dehydrogenation is believed to be followed by C-C bond scission and water-gas shift (WGS) to yield CO_2 and H_2 as the final products.[47] However, in the presence of acidic sites, dehydration reactions occur in parallel with dehydrogenation.[38] Dehydration reactions are followed by

tautomerization, and then various other reactions including decarbonylation, and decarboxylation. This more complex reaction network leads to a much more diverse product distribution than when dehydrogenation reactions dominate. A comparison of the APR kinetics of ethylene glycol and methanol found that C-C bond cleavage is not the rate limiting step in these reactions, and that the reaction order was negative with respect to hydrogen, suggesting that adsorbed hydrogen was bonded to active sites on the Pt.[47] Removal of CO from the surface via WGS has been reported as the rate limiting step in APR over supported Pd, and inhibition by adsorbed hydrogen and CO species on Pt has also been shown to occur.[142]

Such kinetic studies have provided great insight into the APR reaction pathways and kinetics of various biomass derived oxygenates, however in situ vibrational spectroscopic techniques have the potential to provide additional insight into the fundamental reactions steps that occur on the catalyst surface. Knowledge of the nature of surface intermediates and the rates of their formation and consumption will be essential to understanding reaction pathways and kinetics of APR. This understanding will be critical for designing catalysts for APR. Note that comparable studies have been crucial for the development of catalytic processes in petroleum refining.[28]

The liquid environment in APR poses a significant challenge for in situ spectroscopic studies. Water, a dense medium, with very strong absorbance in vibrational spectroscopy, absorbs light in several important regions in the mid-IR range. This problem is further compounded by the very strong absorbance that most metal oxides, including γ-Al_2O_3, exhibit in parts of the mid-IR spectrum.[143] Most of these problems can be avoided by using in situ attenuated total reflectance infra-red (ATR-IR) spectroscopy.

This technique selectively probes the environment within a few micrometers from an internal reflection element (IRE). In typical ATR-IR studies of heterogeneous catalysts, a solid catalyst is immobilized on the IRE and a reactant solution is then flown over the catalyst layer during study. This experimental design eliminates the need to transmit directly through a reaction mixture, as with most conventional IR techniques.[144] As a result, ATR-IR is one of the most promising means of acquiring in situ spectroscopic data for heterogeneous catalysts in aqueous phase.[102] An in situ ATR-IR study of APR of methanol over Pt/γ-Al_2O_3 also found that hydrogen is likely co-adsorbed with CO on Pt during APR reactions, as evidenced through a redshift in the linearly bound CO signal.[39] However, no other spectroscopic evidence of chemisorbed hydrogen was presented. Another study investigated the kinetics and surface species that evolved during the APR of glycerol over 3 wt% Pt on γ-Al_2O_3, and witnessed two modes assigned to linear and bridging CO form on the Pt, but not at temperatures below 463 K.[38] While these studies illustrate the usefulness of ATR-IR as it applies to identifying surface species during APR reactions, they provide little information regarding the rates of the formation or consumption of the relevant surface species, or their role on the mechanism of APR.

An additional challenge in understanding the results of in situ ATR-IR studies of aqueous systems stems from the fact that catalyst layer pretreatments vary significantly from study to study. The pretreatment period has two main functions: to allow for the catalyst layer to mechanically reach a steady state under flowing solvent, and to remove any undesired molecules from the surface of the catalyst prior to the start of the experiment. The former issue is typically addressed by flowing the solvent used in the experiment, without any dissolved reactants, for several hours prior to the start of the

experiment.[38,144] After flowing a degassed solvent to establish a stable catalyst layer, a solvent flow with dissolved gases is sometimes used in order to chemically remove surface species from the catalyst. Dissolved H_2 can be used for removing surface oxygen species,[38,40,41] whereas dissolved O_2 can be used to oxidatively remove carbon containing surface species.[42] The presence of co-adsorbed CO, oxygen, and hydrogen on the Pt particles could have a pronounced effect on any subsequent in situ ATR-IR study. Such effects have yet to be studied rigorously. Consequently, the effect of different catalyst layer pretreatments on the kinetics of APR must be established in order to fully understand the results of such experiments.

In this study, in situ ATR-IR spectroscopy is used to investigate the effect of different pretreatment or cleaning procedures on the formation and removal of surface species on 5 wt% Pt/γ-Al_2O_3 in an aqueous environment. Aqueous phase reforming of glycerol is studied over Pt/γ-Al_2O_3 after different catalyst layer pretreatments. Specifically, the rates of formation and conversion of linear and bridging CO on the Pt surface are analyzed.

4.2 Materials and Methods

Glycerol (99%) and 5 wt% Pt on γ-Al_2O_3 were purchased from Sigma Aldrich and were used as received. Deionized water was further purified using a Barnstead NANOpure ultrapure water system to 18.2 MΩ/cm. X-ray diffraction (XRD) measurements were performed with a Philips X'pert diffractometer using a X'celerator module that utilized Cu Kα radiation. Diffractograms were collected at incident angles from $2\theta = 5°$ to 70° with a step size of 0.0167°. Nitrogen physisorption measurements were conducted with a Micromeritics ASAP 2020 Physisorption Analyzer. Prior to

analysis, samples were degassed under vacuum at 250 °C for 4 h. The BET surface area was calculated from the adsorption isotherm in the region $0.05 < P/P_0 < 0.3$. Average pore diameters were calculated using the BJH method in the region $0.05 < P/P_0 < 0.99$.

Pyridine adsorption followed by IR spectroscopy was performed using a Thermo-Nicolet 8700 FT-IR spectrometer with a MCT/A detector. Each spectrum utilized 64 scans at a resolution of 4 cm^{-1}. The catalyst was pressed into a self-supported wafer and loaded into a custom built vacuum chamber. The catalyst wafer was activated at 500 °C and < 10^{-6} mbar for 12 h. The temperature was then lowered to 150 °C when the background spectrum was collected, and then pyridine was introduced into the chamber at a pressure of 0.1 mbar for 30 min. The chamber was then evacuated for 30 minutes, the spectrum was collected, and the relevant peaks were integrated. The density of the wafer was determined by weighing a cutout of the wafer with a diameter of 6.35 mm, after the experiment. The concentration of acid sites was based on with the integrated area of the peaks, the area density of the wafer and the molar extinction coefficients reported by Datka et al.[50]

^{27}Al MAS-NMR measurements were carried out with a Bruker DSX 400 spectrometer. 4 mm zirconia rotors were used and were spun at 12 kHz. The resonance frequency for ^{27}Al was 104.2 MHz. A $\pi/12$ pulse was used, and the recycling delay was 250 msec. For each spectrum, a minimum of 2400 scans were accumulated. Aqueous $Al(NO_3)_3$ was used as a reference compound (δ = 0 ppm). Transmission electron microscopy (TEM) images were recorded with a JEOL 100CX microscope using a 100 kV acceleration voltage. The samples were prepared by applying a catalyst in ethanol slurry on a graphene coated, 200 mesh copper grid. The slurry was homogenized by

sonication for 15 min prior to applying to the sample grid. Pt particle size measurements utilized these micrographs.

In situ ATR-IR experiments were conducted on the previously mentioned spectrometer, with the same MCT/A detector. Each spectrum was collected with a resolution of 4 cm^{-1} and 64 scans. The heated ATR-IR cell was purchased from Pike Technologies and contained a ZnSe IRE. During the experiments, spectra were collected every 60 s. The catalyst layer was deposited on the IRE by applying a slurry of 12.5 mg of catalyst in 10 mL of ultrapure water, after the slurry had been agitated by a sonicator for 60 min. The water in the deposited layer was allowed to evaporate, and the process was repeated until all of the slurry was deposited. Aqueous solutions were pumped into the ATR-IR cell at a flow rate of 5.0 mL/min by an HPLC pump which drew from 4 different solvent bottles. The bottles typically contained ultrapure water degassed with He, aqueous glycerol solution (0.100 M) degassed with He, ultrapure water saturated with O_2 gas, and ultrapure water saturated with H_2 gas, henceforth referred to as H_2O, glycerol, $O_2(H_2O)$, and $H_2(H_2O)$, respectively. The liquids were saturated with the respective gasses for at least 4 h prior to the start of each experiment. All of the gases used were ultra-high purity grade (UHP, grade 5), and were purchased from Airgas.

Degassed, ultrapure water was flowed over the catalyst bed for 4 h prior to the start of an experiment when no O_2 or H_2 flow periods were used as a part of the pretreatment. The background was collected during water flow 5 min prior to the start of the experiment. When a dissolved O_2 or H_2 pretreatment cleaning period was used, the water was flowed for 3 hours, then the dissolved gas of choice was flowed for 30 min, followed by degassed water for 5 min, during the last minute of this 5 min water flow, the

background was collected, and then the experiment began. A typical experiment used 30 min flow periods that began with the glycerol solution, followed by water, and then dissolved oxygen. Any experiments that deviate from this flow program are clearly highlighted and explained in Chapter 4.3 when introduced.

The peaks in the spectra were integrated using Thermo Fisher Scientific Inc. GRAMS 9.1. The νCH region was used as an indicator of the presence of glycerol, and was integrated from ca. 3000 to 2775 cm^{-1}. The high wavenumber peak in the linear CO on Pt region was integrated from ca. 2125 to 2015 cm^{-1}, the low wavenumber peak in the linear CO on Pt region was integrated from ca. 2055 to 1875 cm^{-1} and the bridging CO on Pt peak was integrated from ca. 1870 to 1700 cm^{-1}, respectively. In cases where the two peaks in the linear CO on Pt region overlapped, peak fitting was used to deconvolute the peaks and find the respective areas.

4.3 Results and Discussion

4.3.1 Catalyst Characterization and Stability

The results from N_2 physisorption analysis and acid site characterization are summarized in Table 4.1. The diffractogram from the XRD analysis is shown in Figure C.1. This diffractogram exhibits two main peaks at 2θ = 44.6° and 66.7° which correspond to the (400) and (440) planes of the defective spinel crystalline structure of the γ-Al_2O_3 support.[73] The Pt particles were too small to be identified by XRD. TEM micrographs were used to determine an average Pt particle size of 3.9 nm based on measuring 177 Pt particles. The ^{27}Al MAS-NMR spectrum of the catalyst exhibits two main peaks at 7 and 63 ppm (Figure C.2), which are attributed to octahedrally and

tetrahedrally coordinated Al atoms, respectively. These resonances are typical for γ-Al_2O_3.[145] The octahedral and tetrahedral Al species comprised 77% and 23% of the total integrated area of these peaks, respectively. FT-IR analysis of the catalyst after pyridine exposure indicated that the catalyst had Lewis acidity as indicated by the peak at 1450 cm^{-1} (Figure C.3).[50] The lack of a peak at 1540 cm^{-1} indicates that the catalyst does not contain Brønsted acid sites (Figure C.3).

Table 4.1 N_2 physisorption and acidity measurement results for 5 wt% Pt/γ-Al_2O_3 catalyst

BET Surface Area	95.7 / m^2/g
BJH Adsorption surface area of pores	101.3 / m^2/g
BJH Desorption surface area of pores	119.3 / m^2/g
BJH Adsorption surface area of pores	0.237 / cm^3/g
BJH Desorption surface area of pores	0.222 / cm^3/g
Adsorption average pore width	9.8 / nm
Average Particle Size	62.7 / nm
Concentration of Lewis Acid Sites	18 / μmol/g

Using γ-Al_2O_3 as a support comes with the added complication of limited stability under APR conditions. γ-Al_2O_3 transforms into boehmite in hot liquid water,[30] although this stability issue has been shown to be less of a concern in aqueous biomass solutions.[31] Under the mild conditions used in the current study, this phase change is drastically slower than the time scale in which APR reactions occur on the catalyst surface. Therefore, it does not have a significant impact on the results of the current study.

4.3.2 Identification and Evolution of Surface Species During Cleaning Cycles

Spectroscopic studies on heterogeneously catalyzed conversion of any reactants require that the catalyst is prepared in well-defined and reproducible state before each

experiment. In studies on the surface interaction of volatile reactants, the catalyst is usually activated at elevated temperature in vacuum or an inert gas.[146] This procedure results in the removal of surface species and provides a clean surface for the main experiment. Pretreatment of catalysts for solution phase studies is more challenging because the catalyst is always exposed to the solvent along with reactants and products. Thus, it is not possible to prepare a surface that is entirely devoid of adsorbed molecules. Specific cleaning procedures were discussed in only a few studies.[42,147] Ortiz-Hernandez et al. described the accumulation of CO on $Pt/\gamma\text{-}Al_2O_3$ when this catalyst was exposed to H_2 saturated water, even though the solvent contained no carbon. Organic impurities in the catalyst layer were proposed as the source of the CO.[42] They also found that dissolved O_2 was effective at removing this CO. Ferri et al. found that impurities on Pt/Al_2O_3 can be removed by repeated cycles of flowing O_2 and H_2 dissolved in CH_2Cl_2.[147] This study also showed that H_2 in CH_2Cl_2 alone was not sufficient to remove impurities. In other studies Pt/Al_2O_3 catalysts were exposed to H_2 in gas phase prior to liquid phase ATR-IR experiment to remove any oxygen that may be on the surface of the supported metal particles.[38,40,41] The effectiveness of such a hydrogen treatment for the removal of carbon containing surface bound species that may have formed during the catalyst layer deposition was not discussed. In this context, it is important to point out that hydrogen strongly chemisorbs on Pt particles under APR conditions reducing the number of active sites.[39] A systematic understanding of the effect of different pretreatments on the formation of surface species on metal particles is an essential prerequisite for in situ ATR-IR studies on the kinetics of reactions like APR.

To illustrate the effect of different cleaning procedures on the surface of Pt/Al_2O_3 in an aqueous environment, the catalyst was subjected to different combinations of H_2O flow, $O_2(H_2O)$ flow, and $H_2(H_2O)$ flow. The pretreatment used for this experiment utilized 3 h of H_2O flow, followed by 30 min of $O_2(H_2O)$ flow, followed by 5 min of H_2O flow (Figure 4.1). The primary purpose of this pretreatment is to remove any loose catalyst particles, and allow the catalyst layer to reach a mechanically stable state. The O_2 flow used during the pretreatment period was used to eliminate carbonaceous impurities, including CO, that are known to form on Pt particles when exposed to atmosphere.[147] The background was collected during the final minute of the 5 min H_2O flow period, just prior to the start of the experiment so that the background captured a CO free Pt surface while minimizing any possible complications due to dissolved O_2 in the water found in the void space and the pores of the catalyst layer.

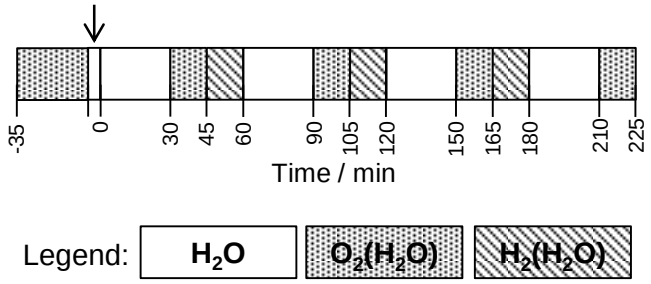

Figure 4.1 Flow periods used period used during the cleaning cycle experiment. Before the $O_2(H_2O)$ flow period that starts at -35 min, H_2O was flowed over the catalyst layer for 3 h, and is not shown. The black arrow indicates the time at which the background was collected.

The cleaning procedure investigated in this experiment consisted of multiple H_2O, $O_2(H_2O)$, and $H_2(H_2O)$ flow periods (Figure 4.1). IR spectra recorded at the end of each flow period are shown in Figure 4.2. The strong absorbance of the HOH scissor mode of

H_2O between 1800 and 1500 cm^{-1} makes resolving this region difficult, consequently this region of the IR spectrum is not shown. No notable changes were observed during the first H_2O and $O_2(H_2O)$ flow periods, (Figure 4.2 a and b). This indicates that the pretreatment with $O_2(H_2O)$ flow is an effective method for creating a stable, CO free Pt surface in an aqueous environment as a starting point for subsequent time resolved in situ ATR-IR experiments.

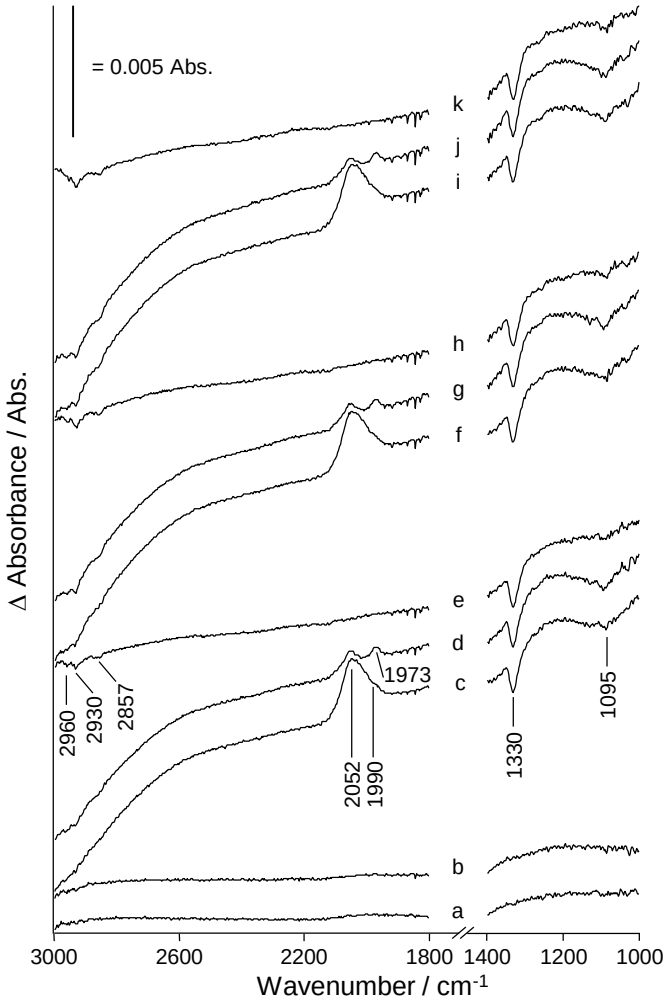

Figure 4.2 ATR-IR difference spectra of the catalyst layer during the cleaning cycle experiment. Spectra were recorded at the end of the following flow periods: first H_2O a), first $O_2(H_2O)$ b), first $H_2(H_2O)$ c), second H_2O d), second $O_2(H_2O)$ e), third $H_2(H_2O)$ f), third H_2O g), third $O_2(H_2O)$ h), fourth $H_2(H_2O)$ i), fourth H_2O j), fourth $O_2(H_2O)$ k).

Several new features evolved during the first $H_2(H_2O)$ flow period (Figure 4.2 c). A large decrease in absorbance was observed above 2600 cm^{-1}, which is assigned to the νOH mode of water. The decreasing absorbance above 2600 cm^{-1} during the $H_2(H_2O)$ period is likely due to dissociatively adsorbed hydrogen (H*), and possibly also adsorbed CO disrupting the water bilayer that is known to form on the Pt surface. H* at sub-monolayer coverages disrupts the water bilayer that forms on Pt.[148-150] This feature is induced by $H_2(H_2O)$ flow, remains during H_2O flow (Figure 4.2 d) and is reversed by $O_2(H_2O)$ flow (Figure 4.2 e). This demonstrates that H* species are formed under $H_2(H_2O)$ flow, remain during a subsequent H_2O flow, and are removed by $O_2(H_2O)$ flow. An experiment that utilized the identical flow pattern used in this experiment, but did not have a catalyst layer on the IRE did not exhibit this behavior (not shown). This eliminates the possibility that the behavior of the large feature above 2600 cm^{-1} is due to a change in the penetration depth of the evanescent wave caused by a change in refractive index of the liquid phase from the dissolved gas.

A negative peak at 1330 cm^{-1} is induced by $H_2(H_2O)$ flow (Figure 4.2 c). The only reasonable assignment for the negative peak at 1330 cm^{-1} is the δOH mode of a hydroxyl on the surface of Pt. This Pt bound OH group is likely formed from water during the pretreatment. It is negative because the $H_2(H_2O)$ flow removed this species. The νOH mode of this species cannot be resolved due to strong absorbance of H_2O in this region (3000 – 3600 cm^{-1}).

A peak at 2052 cm^{-1} with a shoulder at ca. 1990 cm^{-1} was also evident during $H_2(H_2O)$ flow (Figure 4.2 c). The stretching mode of CO linearly bound to Pt (νCO_L) is expected in this region of the spectrum when Pt bound CO is present in an aqueous

environment.[40,41] Deconvoluting the large peak at 2052 cm^{-1} and the shoulder at 1990 cm^{-1} into two peaks allows for the analysis of their evolution as a function of time (Figure 4.3). Peak fitting reveals that the integrated peak areas of the two modes in this region, centered at 2052 and 1990 cm^{-1}, appear at a similar initial rate and that the peak at 2052 cm^{-1} reaches a steady state value 5 min into this $H_2(H_2O)$ flow period. After the first 5 min., the peak centered at 1990 cm^{-1} exhibits a constant rate of appearance that is slower than in the first 5 min.

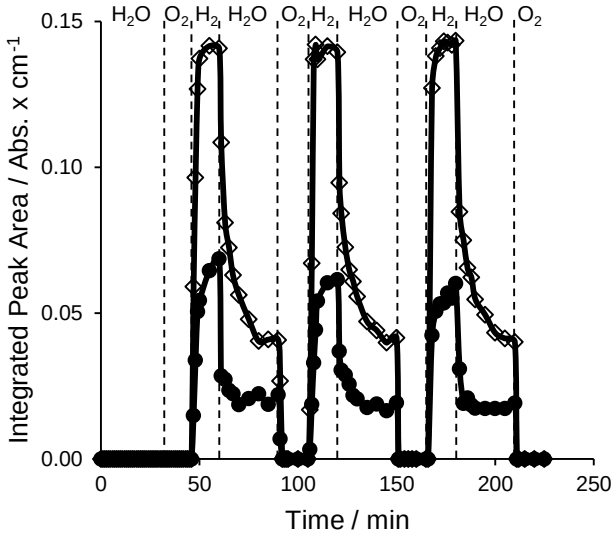

Figure 4.3 Integrated peak areas of νCO_L modes during cleaning cycle experiment. Each flow period is labeled at the top of the figure. O_2 denotes $O_2(H_2O)$ flow, H_2 denotes $H_2(H_2O)$ flow. CO_L/H, ◊ , was centered at ca. 2052 cm^{-1} peak. CO_L/H_2O, ●, was centered at ca. 1990 cm^{-1}.

The distinct νCO_L modes at 2052 and 1990 cm^{-1} suggest the existence of two unique CO_L species. Although it has been suggested that the higher wavenumber species could be due to a νPt-H mode from H* on Pt.[151-153] Ortiz-Hernandez et al. clearly demonstrated that the peaks observed at 2060 and 1990 cm^{-1} also develop on $Pt/\gamma\text{-}Al_2O_3$

in an aqueous environment upon exposure to D_2O saturated with D_2.[42] Consequently, the peaks cannot be attributed to νPt-H modes of H* on Pt. They concluded that these peaks were likely "trace amounts carbon monoxide or other carbonyl species" formed from impurities in the catalyst layer during H_2 flow. The exact identities of the two modes were not investigated. Furthermore, the νPt-H mode of H* adsorbed to "on-top Pt sites" is generally only observed by vibrational spectroscopy either at or near monolayer coverage in an ultra-high vacuum environment.[148] The near perfect agreement of the modes observed in the study by Ortiz-Hernandez et al. with those observed in the present work suggests that the modes observed near 2000 cm^{-1} in the present experiment are due to carbonyl species bound to the Pt. The lack of CH modes suggests that this carbonyl group is CO. The proximity of these peaks to other assignments of CO_L on Pt in aqueous phase, and the similarity of the two peaks' responses to changing dissolved gas flows suggests that they are both νCO_L modes of CO_L on Pt, but exist in environments different enough that they exhibit distinct νCO_L frequencies.

There are multiple factors that can influence the νCO_L frequency of CO adsorbed on Pt particles. The coordination number of the Pt atom to which a CO molecule is bound is known to have an effect on the observed νCO mode. It is generally agreed upon that CO adsorbed on Pt atoms with high coordination numbers that lie in exposed surface planes of Pt particles result in a νCO_L frequency that is higher than that of CO adsorbed Pt atoms with low coordination numbers that exist as edge sites.[154] Consequently, one possible explanation for the existence of the two unique νCO_L modes observed in the present work is that CO is formed from impurities in the catalyst layer during H_2 flow, which binds to platinum on planar and edge sites which give rise to two unique νCO_L

modes. However, evidence suggesting that this is not the cause for the two distinct νCO_L modes observed in the current study will be presented and discussed in detail in Chapter 4.3.3.

Another possible explanation is derived from the fact that coadsorbed species are also known to have a large influence on Pt bound νCO modes. Coadsorption of CO with H_2O on Pt (111) surfaces at one monolayer of H_2O and below leads to the formation of two regions with distinctly different concentrations of adsorbates, referred to as islands or regions.[155,156] One island is comprised purely of adsorbed CO molecules, and the other is a mixture of coadsorbed H_2O and CO. The strong dipole-dipole interactions of CO molecules in the CO rich island gives rise to higher frequency νCO modes, and the distinct νCO modes of these differently constituted islands can be resolved. However, increasing H_2O coverage leads to the complete disappearance of the CO rich islands, and the corresponding higher frequency νCO mode. In the present study, the Pt surface is surrounded by a very high concentration of water. Therefore, a region consisting of well mixed, coadsorbed CO and H_2O can explain only one of the two νCO_L modes observed here.

H* coadsorbed with CO on Pt surfaces can also induce island formation under certain circumstances, but is generally believed to form a single region of well mixed CO and H*.[156] Further evidence for the formation of a well-mixed domain of CO and H* is obtained from the fact that the peak centered at 2052 cm^{-1} (Figure 4.2 c), experienced changes in intensity without a change in frequency during the different flow periods (Figure 4.2 c, d, f, g, i, j). Increasing CO coverages in the cases of pure CO on Pt and CO with coadsorbed with H_2O induces a blueshift in the νCO mode due to increasing dipole-

dipole interactions.[41] H* coadsorbed with CO is known to strongly inhibit these dipole-dipole interactions, which results in a νCO_L mode frequency that is much less dependent on CO coverage.[156] Therefore, it is reasonable to conclude that the higher frequency peak, located at 2052 cm^{-1}, is attributed to the νCO_L mode of a region of CO_L on Pt interacting primarily with coadsorbed H* in a well mixed fashion. By contrast, the peak centered at 1990 cm^{-1} at the end of $H_2(H_2O)$ flow, experienced a redshift of 17 cm^{-1} when its integrated area was reduced by 68% by H_2O flow. This behavior suggests that the lower frequency νCO_L mode, centered near 1990 cm^{-1} at high CO loadings and at 1973 cm^{-1} at low CO loadings, belongs to a separate region of CO_L on Pt that interacts with coadsorbed H_2O in a well mixed fashion.

The exact positions of these two modes can also be explained by this model. Both of the νCO_L modes observed in this study are redshifted compared to where the νCO_L modes are typically observed on Pt in a vacuum environment at ca. 2100 cm^{-1}. This shift is due to a high concentration of H_2O molecules interacting with the Pt particles. The H_2O molecules donate electron density from a lone pair of electrons on the oxygen atom of the H_2O molecule to the Pt particle, which in turn donates electron density to the π bond system of the adsorbed CO. This weakens the C=O bond, and causes a redshift in all νCO frequencies observed.[41] The reason the νCO_L mode of the CO/H rich region is less redshifted, at a higher frequency, than the CO/H_2O rich region, is due to the lower local concentration of coadsorbed H_2O molecules, where instead coadsorbed H* atoms exist. As a result, less π-back donation occurs to the locally adsorbed CO, which results in a higher frequency νCO mode for the CO/H rich region.

The $H_2(H_2O)$ flow period was followed by the second H_2O flow period (Figure 4.1 and Figure 4.2 d). This H_2O flow caused a decrease in the integrated peak area of the $\nu CO_L/H$ mode at 2052 cm^{-1} to 29% of its original value by the end of the flow period (Figure 4.3). The $\nu CO_L/H_2O$ mode centered at 1990 cm^{-1} decreased to 32% of its value at the start of the H_2O period, and exhibited a 17 cm^{-1} red shift to 1973 cm^{-1} by the end of the H_2O period. The spectrum collected at the end of the second H_2O flow period (Figure 4.2 d), clearly illustrates the independent character two peaks in the νCO_L region, as they no longer overlap due to their decreased intensities. The negative peak at 1330 cm^{-1}, as well as the large, continuous decrease in absorbance above 2600 cm^{-1} remain evident in this spectrum, suggesting that the Pt bound H* and CO species prevent the return of the Pt bound OH groups even when dissolved hydrogen is not present.

$O_2(H_2O)$ flow followed the H_2O period and caused the disappearance of the two peaks attributed to νCO_L modes within 2 min (Figure 4.2 e and Figure 4.3). The CO was oxidized to CO_2, which in the presence of H_2O, left the surface as a carbonate species (Figure C.4). The negative peak corresponding to the δOH mode remained during this $O_2(H_2O)$ period, but the decreasing absorbance above 2600 cm^{-1} was no longer present. The return of a flat baseline indicates that all of the H* was oxidized to weakly bound H_2O. Even though the Pt surface appears to be free of adsorbed H* and CO, the Pt bound OH groups did not return (Figure 4.2 e). The fact that the negative δOH mode remains suggests that molecularly and/or dissociatively adsorbed oxygen could be present on the Pt particles along with molecularly adsorbed H_2O. These species could prevent the return of the Pt bound OH groups. The νPt-O modes of molecularly and dissociatively adsorbed oxygen species are known to form on Pt at 870 and 490 cm^{-1}, respectively.[157] However,

they cannot be resolved with the current experimental setup, as they are below the strongly absorbing phonon modes of the γ-Al_2O_3 support ca. 1200 cm^{-1}.[143,158] Additionally, three small negative peaks at 2960, 2930, and 2857 cm^{-1} attributed to aliphatic νCH modes are resolved. This indicates that the carbonaceous impurities in the catalyst layer are likely hydrocarbons, and are being removed by the cleaning cycles.

The cleaning cycle was repeated twice, and the spectra collected at the end of each flow period are shown in Figure 4.2 f – k. There is only one significant change in the peaks discussed in any given flow period with respect to additional cleaning cycles. The negative νCH modes at 2960, 2930, and 2857 cm^{-1} become more negative with each cleaning cycle. The rates at which the νCO_L modes appear increase with each additional cleaning cycle (Figure 4.3). In the second $H_2(H_2O)$ flow period, the νCO_L/H mode at 2052 cm^{-1} reaches the same integrated area as the first H_2 period, however it does so in 3 min rather than 5 min. During this same period, the $\nu CO_L/H_2O$ mode near 1990 cm^{-1} exhibits a fast initial appearance in the first 4 min followed by a significantly slower rate of increase to a maximum value by the end of the flow period. In the third $H_2(H_2O)$ flow period, the νCO_L/H mode reaches the same integrated area as the first two H_2 periods, however it does so in 2 min. The $\nu CO_L/H_2O$ mode again exhibits two distinct rates of appearance, a faster initial rate in the first 2 min, followed by a slower rate of increase until a maximum value is reached by the end of the flow period. Additionally, the integrated areas of the two peaks corresponding to the νCO_L modes decreased faster during the second and third $O_2(H_2O)$ flow periods relative to the first. The peaks disappeared within 2 minutes during the first $O_2(H_2O)$ period, and within 1 min during the second and third $O_2(H_2O)$ periods. The removal of the impurities results in a cleaner

Pt surface as evidenced by faster rate of formation of the two CO_L species during $H_2(H_2O)$ flow, and faster rate of removal during $O_2(H_2O)$ flow with each cleaning cycle.

The results of this experiment agree with the conclusion drawn by Ferri et al. in that multiple dissolved O_2 and H_2 cycles should be used in order to effectively clean the Pt surface.[147] It is clear in the present study that $O_2(H_2O)$ flow is the step that removes impurities from the Pt surface, and the $H_2(H_2O)$ flow appears to enable the formation of CO from impurities in the catalyst layer, in agreement with the study by Ortiz-Hernandez et al.[42] The discrepancy with respect to the exact role of the dissolved O_2 and dissolved H_2 periods is likely due to the different solvents used. Ferri et al. utilized CH_2Cl_2 as the solvent and concluded that H_2 was the cleaning agent, and O_2 induced CO formation by oxidizing impurities. The study by Ortiz-Hernandez et al. utilized H_2O as the solvent and found that H_2 induced the formation of carbonyls and O_2 removed the carbonyl species, cleaning the Pt surface. The present study also ultilized H_2O as a solvent and agrees with the findings of Ortiz-Hernandez et al. The possibility of the CH_2Cl_2 being a carbon source for CO formation during the dissolved O_2 flow period, which exhibited slower CO removal when compared to dissolved H_2 flow, also has to be considered. The present results illustrate that repeated $H_2(H_2O)$, H_2O, and $O_2(H_2O)$ flow periods remove carbonaceous impurities from the catalyst layer and result in a more reactive Pt surface.

4.3.3 Surface Species Formed During Glycerol APR

Before the relative kinetics of glycerol APR can be studied, the surface species that evolve during glycerol conversion must be identified. Adsorbed CO and H* are the most important surface intermediates in APR, but evidence of other species such as surface bound aldehydes or alkoxide groups may provide insight into the major side

reactions that occur during APR.[38] Moreover, even the different conformations of CO on Pt are known to have distinct behavior and kinetics during oxidative removal.[159-162] CO_B was shown to be more susceptible to oxidative removal than CO_L. It was proposed in these studies that oxidative removal of CO_B makes sites available for conversion of other CO molecules that diffuse to these active sites. The role of such sites on CO removal by WGS reactions is not as well understood.

To identify the surface species that evolve on the catalyst upon exposure to glycerol, a glycerol solution was flown over a catalyst bed deposited on the IRE. The pretreatment for this experiment consisted of a 4 h H_2O flow, at the end of this H_2O period the background was collected and then the experiment was begun. The flow program used for this experiment was 30 min glycerol flow, 30 min H_2O flow, 30 min $O_2(H_2O)$ flow (Figure 4.4 a). For reference, the IR spectrum of pure glycerol is shown in Figure 4.5 a.

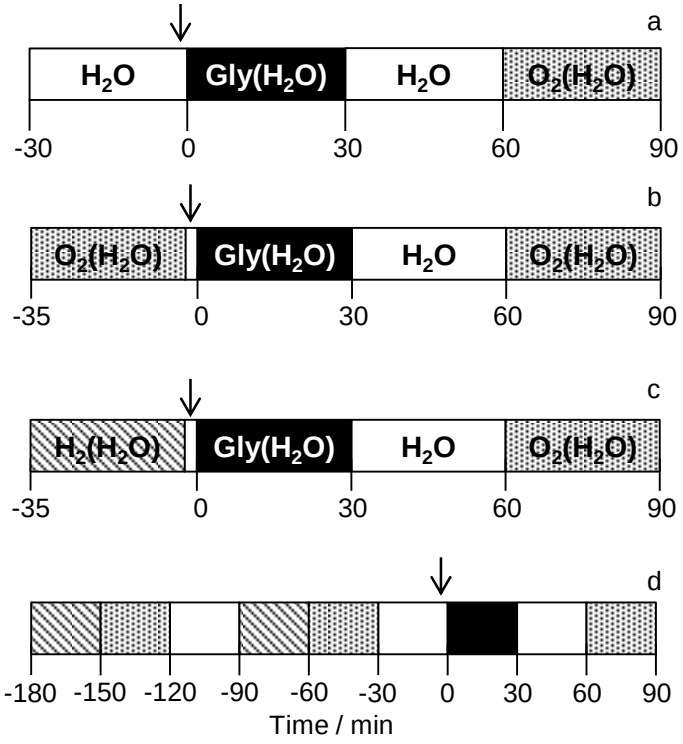

Figure 4.4 Flow compositions of different experiments: control experiment with H_2O pretreatment, a. $O_2(H_2O)$ pretreatment, b. $H_2(H_2O)$ pretreatment ,c. Two cleaning cycles, d. At least 3 h of H_2O flow preceded each experiment, and is not shown. Gly(H_2O) indicates, 0.100 M aqueous solution of glycerol. The black arrow indicates the time at which the background was collected.

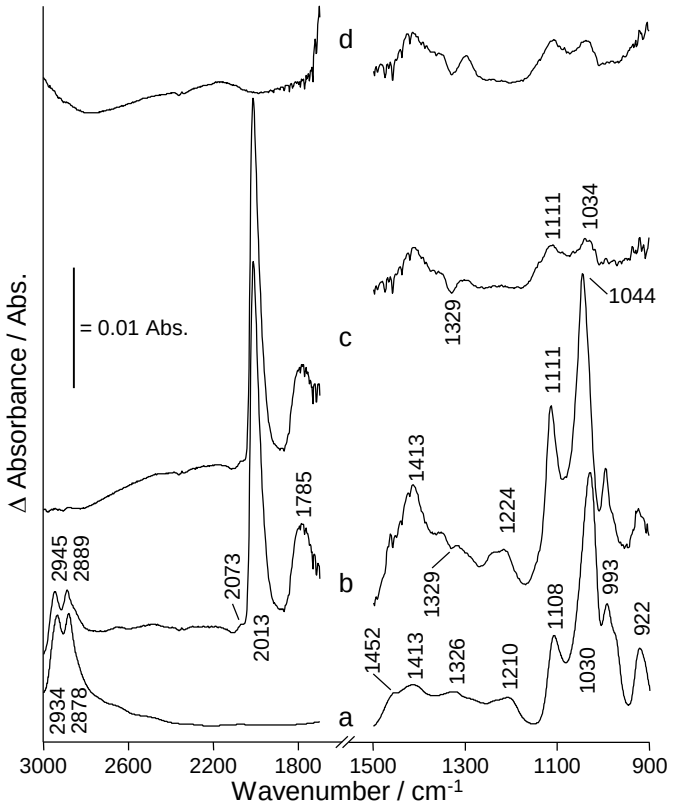

Figure 4.5 ATR-IR spectra of catalyst layer, subjected to a H_2O pretreatment period, during and after glycerol solution exposure. All of the spectra were collected at the end of their respective flow period. Pure glycerol is shown for reference, a). 0.100 M glycerol flowing over the catalyst, b). H_2O flow after the glycerol flow period, c). $O_2(H_2O)$ flow that followed the H_2O flow, d).

Upon exposure to glycerol, $\nu CO_L/H$, $\nu CO_L/H_2O$, and C-O stretching modes of bridging CO on Pt (νCO_B) initially appeared at 2073, 2006, and 1775 cm^{-1}, respectively (Figure 4.5 b). The spectrum collected at the end of the glycerol flow period (Figure 4.5 b) contained a weak $\nu CO_L/H$ peak at 2073 cm^{-1}, a strong and sharp $\nu CO_L/H_2O$ peak at 2013 cm^{-1}, and a νCO_B peak at 1785 cm^{-1}. A small, negative δOH mode at 1329 cm^{-1} is attributed to the removal of OH groups from the Pt surface. Note that this peak is superimposed on the δCH mode of glycerol at 1326 cm^{-1}. The other positive peaks are all

attributed to various modes of glycerol (Table 4.2) according to Colthup et al.[79] Table 4.2 also contains the shifts observed (Δ) relative to pure glycerol for 0.100 M glycerol in H_2O, and 0.100 M glycerol on the 5 wt% Pt catalyst layer. The small shifts observed in the modes of 0.100 M glycerol in water, and in water flown over the catalyst layer indicate weak interactions between glycerol and H_2O. Shifts of comparable magnitude were observed when glycerol interacted with the γ-Al_2O_3 support (Table 4.2). This indicates that the interaction of glycerol with γ-Al_2O_3 is mostly due to relatively weak van-der-Waals forces and/or hydrogen bonding as opposed to the chemisorption on Pt sites. Similar interactions have been reported for alkanes on solid catalysts.[163,164] In the case of 0.100 M glycerol on the catalyst layer, the peak near 1452 cm^{-1} is difficult to resolve due to its proximity to the HOH scissor mode of H_2O.

Table 4.2 Vibrational modes of pure glycerol, glycerol solution, and glycerol solution flown over the catalyst layer

Mode	Pure Glycerol / cm^{-1}	0.1 M Glycerol in H_2O / cm^{-1}	Δ / cm^{-1}	0.1 M Glycerol over Pt/γ-Al_2O_3 / cm^{-1}	Δ / cm^{-1}
$\nu_{asym}CH_2$	2934	2949	15	2945	11
$\nu_{sym}CH_2$	2878	2887	9	2889	11
δCH_2	1452	1458	6	-	-
δOH	1413	1418	5	1413	0
δCH	1326	1335	9	-	-
CH_2 wag	1210	1210	0	1224	14
νC-O 2°	1108	1111	3	1111	3
νC-O 1°	1030	1034	4	1044	14
CH_2 rock	993	993	0	993	0

The glycerol flow period was followed by a 30 min H_2O flow period, which removed the νCH_2 modes of glycerol completely (Figure 4.5 c). However, the δOH

mode, the νC-O mode of the secondary carbon (2°) and the νC-O mode of the primary carbons (1°) of glycerol remained at 1413, 1111, and 1034 cm^{-1}, respectively. The negative peak from the δOH mode of OH on Pt at 1329 cm^{-1} was again evident. The $\nu CO_L/H$, $\nu CO_L/H_2O$, and the νCO_B remained throughout the H_2O flow period. The fact that the 30 min H_2O flow did not remove the δOH, νC-O 2°, and νC-O 1° modes of glycerol suggests that at least a small amount of glycerol is irreversibly bound to the catalyst layer. As the $O_2(H_2O)$ period had no effect on the intensity or the position of these glycerol modes it is reasonable to assume that these carbonaceous species are not bound to the Pt particles. As explained above, Pt bound carbonaceous species are susceptible to oxidation under these conditions. Instead, it is likely that the residual carbonaceous species are adsorbed on the γ-Al_2O_3 support. This behavior was also observed when Pt/γ-Al_2O_3 was exposed to aqueous biomass solutions at 225 °C.[31] Irreversibly bound species were found to attach to surface hydroxyl groups on the support, and protect these sites from attack by hot liquid water[31] preventing the conversion of γ-Al_2O_3 into boehmite.[30] The combination of the optically dense liquid layer and the small concentration of these irreversibly bound glycerol molecules makes elucidating the exact nature of these species difficult. This will be the subject of a future study. Unlike the carbonaceous deposits on the support, the Pt bound CO species were completely removed during the 30 min $O_2(H_2O)$ period that followed the H_2O flow (Figure 4.5 d). However, the negative peak at 1329 cm^{-1} attributed to the δOH mode of OH on Pt remained. It is, thus, reasonable to assume that a substantial fraction of the Pt surface is covered by O_2 or dissociatively adsorbed oxygen, which prevents the return of the Pt bound OH group.

It is evident from Figure 4.5 that the activation of glycerol occurs over a 5 wt% Pt/γ-Al_2O_3 at room temperature and pressure. Even though a cleaning and/or reduction procedure was not used in the pretreatment for this experiment, the catalyst was still active for converting glycerol into CO, likely via dehydrogenation followed by decarbonylation. Unlike during the cleaning cycle experiment of Chapter 4.3.2, the Pt bound CO produced from glycerol is present as both CO_L and CO_B species. Either, the higher concentration of CO produced from glycerol compared to that from impurities could allow for the formation of CO_B species, or the lower concentration of hydrogen on the Pt could allow for the formation of CO_B. Whether CO binds to Pt in a linear or bridging conformation on a given Pt surface is typically not dependent on CO coverage in the absence of an applied electrochemical potential, but it depends on the types of sites available.[159-161] This suggests that the formation of CO_B in this experiment does not occur simply because of the higher CO coverage than in the previous experiment discussed in Chapter 4.3.2, but because H* is not occupying sites where CO_B forms. This also implies that the sites that preferentially bind H* species, also preferentially bind CO_B species.

The fact that the peak areas of the $\nu CO_L/H_2O$ and νCO_B species are much larger than that of the $\nu CO_L/H$ is expected as the coverage of CO is believed to be greater than that of H* due to very strong affinity of CO for Pt.[39,165] Glycerol is the most probable source of the H* on Pt, as Pt/γ-Al_2O_3 does not split H_2O well at 25 °C.[166] The reason that the $\nu CO_L/H$ and $\nu CO_L/H_2O$ modes are 21 and 23 cm^{-1} blueshifted relative to the glycerol free experiment in Chapter 4.3.2, respectively, is attributed to the displacement of molecularly adsorbed H_2O on Pt by a significantly larger CO coverage. The integrated area of the $\nu CO_L/H_2O$ mode in this experiment is 27 times that of the same mode in the

cleaning experiment. While integral areas of modes corresponding to νCO vibrations do not linearly correlate with the coverage of CO on the surface,[147,167] it is reasonable to conclude that the CO coverage in this experiment is much greater than in the previous experiment. As a result, there is less electron donation from the H_2O to the Pt particles, which results in less π back donation to the CO_L π system, and higher νCO frequencies.

Increasing glycerol conversion resulted in a drastic increase of the lower frequency νCO_L mode. Since CO adsorbed onto edge sites gives rise to the lower frequency νCO_L mode relative to CO adsorbed on terrace sites, one could suggest that the large νCO_L intensity in this experiment is due to a much higher concentration of CO on edge sites versus terrace sites. However, this interpretation would stand in exact juxtaposition to the known behavior of CO first populating edge sites and then populating the terrace sites with increasing CO coverage. The latter of these gives rise to the vast majority of the νCO_L signal.[168] Furthermore, both of the CO_L species develop simultaneously in the present study, not sequentially. These observations discount the possibility that the two distinct νCO_L modes are due to representing CO on edge and terrace sites, respectively. Instead, these two unique modes are attributed to the νCO_L modes of a region of CO_L in close proximity to H*, and another distinct region of CO_L in close proximity to coadsorbed water (see also Chapter 4.3.2.). It has to be noted that the coverage of CO species formed during the H_2O pretreatment period is unknown and that residual CO may affect the APR reaction.

As discussed in the introduction, the first step of APR is believed to be dehydrogenation in the absence of acid sites,[38,140-142] and a combination of dehydrogenation and dehydration when acidic sites are available.[38] As the γ-Al_2O_3

support used in the current study has Lewis acidity, the Pt/γ-Al_2O_3 catalyst may be capable of both dehydrogenation and dehydration pathways. A study that utilized in situ ATR-IR spectroscopy to investigate the APR of glycerol over a Pt/γ-Al_2O_3 catalyst found that both of these pathways occurred on the catalyst at 433 K and above, as there was evidence of both glyceraldehyde and hydroxyacetone on the catalyst.[38] The Pt bound CO was believed to have been formed from decarbonylation of any aldehyde containing intermediates. These species were not directly observed in the present study due to a combination of the strong absorbance of H_2O in the carbonyl region, and presumably due to limited concentration of these intermediates. At 25 °C, the rates of dehydrogenation and dehydration may be too low to produce a measureable amount of these species before they are decarbonylated to produce the observed Pt bound CO species.

4.3.4 Kinetics of Glycerol Conversion after Different Pretreatments

In gas phase reactions, it is commonly observed that different metal sites have a different activity for a specific catalytic reaction. In many cases spectroscopic studies allowed for identifying different adsorption sites and classifying them in terms of their activity in catalytic processes. For example, it was shown that highly active sites for WGS can be generated at the metal-support interface when alkaline earths promoters are added to Pt/TiO_2.[169] In addition, the role of well-dispersed metal cations as active sites for CO conversion has also been discussed.[170] It was also shown that the activity of supported Pt catalysts for CO oxidation is enhanced when the surface is partially or completely oxidized.[80] It is expected that similar differences in reactivity exist between different metal sites on APR catalysts. Moreover, the inevitable presence of coadsorbed reactants, products, and solvent requires particularly careful studies for reaction in

solvents. Therefore, it is crucial to pretreat the catalyst so that it is present in a well-defined, reproducible state in the beginning of the experiment.

Four experiments were carried out to investigate the role that different pretreatment procedures have on subsequent APR kinetics of glycerol. The control experiment utilized only H_2O flow for pretreatment, as described in Chapter 4.3.3. Three other experiments were carried out with different pretreatments, one with an $O_2(H_2O)$ period, one with a $H_2(H_2O)$ period, and one with two repetitions of $O_2(H_2O)$, $H_2(H_2O)$, and H_2O cycles (Figure 4.4 b-d).

The formation of CO_L and CO_B species from glycerol was observed after all pretreatments. However, the maximum coverages and rates of formation of these species strongly depended on the pretreatment procedure used. For the control experiment, which only utilized H_2O flow as a pretreatment, the integrated area of the $\nu CO_L/H$, $\nu CO_L/H_2O$, and νCO_B modes increased immediately upon admission of glycerol into the cell and nearly reached a steady state value by the end of the glycerol flow period (Figure 4.6, Figure 4.7, and Figure 4.8). The data points collected in the first 30 min glycerol exposure were fit to a first order step response function, $I = A\left(1 - e^{\left(-t/\tau\right)}\right) + I_0$, with a least squares regression (Table 4.3): in the first order step response function, I is the integrated area of the peak, A is a fit parameter, t is time in minutes, τ is a fit parameter, and I_0 is the initial integrated area, 0 Abs. x cm^{-1} in the case of these experiments. The A parameter is the steady state integrated peak area, and τ is the time it takes for the integrated peak area to reach ~63% of the A value. This τ parameter provides a semi-quantitative comparison of CO formation rate kinetics.

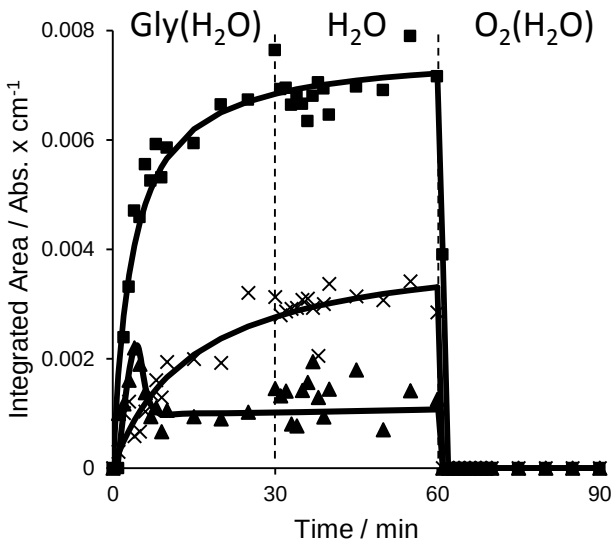

Figure 4.6 Integrated peak areas of the $\nu CO_L/H$ mode as a function of time and pretreatment period used. H_2O pretreatment, X. $O_2(H_2O)$ pretreatment, ■. Multiple cleaning cycles pretreatment, ▲.

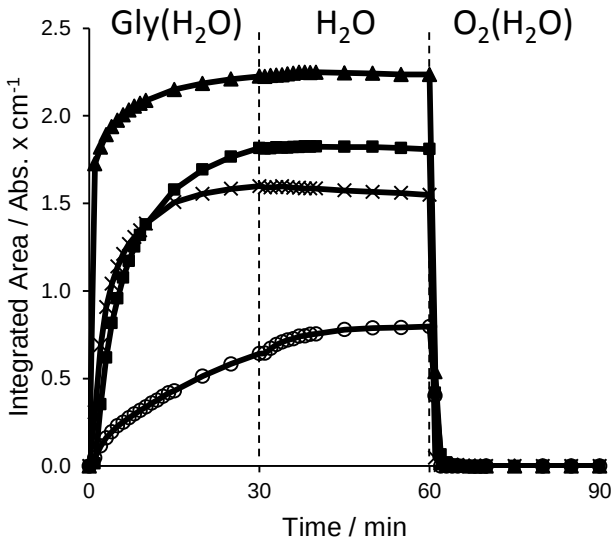

Figure 4.7 Integrated peak areas of the $\nu CO_L/H_2O$ mode as a function of time and pretreatment period used. H_2O pretreatment, X. $O_2(H_2O)$ pretreatment, ■. $H_2(H_2O)$ pretreatment, ○. Multiple cleaning cycles pretreatment, ▲.

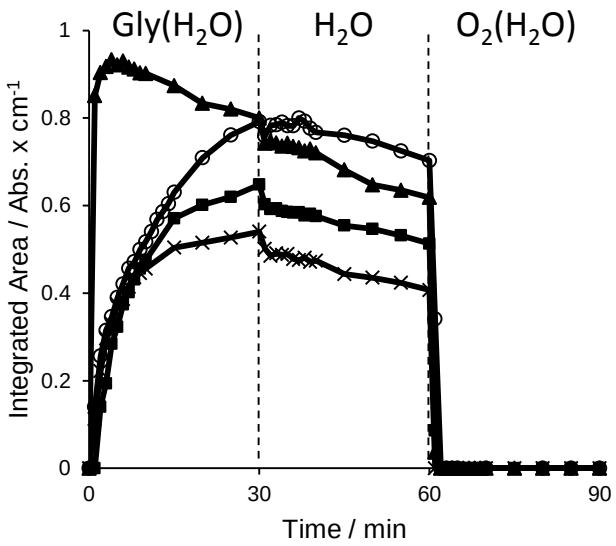

Figure 4.8 Integrated peak areas of the νCO_B mode as a function of time and pretreatment period used. H_2O pretreatment, X. $O_2(H_2O)$ pretreatment, ■. $H_2(H_2O)$ pretreatment, ○. Multiple cleaning cycles pretreatment, ▲.

The oxygen pretreatment resulted in larger integrated areas at steady state for all three of the Pt bound CO species by the end of the 30 min glycerol period relative to the H_2O pretreatment (Figure 4.6, Figure 4.7, Figure 4.8, and Table 4.3). This is attributed to higher surface coverage of the adsorbed species, as the $O_2(H_2O)$ period removed CO species from the Pt surface prior to the glycerol exposure. The initial rates of formation of CO_L/H_2O and CO_B are reduced relative to glycerol conversion after H_2O pretreatment, and the rate of CO_L/H formation is increased, as witnessed by their respective τ values. The decreased rate of CO_L/H_2O and CO_B is attributed to the residual Pt bound oxygen from the $O_2(H_2O)$ pretreatment period discussed in Chapter 4.3.2. These surface oxygen species convert the initial CO species formed from glycerol to loosely bound CO_2 that is subsequently desorbed. As the oxidative removal of CO from the Pt surface is much faster than CO formation (see Chapter 4.3.2), the residual surface oxygen results in a

slower apparent rate of CO formation. Since the control experiment began with some amount of CO on the Pt surface from the impurities in the catalyst layer, the observed rate of formation and saturation coverage of CO_L/H was reduced by the CO_L/H species present at the onset of the control experiment. Furthermore, integration of the CO_L/H mode during glycerol flow is particularly susceptible to error caused by the pre-existing CO species because both of these species give rise to peaks with similar size and frequency. By contrast, the CO_L/H_2O peak formed during glycerol exposure is significantly larger than during pretreatment, and is not affected to a significant extent. It should be noted that the τ value for the νCH_2 modes of glycerol, used as an indicator of the presence of glycerol in the catalyst layer, was typically about 0.1 min. This value is much smaller than any of the τ values of the CO species in this experiment. Consequently, it is safe to assume that the rates observed in this study are not limited by mass transfer of glycerol from the bulk fluid diffusing through the catalyst layer.

Table 4.3 First order step response function fit parameters for Pt bound CO species with different pretreatment procedures.

	None		O_2		H_2		Multiple Cycles	
Species	A / Abs. x cm^{-1}	τ / min	A / Abs. x cm^{-1}	τ / min	A / Abs. x cm^{-1}	τ / min	A / Abs. x cm^{-1}	τ / min
CO_L/H	0.0031	12.2	0.0069	4.7	-	-	-	<1.0
CO_L/H_2O	1.5	3.8	1.8	7.2	0.7	14.9	2.1	0.6
CO_B	0.5	4.0	0.7	7.6	0.7	5.9	-	<0.5

Glycerol exposure following the H_2 pretreatment experiment did not result in a measureable amount of CO_L/H (Figure 4.9 a). This is because the Pt surface was saturated with this species from the $H_2(H_2O)$ pretreatment period, as was the case during

$H_2(H_2O)$ exposure in Chapter 4.3.2. Consequently, there was no additional formation of CO_L/H during glycerol exposure. The CO_L/H_2O species exhibited a significantly decreased maximum integrated area and rate of formation relative to the H_2O and $O_2(H_2O)$ pretreatments. The reduced rate of CO formation is attributed H* blocking glycerol from active Pt sites. Likewise, it is proposed that the reduced saturation coverage of CO is due to H* competitively adsorbing with CO binding sites. Although the surface coverage of H* is higher in the current study due to the mild temperature, these observations agree qualitatively with the negative reaction orders with respect to hydrogen for this system observed in other studies at elevated temperature.[38,39,47] CO_B exhibits a rate of formation that is marginally slower than after the H_2O pretreatment and faster than after the $O_2(H_2O)$ treatment. The maximum integrated area of the CO_B species is larger than the value reached after H_2O pretreatment and similar to the value reached after the $O_2(H_2O)$ pretreatment. The decreased CO_L to CO_B ratio observed in this experiment, as well as the only slightly reduced rate of formation of CO_B, can be explained by the presence of H* co-adsorbed with CO. Coadsorbing H* with CO on Pt is known to decrease the νCO_L to νCO_B ratio by promoting the formation of different islands, in which CO is present in distinctly different environments.[156]

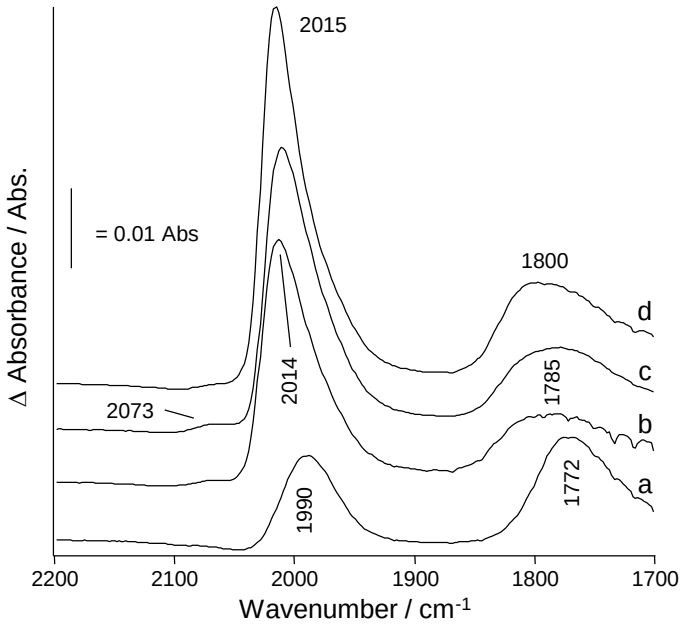

Figure 4.9 ATR-IR spectra of catalyst layer at the end of the glycerol exposure period of the different pretreatment experiments showing the Pt bound νCO region. $H_2(H_2O)$ pretreatment, a. H_2O pretreatment, b. $O_2(H_2O)$ pretreatment, c. Multiple cleaning cycles pretreatment, d.

The frequencies of the νCO modes at the end of the glycerol exposure period of the different pretreatment periods provide insight into interactions with coadsorbed species. The $\nu CO_L/H_2O$ and νCO_B modes of the glycerol exposure after the $H_2(H_2O)$ pretreatment (Figure 4.9 a) are redshifted 24 and 13 cm^{-1} relative to the control experiment (Figure 4.9 b). The redshift of the $\nu CO_L/H_2O$ mode is assigned to decreased dipole-dipole interactions resulting from a lower density of CO on the Pt surface relative to the control experiment. The νCO_B mode also experienced a redshift, but it coincided with an increase in the peak area. Ordinarily, dipole-dipole interaction would result in a blueshift as the concentration of surface CO increases.[156] The reason that a redshift was observed in this experiment is that H* formed during the pretreatment exists in close proximity to the CO_B species where it inhibits the dipole-dipole interactions.[156]

Multiple cleaning cycles used during the pretreatment resulted in the smallest integrated area of the CO_L/H peak by the end of the glycerol exposure, and the largest maximum integrated areas reached by CO_L/H_2O and CO_B. Additionally, the rate of formation of all three of the Pt bound CO species was the fastest with this pretreatment (Table 4.3 and Figure 4.6, Figure 4.7, and Figure 4.8). The increased rates of CO formation are attributed to the highest concentration of accessible Pt surface sites. In addition, the activity per site was increased relative to the other pretreatments. The increased number of available surface sites on Pt also resulted in the largest observed integrated areas for the CO_L/H_2O and CO_B species (Figure 4.9 d). The observed blueshifts relative to the other pretreatments is assigned to an increased density of CO on the Pt surface. Figure 4.6, Figure 4.7, and Figure 4.8 demonstrate that the pretreatment consisting of multiple cleaning cycles is particularly effective for sites that bind CO_B. A small number of sites on Pt particles preferentially bind CO_B species when exposed to gaseous CO.[160] These sites are also suggested to be the active sites for the oxidative removal of both CO_B and CO_L species from the Pt surface.[159-161]

The CO_L/H_2O species exhibited saturation behavior, as it was the case with this species with all of the other cleaning pretreatments. However, a different trend was observed for the rates of formation and coverages of CO_L/H and CO_B species. In all of the previously discussed pretreatments, the coverages of the CO_L/H and CO_B species exhibited saturation behavior, approaching a maximum value at the end of the 30 min glycerol exposure period. In the case of the experiment with multiple cleaning cycles, maximum areas for both of these peaks were reached after 4 min and were followed by a decrease in the integrated peak areas (Figure 4.6 and Figure 4.8). The area of the νCO_L/H

mode exhibited a sharp decrease from 4 to 7 min and then reached a constant value that lasted through the subsequent H_2O period. The CO_B species exhibited a more gradual, and linear decrease throughout the glycerol and H_2O flow periods. Interactions between the Pt bound CO species and other Pt bound molecules could alter the extinction coefficient of the Pt bound νCO modes. However, there is no evidence of unique surface species present due to this pretreatment. Therefore, it is proposed that the coverage maxima of the CO_L/H and CO_B species are not due to altered extinction coefficients of the respective νCO modes.

Instead, the maxima of the integrated areas of the νCO_L/H and νCO_B peaks are attributed to changes of the concentration of these species on the Pt surface. It is also suggested that this behavior requires unique sites that are only made available by the multiple cleaning cycles used in this experiment. The faster rates of formation and the higher integrated areas after this pretreatment indicate that this pretreatment provides the cleanest Pt surface in this study. Evidently, some of the Pt sites that are liberated by this cleaning procedure are the most reactive sites available, which explains their proclivity to react with carbon containing compounds in the atmosphere and become poisoned under mild conditions, room temperature and ambient pressure.

The decrease of the areas of the νCO_L/H and νCO_B modes after the maximum could be explained by desorption of CO, oxidation of CO to CO_2 by residual oxygen, or reorganization of the surface species and conversion of CO by WGS. Desorption of CO is an unlikely explanation because the areas of the CO_L/H and CO_B bands start to decrease while glycerol is still supplied as a CO source. Moreover, CO_L/H_2O sites bind CO less strongly than CO_B sites and should, thus, be the species to preferentially desorb.[171]

Additionally, CO_L/H_2O would be affected by oxidation with residual oxygen (Figure 4.7), but the integral of the corresponding peak remained constant during the H_2O flow period. The constant integral of the CO_L/H_2O band during H_2O flow along with the decreasing integrals of the CO_L/H and CO_B bands during the same period also discounts the possibility of a reorganization of the surface species. Therefore, it is concluded that CO_L/H and CO_B species are susceptible to conversion by WGS under the present conditions.

Initially, the rates of CO and H formation from APR of glycerol may be limited by mass transfer of glycerol from catalyst pores or void space to the Pt surface, as the τ values for the rates of formation of these species approach that of the appearance of glycerol. The present results indicate that the steady state for APR of glycerol is approached via a maximum surface coverage of CO_L/H and CO_B (Figure 4.6 and Figure 4.8). The decrease in the CO_L/H and CO_B species after 4 min indicates that CO species are being removed by WGS, and the rate of CO formation decreases. This suggests that H* is accumulating on these most active Pt sites, and is poisioning them from further CO formation or WGS reactions. In fact, with every pretreatment, the CO_B area decreased gradually while the CO_L/H and CO_L/H_2O species remained constant during the H_2O flow period that followed the glycerol flow period. This indicates that some of the sites that form CO_B species preferentially remove CO_B via WGS regardless of the pretreatment used.

Removal of CO by WGS was identified as the rate limiting step for APR reactions.[142] The findings of the present study support this conclusion. In addition, it is shown that the Pt sites which are cleaned by a combination of oxidative and reductive

aqueous environments are those which preferentially form CO_L/H and CO_B species from glycerol and are the most reactive sites for both CO formation from glycerol and WGS reactions. The WGS reaction occurs on these sites even at temperatures as low as 25 °C. The rate of the WGS at this temperature is slow relative to CO formation from glycerol, and the accumulation of Pt bound CO and H* species on the active sites limits the activity of the catalyst. The ability to compare the relative activities of CO formation and conversion by WGS allows for obtaining valuable insight into understanding the behaviors of catalysts for APR.

4.4 Conclusions

Pt/γ-Al_2O_3 shows a remarkable activity for conversion of glycerol in an aqueous environment at room temperature. The reaction leads to the formation of surface bound CO, and some of the CO species are even susceptible to water-gas shift at room temperature. Linearly bound (CO_L) and bridging CO (CO_B) on the Pt surface are identified as dominant surface species. Linearly bound CO exists in two unique environments, one where it is microscopically mixed with coadsorbed H* (CO_L/H), and another where it is microscopically mixed with coadsorbed H_2O (CO_L/H_2O).

The pretreatment procedure used for stabilizing and cleaning a 5 wt% Pt/γ-Al_2O_3 catalyst bed has a strong impact on the observed kinetics of APR of glycerol. A pretreatment that only consists of H_2O flow to stabilize the catalyst bed results in the formation of CO on the Pt surface. Pt bound CO species that are present after the pretreatment limit the number of active sites for glycerol activation. A pretreatment consisting of H_2O flow followed by O_2(H_2O) flow results in a CO free surface at the start of the APR reaction. However, residual Pt bound oxygen species initially react with

adsorbed CO_L/H_2O and CO_B species slowing the appearance of the corresponding IR bands. Pretreatment by H_2O flow followed by $H_2(H_2O)$ results in the slowest rates of CO formation because the adsorbed hydrogen blocks a substantial number of Pt sites at the onset of the glycerol flow. Multiple cycles of H_2O, $O_2(H_2O)$, and $H_2(H_2O)$ flow periods are the most effective cleaning pretreatment and result in the fastest rates of CO formation for all species. At the same time the highest concentrations of Pt surface sites is available for each CO species.

These most reactive Pt sites preferentially form CO_L/H and CO_B species from glycerol, until they become saturated with adsorbed reaction intermediates, namely CO_B and H*. The slow removal of the CO_B species during exposure to glycerol and H_2O indicates that these same sites are also the most active for WGS with notable activity at room temperature. The rate of CO formation from dehydrogenation of glycerol is limited by the lack of available Pt active sites due to high coverages of CO and H* species.

APPENDIX A

SUPPLEMENTARY INFORMATION FOR CHAPTER 2

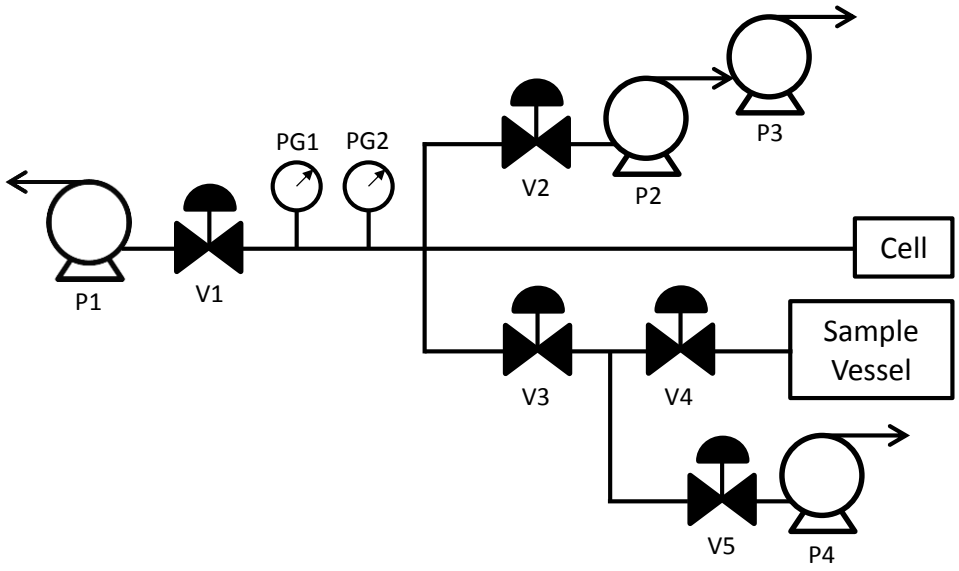

Figure A.1 Sketch of the high vacuum chamber used in the present study. P1 is a cryogenic pump, P2 is a turbo-molecular pump, P3 is a rotary vane pump, P4 is a membrane pump. V1 and V2 are 90° high vacuum valves, V3 is a leak valve, V4 is a high-vacuum glassware valve with a Viton o-ring that is part of the 50 ml sample vessel where water or other probe molecules are contained, V5 is a bellows sealed valve.

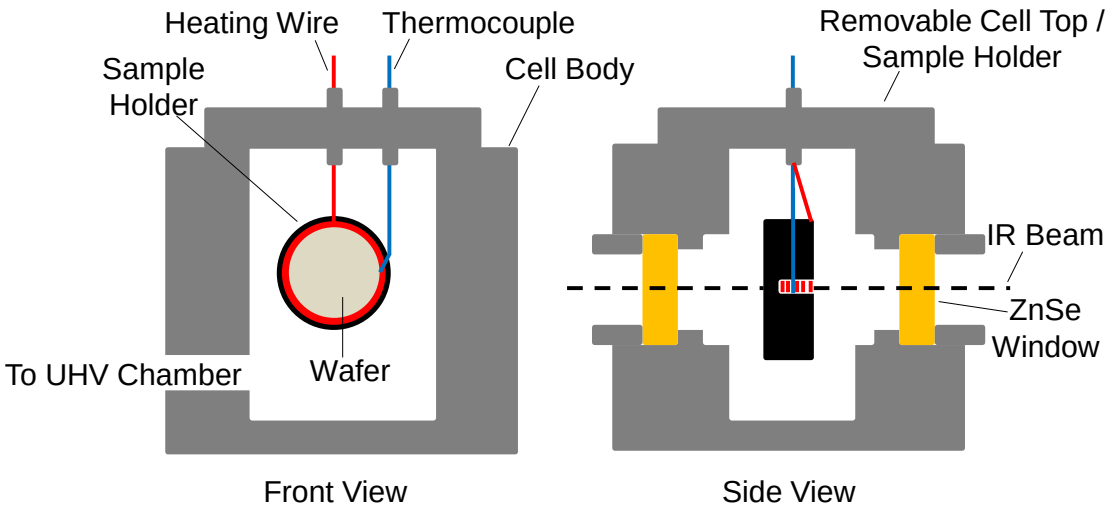

Figure A.2 Schematic of the in situ high vacuum transmission IR cell used in the present study. The ZnSe windows were sealed on either side of each window with custom made 1 mm thick PTFE gaskets (not shown). The heating wire and the thermocouple are soldered to the removable cell top / sample holder. The removable cell top / sample holder seals to the cell with a CF 40 flange and a copper gasket. The “To UHV Chamber” connection is a CF 16 flange with a copper gasket.

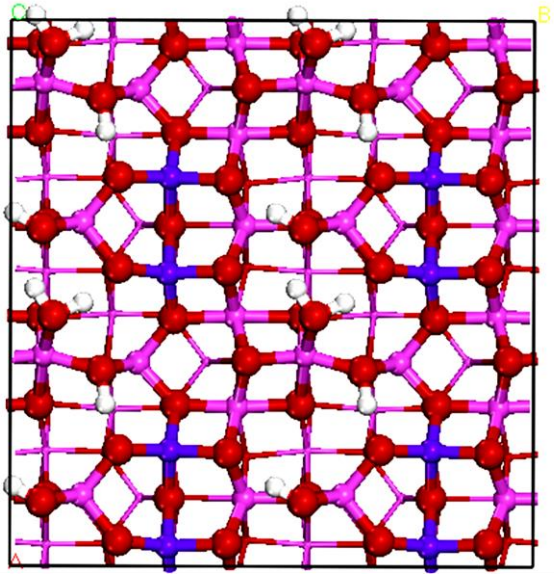

Figure A.3 Top view of the γ-Al_2O_3 surfaces used in this work: hydrated (110) surface with 5.9 OH/nm^2. Atoms in the first layer are shown in a ball and stick form with white (H), red (O), and pink (Al) balls. The surface unsaturated Al is marked by purple balls. The other layers are shown in a stick representation.

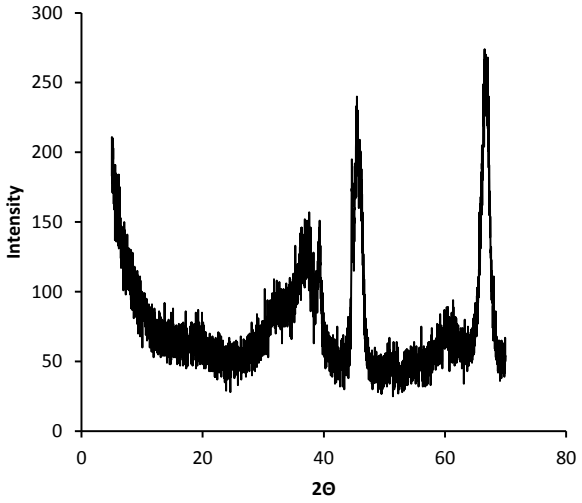

Figure A.4 XRD diffractogram of γ-Al_2O_3 used in the current study.

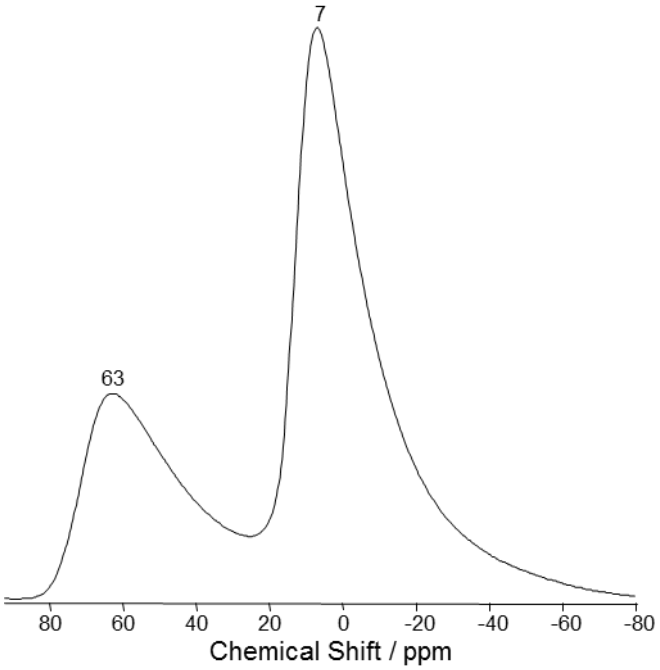

Figure A.5 ^{27}Al MAS-NMR of γ-Al_2O_3 used in the current study.

Table A.1 Select IR peak positions of pure oxygenates and oxygenates loaded on γ-Al_2O_3 in various environments.

	Ethylene Glycol / cm^{-1}				1,2-Propanediol / cm^{-1}				1,3-Propanediol / cm^{-1}				Glycerol / cm^{-1}			
	Pure	RTP	HV	H_2O	Pure	RTP	HV	H_2O	Pure	RTP	HV	H_2O	Pure	RTP	HV	H_2O
	2937	2937	2940	2940	2973	2970	2974	2973	2941	2933	2923	2928	2934	2934	2940	2940
	2874	2874	2922	2922	2930	2930	2964	2932	2880	2914	2910	2915	2878	2900	2922	2922
νCH		2850	2872	2881	2876	2876	2928	2876		2880	2860	2873		2880	2876	2879
			2845	2845		2855	2900	2855		2835				2855	2848	2852
						2815	2867	2815								
νOH			2713							2728	2722	2730			2717	
	1083	1131	1160	1131	1136	1145	1148	1145	1056	1144	1145	1144	1108	1151	1151	1152
	1033	1095	1131	1097	1077	1107	1095	1107	1034	1115	1120	1115	1030	1122	1125	1125
νCO		1058	1105	1062	1038	1084		1084		1074	1080	1074		1075	1083	1085
			1066			1057		1063								
								1055								

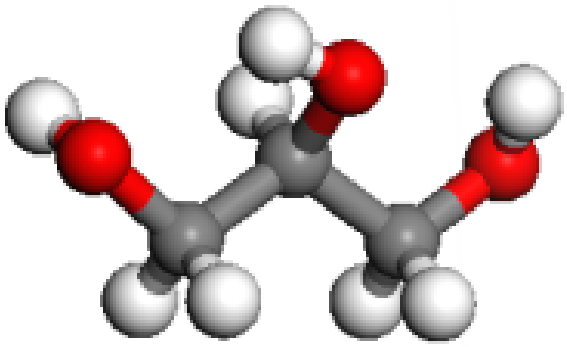

Figure A.6 A depiction of glycerol in the αα conformation. Grey balls are carbon atoms, red balls are oxygen atoms, and white balls are hydrogen atoms.

A.1 IR Spectra Normalization and Subtraction Procedure for Difference Spectra

The difference spectra were obtained using Thermo Fisher Scientific Inc. GRAMS 9.1 by the following procedure: Spectra of γ-Al_2O_3 wetted with pure water, rather than an oxygenate solution, were collected after the sample was subjected to the same vacuum and rehydration procedure as the oxygenate loaded samples. The area density of this sample was then collected. A spectrum of γ-Al_2O_3 impregnated with a solution of an oxygenate molecule of interest was divided by its area density, and then was multiplied by the area density of the γ-Al_2O_3 reference sample. This normalization makes subtracting samples with different area densities, and thus different wafer thicknesses valid. The spectrum of γ-Al_2O_3 impregnated with only water, at a given temperature and pressure, was then subtracted from the density normalized spectrum of the oxygen impregnated γ-Al_2O_3 at the same temperature and pressure. The resulting difference spectrum exhibits the differences that the presence of the polyol induced in the

hydrated γ-Al_2O_3 spectrum while eliminating the majority of the unchanging signal from γ-Al_2O_3.

A.2 DFT Experimental Details

All calculations were performed with plane-wave DFT[64] using the Vienna *ab initio* simulation package (VASP) with the PBE-GGA exchange-correlation functional[65] and the projector augmented wave (PAW) method.[66-69] To elucidate the role of the van der Waals interaction in this system, we also performed calculations using the PBE-D2 functional.[70] Spin polarization was employed for all calculations and the cutoff energy for the plane wave basis set was fixed at 400 eV. Geometry optimization was performed with a conjugate-gradient algorithm and considered to be converged when the forces on each atom become 0.03 eV/Å or less. Reciprocal space was sampled only at the Γ-point due to the large supercell. Numerical tests with more *k*-points changed the calculated adsorption energies by less than 2%.[71] Vibrational frequencies are evaluated by the harmonic approach. For comparison with experiment, the calculated frequencies for the glycerol adsorbates are scaled by factors of 1.008, which reflects the differences between measured and calculated frequencies of gas-phase CO molecules.

We adopted models for alumina surfaces from Ref.[72] According to this work, the (110) surface of *γ*-Al_2O_3 has the largest surface area among the surfaces present on the equilibrium crystal shape. The (110) surface has a hydroxyl coverage of 5.9 OH/nm^2 when *γ*-Al_2O_3 is prepared at 377-677 °C.[72] An illustration of this surface is shown in Fig. 1. This surface exposes unsaturated 4-coordinated Al atoms, whereas Al atoms in the bulk are 6-coordinated. To reduce lateral interactions between adsorbed molecules, we used a slab containing 2 × 2 unit cells in the plane of the surface and four layers normal

to the surface. With these choices, the computational supercells for the hydrated (110) surface contained 224 atoms.

For glycerol adsorption on the surface, we performed calculations for three distinct scenarios. First, we considered situations where glycerol binds to the surface only through one, two, or three H bonds. Second, we examined configurations where glycerol binds to unsaturated surface Al atoms via one, two, or three O-Al bond. Finally, we considered situations where the molecules bind to the surface through a combination of H bonds and O-Al bonds. All of our calculations considered isolated glycerol molecules on the surface; exploring the full range of possibilities that can arise when water is coadsorbed with glycerol was beyond the scope of these calculations.

Following the identification of the molecular adsorption of glycerol on surface, we then studied the dissociation of molecular glycerol into H and $C_3H_7O_3$ on the surface. Following the dissociation of adsorbed molecular glycerol into H and $C_3H_7O_3$, we performed calculations for three additional reactions: dissociation of another H on the surface, reaction of the dissociated H with a surface OH to release water into the gas phase, and recombinative desorption of the dissociated H to release H_2 into the gas phase. For each case, we considered numerous initial geometries. For brevity, however, only the most stable local minimum energy structures are presented.

A.3 Reaction Energy ΔE

For each reaction as shown in Figure 2.8 is calculated as following:

A.3.1 Molecular Adsorption

$$\Delta E = E_{tot}(\text{glycerol}/Al_2O_3) - E_{tot}(Al_2O_3) - E_{tot}(\text{glycerol})$$

where $E_{tot}(glycerol/Al_2O_3)$, $E_{tot}(Al_2O_3)$ and $E_{tot}(glycerol)$ are the total energy of optimized structure with glycerol molecule on the γ-Al_2O_3(110) surface, the γ-Al_2O_3(110) surface and the free glycerol molecule in the gas phase, respectively.

A.3.2 Dissociation of the First H

$\Delta E = E_{tot}(H\text{-}C_3H_7O_3/Al_2O_3) - E_{tot}(glycerol/Al_2O_3)$, where $E_{tot}(H\text{-}C_3H_7O_3/Al_2O_3)$ is the total energy of optimized most stable structure with glycerol molecule dissociated into one H atom and $C_3H_7O_3$ on the γ-Al_2O_3(110) surface.

A.3.3 Dissociation of the Second H

$\Delta E = E_{tot}(2H\text{-}C_3H_6O_3/Al_2O_3) - E_{tot}(H\text{-}C_3H_7O_3/Al_2O_3)$, where $E_{tot}(2H\text{-}C_3H_6O_3/Al_2O_3)$ is the total energy of optimized most stable structure with two separate H atoms and $C_3H_6O_3$ on the γ-Al_2O_3(110) surface.

A.3.4 Desorption of Surface H as ½$H_{2(g)}$

$\Delta E = E_{tot}(C_3H_7O_3/Al_2O_3) + ½\ E_{tot}(H_2) - E_{tot}(H\text{-}C_3H_7O_3/Al_2O_3)$, where $E_{tot}(C_3H_7O_3/Al_2O_3)$ and $E_{tot}(H_2)$ are the total energy of optimized most stable structure with $C_3H_7O_3$ species on the γ-Al_2O_3(110) surface and the free H_2 species in the gas phase, respectively.

A.3.5 Surface H Reacting with Surface OH and Leaving as $H_2O_{(g)}$

$\Delta E = E_{tot}[C_3H_7O_3/(Al_2O_3)_{(OH)vac}] + E_{tot}(H_2O) - E_{tot}(H\text{-}C_3H_7O_3/Al_2O_3)$, where $E_{tot}[C_3H_7O_3/(Al_2O_3)_{(OH)vac}]$ and $E_{tot}(H_2O)$ are the total energy of optimized most stable structure with $C_3H_7O_3$ species adsorption on the γ-Al_2O_3(110) surface with one OH vacancy and the free H_2O molecule in the gas phase, respectively.

A.4 Reaction Mechanism from PBE Calculation

The reaction mechanism including the most stable structure for each elementary step is shown in Figure A.7. As shown in Figure A.7, the PBE functional gives the same lowest energy surface species in each reaction step as the PDE+D2 functional shown in Figure 2.8 in the main text, but with slightly different adsorption energies. Dissociation of the first H at the surface yields the most favorable surface structure, and all further reactions considered were found to be unfavorable.

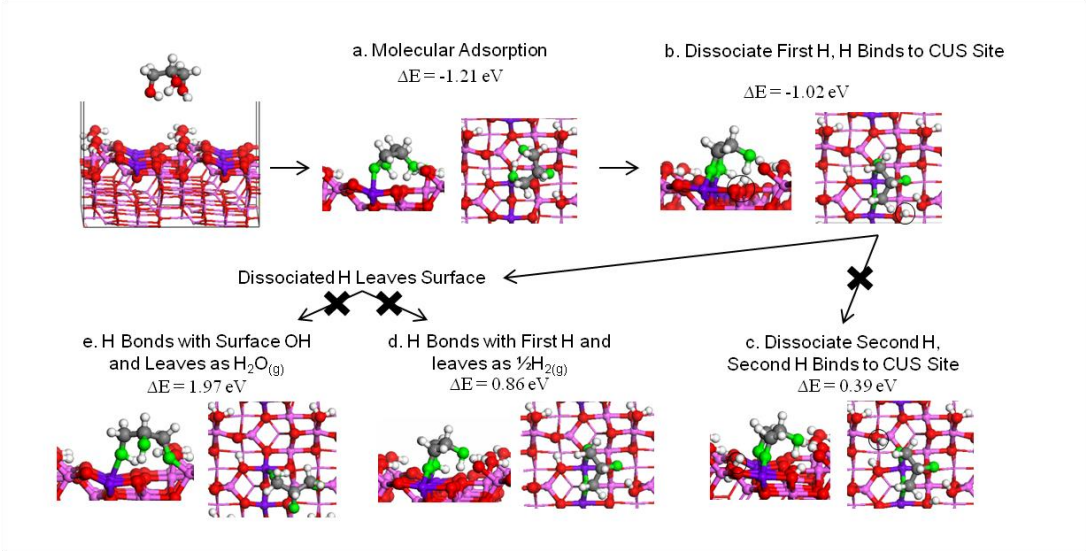

Figure A.7 Side and top views of the most energetically favorable surface species in the case of glycerol on γ-Al_2O_3(110) surface with energies relative to the previous scenario, a: molecular adsorption; b: single H dissociation; c: second H dissociation; d: single dissociated H leaving as $½H_{2(g)}$; e: single dissociated H bonding with a surface OH γ-Al_2O_3(110) surface and leaving as $½H_2O_{(g)}$. Small white balls: H; red balls: surface O; green balls: O of glycerol; gray balls: C; pink balls: Al atoms; purple balls: unsaturated surface Al atoms. The black cycle indicated the dissociated H from glycerol in that reaction step.

A.5 Comparison of the Most Stable Structures for PBE and PBE+D2 Methods.

As shown in Table A.2, including the van der Waals force correction using the PBE-D2 functional causes the H bond distances to become slightly shorter compared PBE calculations without van der Waals force correction.

Table A.2 Comparison of structures for PBE and PBE+D2 method as shown in Figure A.7 and Figure 2.8, the distance of O-Al bond formed between oxygen of glycerol and surface Al atoms (Å), the H bond distance between the glycerol and surface (Å).

a	d(O-Al) [Å]	d(H bond) [Å]
PBE	1.96	1.59,1.59,1.81
PBE+D2	1.92	1.49,1.53,1.84
b		
PBE	1.99,1.92,1.88	1.91,1.71,1.71,1.62
PBE+D2	1.98,1.91,1.88	1.71,1.65,1.62,1.53
c		
PBE	1.91,1.85,1.81	1.78,1.76,1.72,1.65
PBE+D2	1.91,1.85,1.81	1.67,1.70,1.65,1.56
d		
PBE	2.00,1.91,1.89	1.93,1.72,1.61
PBE+D2	1.98,1.91,1.89	1.77,1.69,1.54
e		
PBE	2.11,1.74	1.68,1.61,1.52
PBE+D2	2.01,1.73	1.64,1.58,1.45

Table A.3 Comparison of experimentally observed and literature values of vibrational frequencies of surface OH groups of γ-Al_2O_3. Number following μ indicates the coordination number of the OH group, and the numbers in the parenthesis indicate the Miller index of the plane in which the OH group exists.

ν / cm^{-1}	Knözinger et al.[90]	Digne et al.[72]
3772	OH- μ_1-Al_{IV}	OH- μ_1-Al_{VI} (100)
3730	OH- μ_2-Al_{VI},Al_{IV}	OH- μ_1-Al_{IV} (110)
3700	OH- μ_3	OH- μ_2-Al_{VI} (110)
3560	H bonded	OH- μ_3-Al_{VI} (100)

APPENDIX B

SUPPLEMENTARY INFORMATION FOR CHAPTER 3

Table B.1 Area densities in mg/cm^2 of the metal oxide wafers used for all of the in situ transmission IR experiments carried out in the present study.

	Adsorbate Molecule			
	Pyridine	CO_2	H_2O	Glycerol/H_2O
γ-Al_2O_3	28.8	11.5	12.1	7.1
basic γ-Al_2O_3	14.8	15.4	14.2	7.9
TiO_2	30.3	34.6	21.4	21.1
ZrO_2	35.0	36.8	30.4	41.9
Alfa ZrO_2	26.4	25.7	30.0	25.8
MgO	13.8	10.6	11.1	10.0
CeO_2	42.9	44.1	43.0	33.5

Table B.2 Metal Oxide N_2 Physisorption Results.

	BET SA / m^2/g	Pore Volume / cm^3/g	Pore Width / nm
γ-Al_2O_3	76.9	0.152	12.5
Basic γ-Al_2O_3	224.6	0.954	17.8
TiO_2	54.1	0.102	13.0
ZrO_2	99.1	0.078	3.8
Alfa ZrO_2	102.2	0.300	12.1
MgO	70.8	0.256	15.2
CeO_2	62.6	0.123	9.3

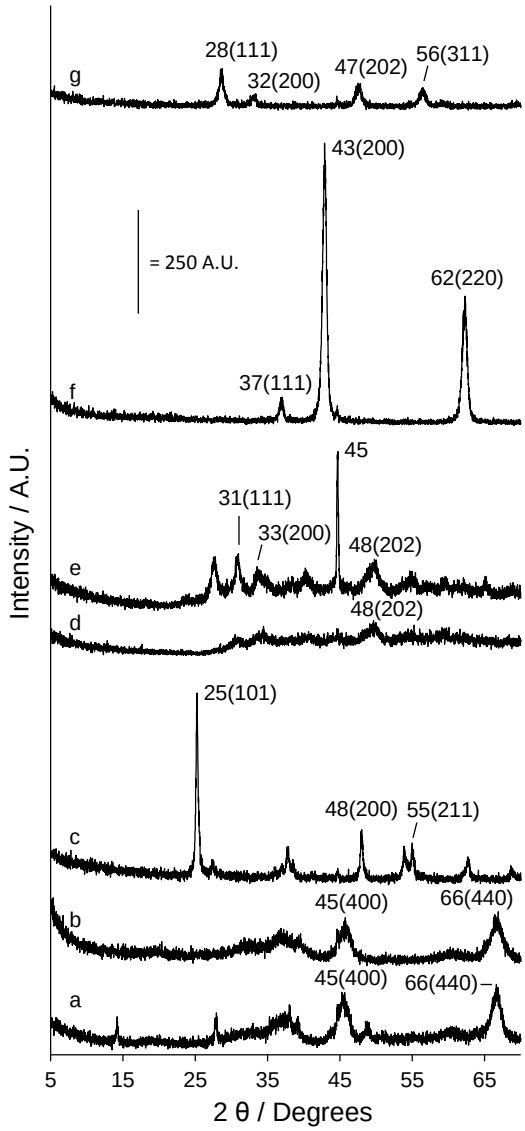

Figure B.1 XRD diffractograms of metal oxides. γ-Al_2O_3 (a), basic γ-Al_2O_3 (b), TiO_2 (c), ZrO_2 (d), Alfa ZrO_2 (e), MgO (f), CeO_2 (g). The numbers in parenthesis indicate the family of planes to which the corresponding peak is assigned.

Both γ-Al_2O_3 and basic γ-Al_2O_3 exhibit a diffractogram indicative of a largely amorphous defect-spinel structure (Fig S1 a and b, respectively).[30,73] TiO_2 exhibits diffraction peaks attributed to crystalline planes indicative of anatase phase (Fig S1 c).[172] ZrO_2 and Alfa ZrO_2 exhibit peaks attributed to tetragonal crystalline structure (Fig S1 d and e, respectively).[173] MgO exhibited diffraction peaks consistent with a NaCl type crystalline structure (Fig S1 f).[172] CeO_2 exhibited diffraction peaks consistent with a cubic structure (Fig S1 g).[173]

Table B.3 Total and strong acid site concentrations in $\mu mol/m^2$.

	γ-Al_2O_3	Basic γ-Al_2O_3	TiO_2	ZrO_2	MgO	CeO_2
Total Sites	0.27	0.07	0.08	0.05	0.09	0.32
Strong Sites	0.12	0.03	0.06	0.03	0.01	0.21

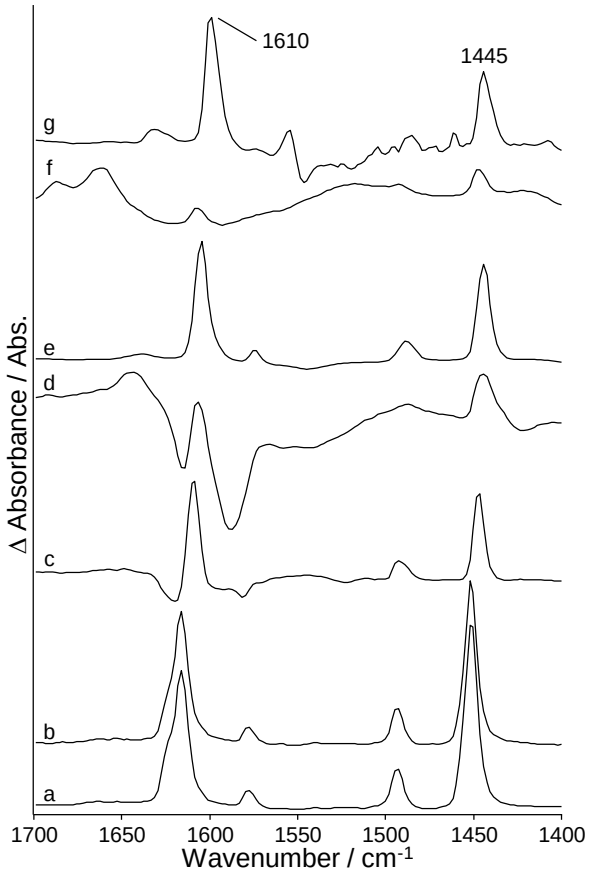

Figure B.2 IR difference spectra of pyridine on metal oxides after 200 °C desorption temperature. γ-Al_2O_3 (a), basic γ-Al_2O_3 (b), TiO_2 (c), ZrO_2 (d), Alfa ZrO_2 (e), MgO (f), CeO_2 (g).

The ν19b mode at ca. 1445 cm-1 and the ν8a mode at ca 1610 cm-1 of pyridine coordinated to Lewis acid sites[63] is evident in every metal oxide except MgO after having been exposed to pyridine, and then heated to a desorption temperature of 200 °C (Fig. S2). Note that the ν19b mode of pyridine coordinated to a Brønsted acid site, expected at ca. 1540 cm-1,[63] is not present in any of the spectra.

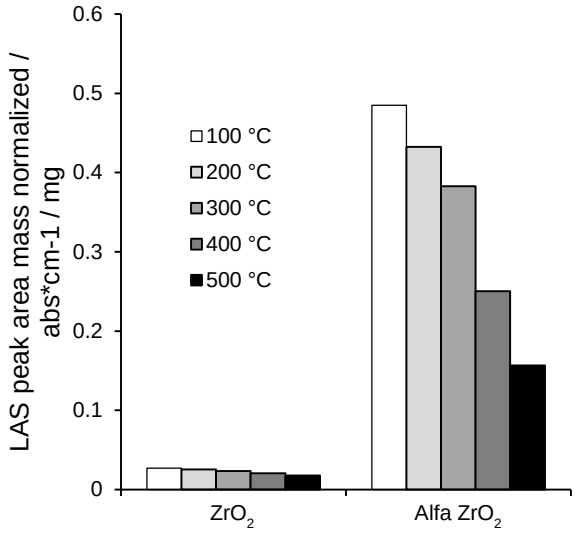

Figure B.3 Wafer mass normalized integrated peak areas of pyridine coordinated to LAS for the ZrO_2 samples.

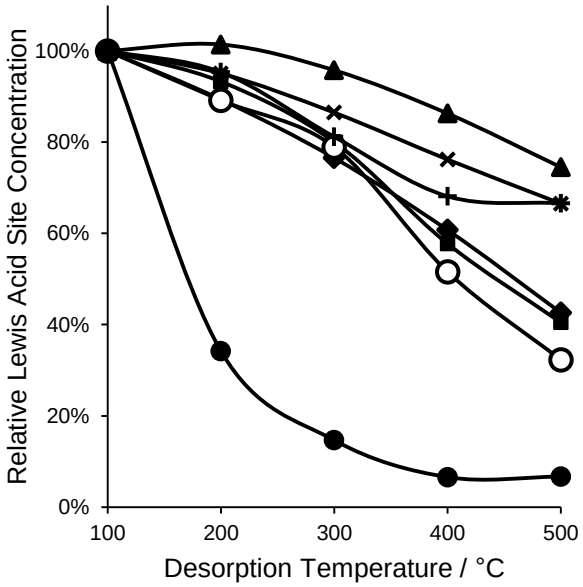

Figure B.4 Relative Lewis acid site concentration of the metal oxides as a function of pyridine desorption temperature. γ-Al_2O_3 (♦), basic γ-Al_2O_3 (■), TiO_2 (▲), ZrO_2 (X), Alfa ZrO_2 (○), MgO (●), CeO_2 (+).

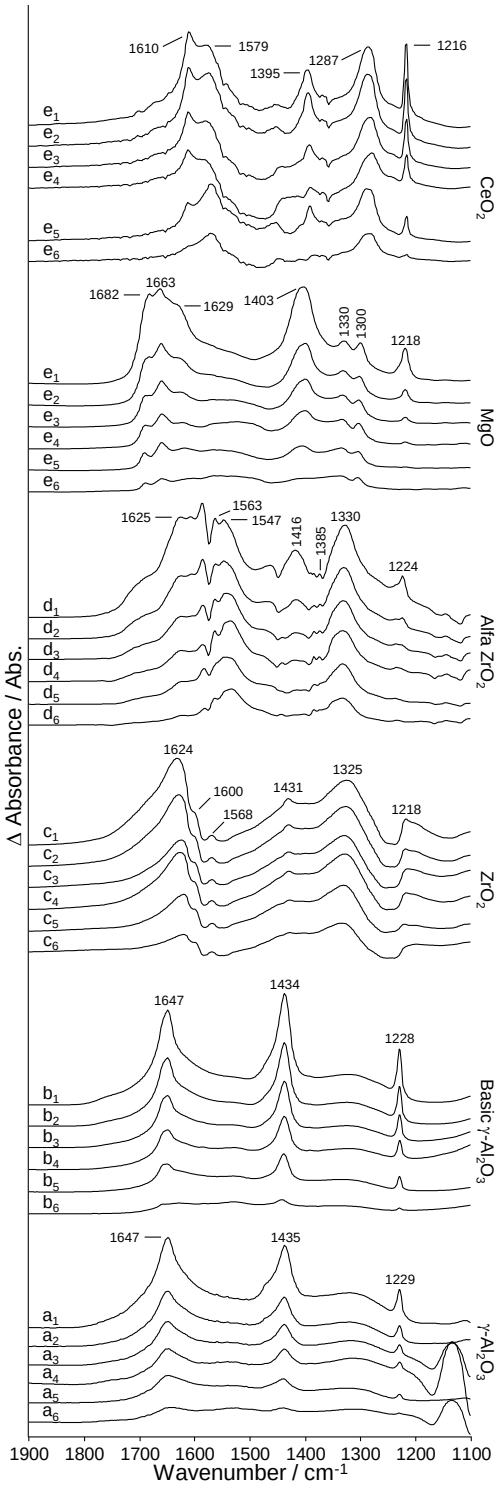

Figure B.5 IR spectra of the temperature programmed desorption of CO_2 from the metal oxides. The samples shown are γ-Al_2O_3 (a), basic γ-Al_2O_3 (b), ZrO_2 (c), Alfa ZrO_2 (d), MgO (e), and CeO_2 (f). The number in subscript denotes the highest desorption temperature that the sample was exposed to: 100 °C (1), 200 °C (2), 300 °C (3), 400 °C (4), and 500 °C (5).

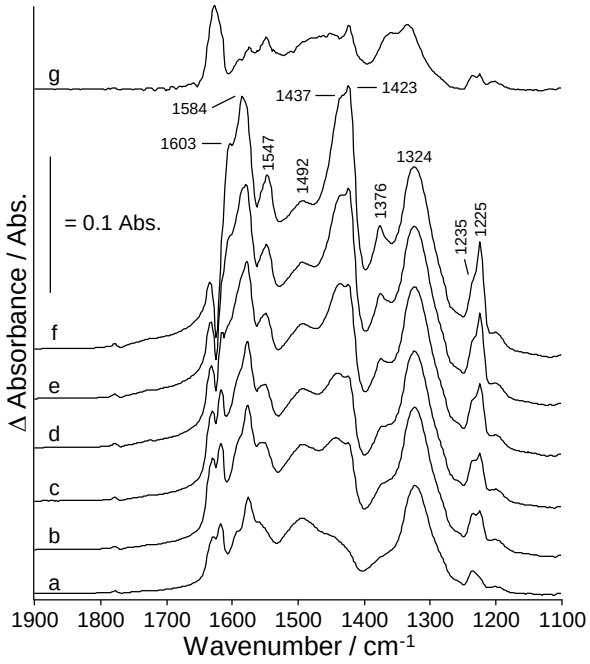

Figure B.6 IR spectra of CO_2 adsorption on TiO_2 at various pressures. CO_2 pressures as follows: 0.14 mbar (a), 0.51 mbar (b), 1.02 mbar (c), 2.53 mbar (d), 5.01 mbar (e), 10.02 mbar (f), UHV (g).

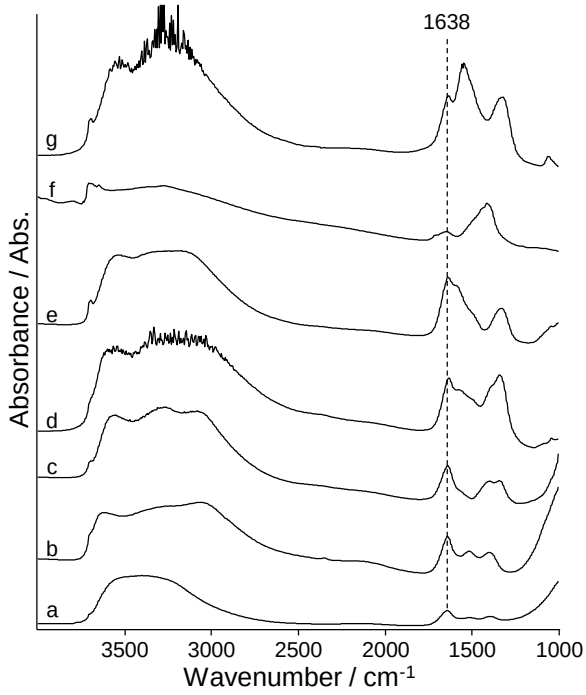

Figure B.7 IR spectra of the wetted metal oxides at RTP. γ-Al_2O_3 (a), basic γ-Al_2O_3 (b), TiO_2 (c), ZrO_2 (d), Alfa ZrO_2 (e), MgO (f), CeO_2 (g).

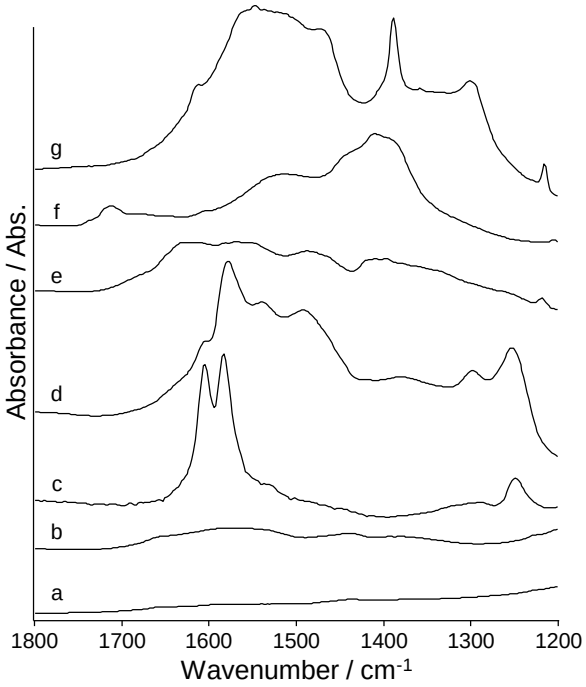

Figure B.8 Adsorbed carbonate region of the IR spectra of the wetted metal oxides after one hour spent under HV. γ-Al_2O_3 (a), basic γ-Al_2O_3 (b), TiO_2 (c), ZrO_2 (d), Alfa ZrO_2 (e), MgO (f), CeO_2 (g).

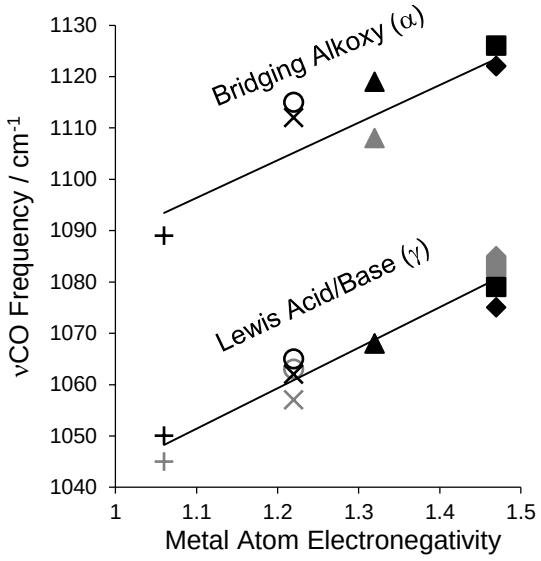

Figure B.9 Shift in electron density due to increased electronegativity of metal atom to which glycerol is bound. Arrows indicate direction of shifts in electron density. The white spheres indicate hydrogen atoms, the light grey spheres indicate oxygen atoms, the dark grey spheres indicate CUS surface metal atoms of a metal oxide, and the black spheres indicate carbon atoms.

APPENDIX C

SUPPLEMENTARY INFORMATION FOR CHAPTER 4

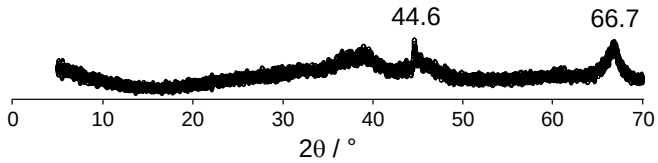

Figure C.1 XRD diffractogram of the 5 wt% Pt/g-Al_2O_3 catalyst used in the current study.

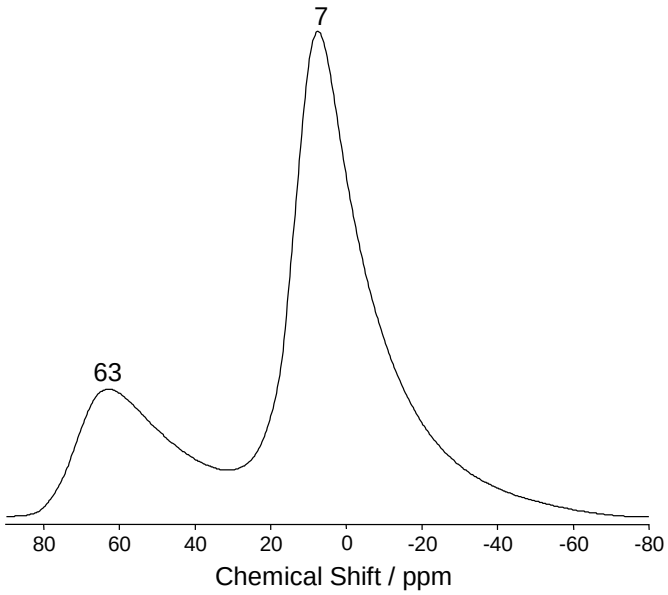

Figure C.2 ^{27}Al MAS-NMR Spectrum of the 5 wt% Pt/g-Al_2O_3 catalyst used in the current study.

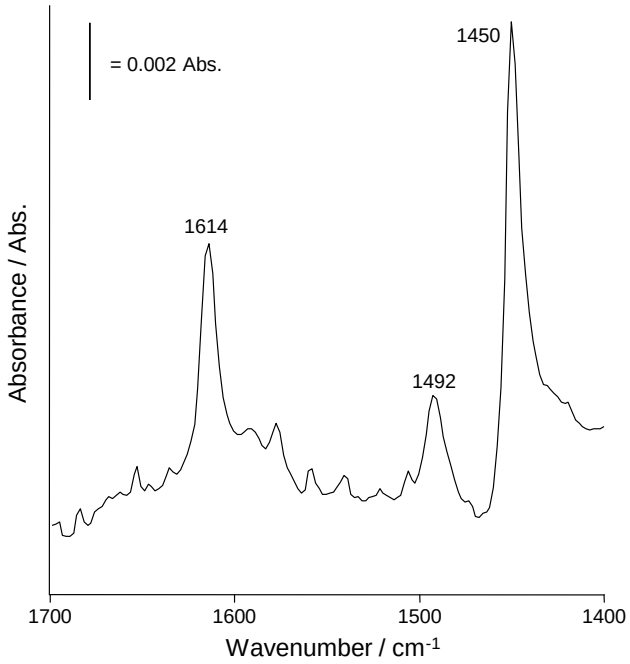

Figure C.3 Transmission FT-IR of the catalyst after activation, exposure to 0.110 mbar pyridine for 30 min, and subsequent high vacuum exposure for 30 min.

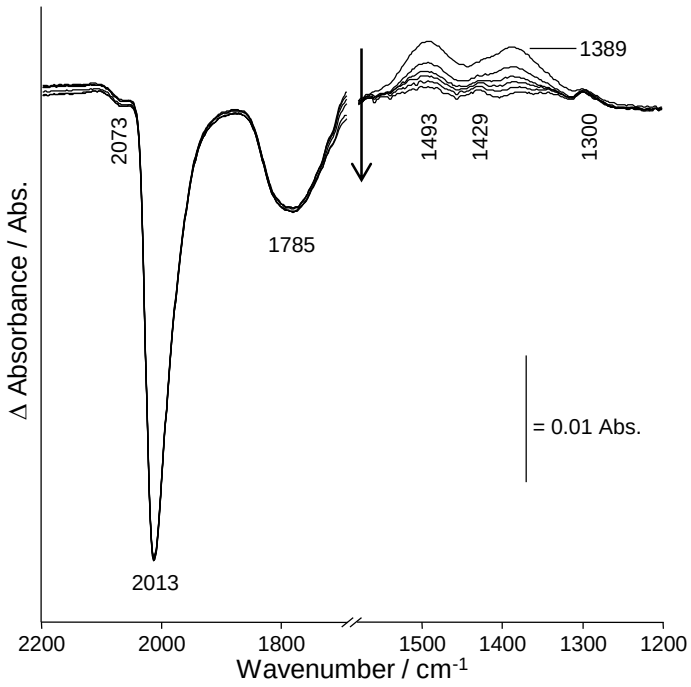

Figure C.4 Difference spectra of the catalyst layer collected every 5 min during the $O_2(H_2O)$ flow period, black arrow indicates direction of increasing time. The subtrahend spectrum was the spectrum collected just prior to the the $O_2(H_2O)$ flow period so that changes upon the admission of oxygen can be clearly observed.

As shown in the first difference spectrum of Figure C.4, within 5 min, all of the Pt bound CO species were completely removed, as evidenced by the negative peaks at 2073, 2013, and 1785 cm^{-1}. These species were oxidized to CO_2, which in the presence of H_2O rapidly convert to a carbonate species. The modes of this carbonate species are also evident in the first spectrum of Figure C.4. Namely, the $\nu_{asym}CO_2^-$ mode is evident at 1493 cm^{-1}, and the $\nu_{sym}CO_2^-$ gives rise to the peaks at 1429, 1389 cm^{-1}. Over the 30 min long $O_2(H_2O)$ flow period, these carbonate species were removed by the flowing H_2O as evidenced by their continuously decreasing absorbance.

REFERENCES

(1) Annual Energy Review 2011. In DOE/EIA, Ed. U.S. Government Printing Office: Washington, DC, 2012.

(2) Sieminski, A. *International Energy Outlook 2013*; Washington, DC, July 25, 2013, 2013.

(3) Meng, Q. Y.; Bentley, R. W., Global Oil Peaking: Responding to the Case for 'Abundant Supplies of Oil'. *Energy* **2008,** *33*, 1179-1184.

(4) Crowley, T. J., Causes of Climate Change Over the Past 1000 Years. *Science* **2000,** *289*, 270-277.

(5) Cox, P. M.; Betts, R. A.; Jones, C. D.; Spall, S. A.; Totterdell, I. J., Acceleration of Global Warming due to Carbon-Cycle Feedbacks in a Coupled Climate Model. *Nature* **2000,** *408*, 184-187.

(6) Hughes, T. P.; Baird, A. H.; Bellwood, D. R.; Card, M.; Connolly, S. R.; Folke, C.; Grosberg, R.; Hoegh-Guldberg, O.; Jackson, J. B. C.; Kleypas, J.; Lough, J. M.; Marshall, P.; Nystrom, M.; Palumbi, S. R.; Pandolfi, J. M.; Rosen, B.; Roughgarden, J., Climate Change, Human Impacts, and the Resilience of Coral Reefs. *Science* **2003,** *301*, 929-933.

(7) Hoegh-Guldberg, O.; Mumby, P. J.; Hooten, A. J.; Steneck, R. S.; Greenfield, P.; Gomez, E.; Harvell, C. D.; Sale, P. F.; Edwards, A. J.; Caldeira, K.; Knowlton, N.; Eakin, C. M.; Iglesias-Prieto, R.; Muthiga, N.; Bradbury, R. H.; Dubi, A.; Hatziolos, M. E., Coral Reefs Under Rapid Climate Change and Ocean Acidification. *Science* **2007,** *318*, 1737-1742.

(8) Schobert, H., Chemistry of Fossil Fuels and Biofuels. In Cambridge University Press: West Nyack, NY, USA, 2012; p 502.

(9) Kleinert, M.; Barth, T., Towards a Lignincellulosic Biorefinery: Direct One-Step Conversion of Lignin to Hydrogen-Enriched Biofuel. *Energy Fuels* **2008,** *22*, 1371-1379.

(10) Marshall, A. G.; Rodgers, R. P., Petroleomics: The Next Grand Challenge for Chemical Analysis. *Accounts Chem. Res.* **2004,** *37*, 53-59.

(11) OSHA Technical Manual, Section IV, Chapter 2, Petroleum Refining Processes. In 1 ed.; DOL, Ed. 1999.

(12) Huber, G. W.; Iborra, S.; Corma, A., Synthesis of Transportation Fuels from Biomass: Chemistry, Catalysts, and Engineering. *Chem. Rev.* **2006,** *106*, 4044-4098.

(13) Hill, J.; Nelson, E.; Tilman, D.; Polasky, S.; Tiffany, D., Environmental, Economic, and Energetic Costs and Benefits of Biodiesel and Ethanol Biofuels. *Proceedings of the National Academy of Sciences of the United States of America* **2006,** *103*, 11206-11210.

(14) Meher, L. C.; Sagar, D. V.; Naik, S. N., Technical Aspects of Biodiesel Production by Transesterification - a Review. *Renew. Sust. Energ. Rev.* **2006,** *10*, 248-268.

(15) Corma, A.; Iborra, S.; Velty, A., Chemical Routes for the Transformation of Biomass into Chemicals. *Chem. Rev.* **2007,** *107*, 2411-2502.

(16) Ragauskas, A. J.; Williams, C. K.; Davison, B. H.; Britovsek, G.; Cairney, J.; Eckert, C. A.; Frederick, W. J.; Hallett, J. P.; Leak, D. J.; Liotta, C. L.; Mielenz, J. R.; Murphy, R.; Templer, R.; Tschaplinski, T., The Path Forward for Biofuels and Biomaterials. *Science* **2006,** *311*, 484-489.

(17) Chheda, J. N.; Huber, G. W.; Dumesic, J. A., Liquid-Phase Catalytic Processing of Biomass-Derived Oxygenated Hydrocarbons to Fuels and Chemicals. *Angew. Chem. Int. Edit.* **2007,** *46*, 7164-7183.

(18) Davda, R. R.; Shabaker, J. W.; Huber, G. W.; Cortright, R. D.; Dumesic, J. A., A Review of Catalytic Issues and Process Conditions for Renewable Hydrogen and Alkanes by Aqueous-Phase Reforming of Oxygenated Hydrocarbons Over Supported Metal Catalysts. *Appl. Catal. B-Environ.* **2005,** *56*, 171-186.

(19) Sun, Y.; Cheng, J. Y., Hydrolysis of Lignocellulosic Materials for Ethanol Production: a Review. *Bioresour. Technol.* **2002,** *83*, 1-11.

(20) Perry's Chemical Engineer's Handbook. In 8 ed.; Green, D. W.; Perry, R. H., Eds. McGraw-Hill: New York, 2008.

(21) Corma, A.; Huber, G. W.; Sauvanaud, L.; O'Connor, P., Processing Biomass-Derived Oxygenates in the Oil Refinery: Catalytic Cracking (FCC) Reaction Pathways and Role of Catalyst. *J. Catal.* **2007,** *247*, 307-327.

(22) Gallezot, P., Conversion of Biomass to Selected Chemical Products. *Chem. Soc. Rev.* **2012,** *41*, 1538-1558.

(23) Bobleter, O., Hydrothermal Degradation and Fractionation of Saccharides and Polysaccharides. In *Polysaccharides Structural Diversity and Functional Versatility*, 2 ed.; Dumitriu, S., Ed. Macel Dekker: New York, NY, 2005; pp 893-936.

(24) Watanabe, M.; Aizawa, Y.; Iida, T.; Aida, T. M.; Levy, C.; Sue, K.; Inomata, H., Glucose Reactions with Acid and Base Catalysts in Hot Compressed Water at 473 K. *Carbohyd. Res.* **2005,** *340*, 1925-1930.

(25) Qi, X. H.; Watanabe, M.; Aida, T. M.; Smith, R. L., Catalytical Conversion of Fructose and Glucose into 5-Hydroxymethylfurfural in Hot Compressed Water by Microwave Heating. *Catal. Commun.* **2008,** *9*, 2244-2249.

(26) Cortright, R. D.; Davda, R. R.; Dumesic, J. A., Hydrogen from Catalytic Reforming of Biomass-Derived Hydrocarbons in Liquid Water. *Nature* **2002,** *418*, 964-967.

(27) Huber, G. W.; Chheda, J. N.; Barrett, C. J.; Dumesic, J. A., Production of Liquid Alkanes by Aqueous-Phase Processing of Biomass-Derived Carbohydrates. *Science* **2005,** *308*, 1446-1450.

(28) Marcilly, C., Present Status and Future Trends in Catalysis for Refining and Petrochemicals. *J. Catal.* **2003,** *216*, 47-62.

(29) Jongerius, A. L.; Copeland, J. R.; Foo, G. S.; Hofmann, J. P.; Bruijnincx, P. C. A.; Sievers, C.; Weckhuysen, B. M., Stability of Pt/γ-Al_2O_3 Catalysts in Lignin and Lignin Model Compound Solutions under Liquid Phase Reforming Reaction Conditions. *ACS Catal.* **2013,** *3*, 464-473.

(30) Ravenelle, R. M.; Copeland, J. R.; Kim, W. G.; Crittenden, J. C.; Sievers, C., Structural Changes of γ-Al_2O_3-Supported Catalysts in Hot Liquid Water. *ACS Catal.* **2011,** *1*, 552-561.

(31) Ravenelle, R. M.; Copeland, J. R.; Van Pelt, A. H.; Crittenden, J. C.; Sievers, C., Stability of Pt/γ-Al_2O_3 Catalysts in Model Biomass Solutions. *Top. Catal.* **2012,** *55*, 162-174.

(32) Mallon, E. E.; Bhan, A.; Tsapatsis, M., Driving Forces for Adsorption of Polyols onto Zeolites from Aqueous Solutions. *J. Phys. Chem. B* **2010,** *114*, 1939-1945.

(33) Mallon, E. E.; Babineau, I. J.; Kranz, J. I.; Guefrachi, Y.; Siepmann, J. I.; Bhan, A.; Tsapatsis, M., Correlations for Adsorption of Oxygenates onto Zeolites from Aqueous Solutions. *J. Phys. Chem. B* **2011,** *115*, 11431-11438.

(34) van Bronswijk, W.; Watling, H. R.; Yu, Z., A Study of the Adsorption of Acyclic Polyols on Hydrated Alumina. *Colloid Surf. A-Physicochem. Eng. Asp.* **1999,** *157*, 85-94.

(35) Sato, S.; Sato, F.; Gotoh, H.; Yamada, Y., Selective Dehydration of Alkanediols into Unsaturated Alcohols over Rare Earth Oxide Catalysts. *ACS Catal.* **2013,** *3*, 721-734.

(36) Calatayud, M., Ethylene Glycol Interaction on Alkaline Earth Oxides: A Periodic DFT Study. *Catal. Today* **2010,** *152*, 88-92.

(37) Popov, A.; Kondratieva, E.; Goupil, J. M.; Mariey, L.; Bazin, P.; Gilson, J. P.; Travert, A.; Mauge, F., Bio-oils Hydrodeoxygenation: Adsorption of Phenolic Molecules on Oxidic Catalyst Supports. *J. Phys. Chem. C* **2010,** *114*, 15661-15670.

(38) Wawrzetz, A.; Peng, B.; Hrabar, A.; Jentys, A.; Lemonidou, A. A.; Lercher, J. A., Towards Understanding the Bifunctional Hydrodeoxygenation and Aqueous Phase Reforming of Glycerol. *J. Catal.* **2010,** *269*, 411-420.

(39) He, R.; Davda, R. R.; Dumesic, J. A., In Situ ATR-IR Spectroscopic and Reaction Kinetics Studies of Water-Gas Shift and Methanol Reforming on Pt/Al_2O_3 Catalysts in Vapor and Liquid Phases. *J. Phys. Chem. B* **2005,** *109*, 2810-2820.

(40) Ebbesen, S. D.; Mojet, B. L.; Lefferts, L., CO Adsorption and Oxidation at the Catalyst-Water Interface: An Investigation by Attenuated Total Reflection Infrared Spectroscopy. *Langmuir* **2006,** *22*, 1079-1085.

(41) Ebbesen, S. D.; Mojet, B. L.; Lefferts, L., In situ ATR-IR Study of CO Adsorption and Oxidation Over Pt/Al_2O_3 in Gas and Aqueous Phase: Promotion Effects by Water and pH. *J. Catal.* **2007,** *246*, 66-73.

(42) Ortiz-Hernandez, I.; Owens, D. J.; Strunk, M. R.; Williams, C. T., Multivariate Analysis of ATR-IR Spectroscopic Data: Applications to the Solid-Liquid Catalytic Interface. *Langmuir* **2006,** *22*, 2629-2639.

(43) Johnson, D. T.; Taconi, K. A., The Glycerin Glut: Options for the Value-Added Conversion of Crude Glycerol Resulting from Biodiesel Production. *Environ. Prog.* **2007,** *26*, 338-348.

(44) Werpy, T.; Petersen, G.; Aden, A.; Bozell, J.; Holladay, J.; White, J.; Manheim, A., Top Value Added Chemicals From Biomass: Volume 1—Results of Screening for Potential Candidates from Sugars and Synthesis Gas. In DOE, Ed. Golden, 2004; Vol. 1, pp 1-76.

(45) Holladay, J. E.; Bozell, J. J.; White, J. F.; Johnson, D., Top Value-Added Chemicals from Biomass Volume II - Results of Screening for Potential Candidates from Biorefinery Lignin. In DOE, Ed. 2007; Vol. 2, pp 1-87.

(46) Fukuoka, A.; Dhepe, P. L., Catalytic Conversion of Cellulose into Sugar Alcohols. *Angew. Chem. Int. Edit.* **2006,** *45*, 5161-5163.

(47) Shabaker, J. W.; Davda, R. R.; Huber, G. W.; Cortright, R. D.; Dumesic, J. A., Aqueous-Phase Reforming of Methanol and Ethylene Glycol over Alumina-Supported Platinum Catalysts. *J. Catal.* **2003,** *215*, 344-352.

(48) Copeland, J. R.; Foo, G. S.; Harrison, L. A.; Sievers, C., In situ ATR-IR Study on Aqueous Phase Reforming Reactions of Glycerol Over a $Pt/\gamma\text{-}Al_2O_3$ Catalyst. *Catal. Today* **2013,** *205*, 49-59.

(49) Griffin, M. B.; Jorgensen, E. L.; Medlin, J. W., The Adsorption and Reaction of Ethylene Glycol and 1,2-Propanediol on Pd(111): A TPD and HREELS Study. *Surf. Sci.* **2010,** *604*, 1558-1564.

(50) Datka, J.; Turek, A. M.; Jehng, J. M.; Wachs, I. E., Acidic Properties of Supported Niobium Oxide Catalysts - an Infrared-Spectroscopy Investigation. *J. Catal.* **1992,** *135*, 186-199.

(51) Emeis, C. A., Determination of Integrated Molar Extinction Coefficients for Infrared Absorption Bands of Pyridine Adsorbed on Solid Acid Catalysts. *J. Catal.* **1993,** *141*, 347-354.

(52) Domok, M.; Toth, M.; Rasko, J.; Erdohelyi, A., Adsorption and Reactions of Ethanol and Ethanol-Water Mixture on Alumina-Supported Pt Catalysts. *Appl. Catal. B-Environ.* **2007,** *69*, 262-272.

(53) Matyshak, V. A.; Sil'chenkova, O. N.; Ismailov, I. T.; Tret'yakov, V. F., Mechanism of Methanol Conversion on ZrO_2 and 5% Cu/ZrO_2 According to In Situ IR Spectroscopic Data. *Kinet. Catal.* **2010,** *51*, 428-437.

(54) Peluso, M. A.; Pronsato, E.; Sambeth, J. E.; Thomas, H. J.; Busca, G., Catalytic Combustion of Ethanol on Pure and Alumina Supported K-Mn Oxides: An IR and Flow Reactor Study. *Appl. Catal. B-Environ.* **2008,** *78*, 73-79.

(55) Schenkel, R.; Jentys, A.; Parker, S. F.; Lercher, J. A., INS and IR and NMR Spectroscopic Study of C-1-C-4 Alcohols Adsorbed on Alkali Metal-Exchanged Zeolite X. *J. Phys. Chem. B* **2004,** *108*, 15013-15026.

(56) Zaki, M. I.; Hasan, M. A.; Pasupulety, L., In situ FTIR Spectroscopic Study of 2-Propanol Adsorptive and Catalytic Interactions on Metal-Modified Aluminas. *Langmuir* **2001,** *17*, 4025-4034.

(57) Yan, W.; Suppes, G. J., Vapor Pressures and Evaporation Studies of Sugars and Sugar Alcohols. *J. Chem. Eng. Data* **2008,** *53*, 2033-2040.

(58) Burcham, L. J.; Wachs, I. E., The Origin of the Support Effect in Supported Metal Oxide Catalysts: in situ Infrared and Kinetic Studies During Methanol Oxidation. *Catal. Today* **1999,** *49*, 467-484.

(59) Wang, J.; Huang, L. M.; Chen, H. Y.; Li, Q. Z., Acid Function of Al-MCM-41 Supported Platinum Catalysts in Hydrogenation of Benzene, Toluene and O-Xylene. *Catal. Lett.* **1998,** *55*, 157-163.

(60) Brunauer, S.; Emmett, P. H.; Teller, E., Adsorption of Gases in Multimolecular Layers. *J. Am. Chem. Soc.* **1938,** *60*, 309-319.

(61) Barrett, E. P.; Joyner, L. G.; Halenda, P. P., The Determination of Pore Volume and Area Distributions in Porous Substances.1. Computations from Nitrogen Isotherms. *J. Am. Chem. Soc.* **1951,** *73*, 373-380.

(62) Selli, E.; Forni, L., Comparison Between the Surface Acidity of Solid Catalysts Determined by TPD and FTIR Analysis of Pre-Adsorbed Pyridine. *Micropor. Mesopor. Mat.* **1999,** *31*, 129-140.

(63) Zaki, M. I.; Hasan, M. A.; Al-Sagheer, F. A.; Pasupulety, L., In Situ FTIR Spectra of Pyridine Adsorbed on SiO_2-Al_2O_3, TiO_2, ZrO_2 and CeO_2: General Considerations for the Identification of Acid Sites on Surfaces of Finely Divided Metal Oxides. *Colloid Surf. A-Physicochem. Eng. Asp.* **2001,** *190*, 261-274.

(64) Sholl, D. S.; Steckel, J. A., Density functional theory: a practical introduction *John Wiley & Sons, Inc.: Hoboken, NJ* **2009**.

(65) Perdew, J. P.; Burke, K.; Ernzerhof, M., Generalized Gradient Approximation Made Simple. *Phys. Rev. Lett.* **1996,** *77*, 3865-3868.

(66) Kresse, G.; Hafner, J., Ab initio molecular dynamics for liquid metals. *Phys. Rev. B* **1993,** *47*, 558-561.

(67) Kresse, G.; Furthmüller, J., Efficiency of ab-initio total energy calculations for metals and semiconductors using a plane-wave basis set. *Comput. Mater. Sci.* **1996,** *6*, 15-50.

(68) Kresse, G.; Furthmüller, J., Efficient iterative schemes for ab initio total-energy calculations using a plane-wave basis set. *Phys. Rev. B* **1996,** *54*, 11169-11186.

(69) Kresse, G.; Joubert, D., From ultrasoft pseudopotentials to the projector augmented-wave method. *Phys. Rev. B* **1999,** *59*, 1758-1775.

(70) Grimme, S., Semiempirical GGA-type density functional constructed with a long-range dispersion correction. *J. Comput. Chem.* **2006,** *27*, 1787-1799.

(71) Shi, X.-R.; Sholl, D. S., Nucleation of Rhn (n = 1–5) Clusters on γ-Al2O3 Surfaces: A Density Functional Theory Study. *J. Phys. Chem. C* **2012,** *116*, 10623-10631.

(72) Digne, M.; Sautet, P.; Raybaud, P.; Euzen, P.; Toulhoat, H., Use of DFT to Achieve a Rational Understanding of Acid-Basic Properties of γ-Alumina Surfaces. *J. Catal.* **2004,** *226*, 54-68.

(73) Wefers, K.; Misra, C., *Oxides and Hydroxides of Aluminum*. 2 ed.; Alcoa Research Laboratories: 1987; p 92.

(74) Ravenelle, R. M.; Diallo, F. Z.; Crittenden, J. C.; Sievers, C., Effects of Metal Precursors on the Stability and Observed Reactivity of Pt/γ-Al_2O_3 Catalysts in Aqueous Phase Reactions. *ChemCatChem* **2012,** *4*, 492-494.

(75) Taguchi, A.; Schüth, F., Ordered Mesoporous Materials in Catalysis. *Micropor. Mesopor. Mat.* **2005,** *77*, 1-45.

(76) Spiess, H. W., Deuteron NMR - A New Tool for Studying Chain Mobility and Orientation in Polymers. *Adv. Polym. Sci.* **1985,** *66*, 23-58.

(77) Pinchas, S.; Laulicht, I., *Infrared Spectra of Labelled Compounds*. Academic Press Inc.: New York, New York 10003, 1971.

(78) Ayre, C. R.; Madix, R. J., The Adsorption and Reaction of 1,2-Propanediol on Ag(110) Under Oxygen Lean Conditions. *Surf. Sci.* **1994,** *303*, 279-296.

(79) Colthup, N. B.; Daly, L. H.; Wiberley, S. E., *Introduction to Infrared and Raman Spectroscopy*. Academic Press: 1990; p 547.

(80) Singh, J.; Alayon, E. M. C.; Tromp, M.; Safonova, O. V.; Glatzel, P.; Nachtegaal, M.; Frahm, R.; van Bokhoven, J. A., Generating Highly Active Partially Oxidized Platinum during Oxidation of Carbon Monoxide over Pt/Al_2O_3: In Situ, Time-Resolved, and High-Energy-Resolution X-Ray Absorption Spectroscopy. *Angew. Chem. Int. Edit.* **2008,** *47*, 9260-9264.

(81) Weber, D.; Mitchell, J.; McGregor, J.; Gladden, L. F., Comparing Strengths of Surface Interactions for Reactants and Solvents in Porous Catalysts Using Two-Dimensional NMR Relaxation Correlations. *J. Phys. Chem. C* **2009,** *113*, 6610-6615.

(82) Olson, D. H.; Kokotailo, G. T.; Lawton, S. L.; Meier, W. M., Crystal-Structure and Structure-Related Properties of ZSM-5. *J. Phys. Chem.* **1981,** *85*, 2238-2243.

(83) Digne, M.; Sautet, P.; Raybaud, P.; Euzen, P.; Toulhoat, H., Hydroxyl Groups on γ-Alumina Surfaces: A DFT Study. *J. Catal.* **2002,** *211*, 1-5.

(84) Deo, A. V.; Dalla Lana, I. G., An Infrared Study of Adsorption and Mechanism of Surface Reactions of 1-Propanol on γ-Alumina and γ-Alumina Doped with Sodium Hydroxide and Chromium Oxide. *J. Phys. Chem.* **1969,** *73*, 716-723.

(85) Matyshak, V. A.; Berezina, L. A.; Sil'chenkova, O. N.; Tret'yakov, V. F.; Lin, G. I.; Rozovskii, A. Y., Properties of Surface Compounds in Methanol Conversion on γ-Al_2O_3: Data of in situ IR Spectroscopy. *Kinet. Catal.* **2009,** *50*, 111-121.

(86) Thanthiriwatte, K. S.; Hohenstein, E. G.; Burns, L. A.; Sherrill, C. D., Assessment of the Performance of DFT and DFT-D Methods for Describing Distance Dependence of Hydrogen-Bonded Interactions. *J. Chem. Theory. Comput.* **2011,** *7*, 88-96.

(87) Liu, D. F.; Ma, G.; Xu, M.; Allen, H. C., Adsorption of Ethylene Glycol Vapor on α-Al_2O_3(0001) and Amorphous SiO_2 Surfaces: Observation of Molecular Orientation and Surface Hydroxyl Groups as Sorption Sites. *Environ. Sci. Technol.* **2005,** *39*, 206-212.

(88) Haffad, D.; Chambellan, A.; Lavalley, J. C., Propan-2-ol Transformation on Simple Metal Oxides TiO_2, ZrO_2 and CeO_2. *J. Mol. Catal. A-Chem.* **2001,** *168*, 153-164.

(89) Wischert, R.; Coperet, C.; Delbecq, F.; Sautet, P., Optimal Water Coverage on Alumina: A Key to Generate Lewis Acid-Base Pairs that are Reactive Towards the C-H Bond Activation of Methane. *Angewandte Chemie-International Edition* **2011,** *50*, 3202-3205.

(90) Knözinger, H.; Ratnasamy, P., Catalytic Aluminas - Surface Models and Characterization of Surface Sites. *Catal. Rev.-Sci. Eng.* **1978,** *17*, 31-70.

(91) Ketchie, W. C.; Maris, E. P.; Davis, R. J., In-Situ X-Ray Absorption Spectroscopy of Supported Ru Catalysts in the Aqueous Phase. *Chem. Mat.* **2007,** *19*, 3406-3411.

(92) Iriondo, A.; Cambra, J. F.; Barrio, V. L.; Guemez, M. B.; Arias, P. L.; Sanchez-Sanchez, M. C.; Navarro, R. M.; Fierro, J. L. G., Glycerol Liquid Phase Conversion over Monometallic and Bimetallic Catalysts: Effect of Metal, Support Type and Reaction Temperatures. *Appl. Catal. B-Environ.* **2011,** *106*, 83-93.

(93) Bermudez, V. M., Investigation of the Interaction of γ-Al_2O_3 with Aqueous Solutions of Dimethyl Methylphosphonate Using Infrared Multiple Internal Reflection Spectroscopy. *Langmuir* **2013,** *29*, 1483-1489.

(94) Martucci, A.; Pasti, L.; Marchetti, N.; Cavazzini, A.; Dondi, F.; Alberti, A., Adsorption of Pharmaceuticals from Aqueous Solutions on Synthetic Zeolites. *Micropor. Mesopor. Mat.* **2012,** *148*, 174-183.

(95) Lupulescu, A. I.; Kumar, M.; Rimer, J. D., A Facile Strategy To Design Zeolite L Crystals with Tunable Morphology and Surface Architecture. *J. Am. Chem. Soc.* **2013,** *135*, 6608-6617.

(96) Bai, P.; Tsapatsis, M.; Siepmann, J. I., Multicomponent Adsorption of Alcohols onto Silicalite-1 from Aqueous Solution: Isotherms, Structural Analysis, and Assessment of Ideal Adsorbed Solution Theory. *Langmuir* **2012,** *28*, 15566-15576.

(97) Xiong, R.; Sandler, S. I.; Vlachos, D. G., Molecular Screening of Alcohol and Polyol Adsorption onto MFI-Type Zeolites. *Langmuir* **2012,** *28*, 4491-4499.

(98) Xiong, R. C.; Sandler, S. I.; Vlachos, D. G., Alcohol Adsorption onto Silicalite from Aqueous Solution. *J. Phys. Chem. C* **2011,** *115*, 18659-18669.

(99) Wischert, R.; Laurent, P.; Coperet, C.; Delbecq, F.; Sautet, P., γ-Alumina: The Essential and Unexpected Role of Water for the Structure, Stability, and Reactivity of "Defect" Sites. *J. Am. Chem. Soc.* **2012,** *134*, 14430-14449.

(100) Copeland, J. R.; Shi, X. R.; Sholl, D. S.; Sievers, C., Surface Interactions of C-2 and C-3 Polyols with γ-Al_2O_3 and the Role of Coadsorbed Water. *Langmuir* **2013,** *29*, 581-593.

(101) Erdohelyi, A.; Rasko, J.; Kecskes, T.; Toth, M.; Domok, M.; Baan, K., Hydrogen Formation in Ethanol Reforming on Supported Noble Metal Catalysts. *Catal. Today* **2006,** *116*, 367-376.

(102) Mojet, B. L.; Ebbesen, S. D.; Lefferts, L., Light at the Interface: the Potential of Attenuated Total Reflection Infrared Spectroscopy for Understanding Heterogeneous Catalysis in Water. *Chem. Soc. Rev.* **2010,** *39*, 4643-4655.

(103) Mekhemer, G. A. H.; Halawy, S. A.; Mohamed, M. A.; Zaki, M. I., Qualitative and Quantitative Assessments of Acid and Base Sites Exposed on Polycrystalline MgO Surfaces: Thermogravimetric, Calorimetric, and in-situ FTIR Spectroscopic Study Combination. *J. Phys. Chem. B* **2004,** *108*, 13379-13386.

(104) Chaikittisilp, W.; Kim, H. J.; Jones, C. W., Mesoporous Alumina-Supported Amines as Potential Steam-Stable Adsorbents for Capturing CO_2 from Simulated Flue Gas and Ambient Air. *Energy Fuels* **2011,** *25*, 5528-5537.

(105) Bali, S.; Chen, T. T.; Chaikittisilp, W.; Jones, C. W., Oxidative Stability of Amino Polymer-Alumina Hybrid Adsorbents for Carbon Dioxide Capture. *Energy Fuels* **2013,** *27*, 1547-1554.

(106) Tamura, M.; Shimizu, K.; Satsuma, A., Comprehensive IR Study on Acid/Base Properties of Metal Oxides. *Appl. Catal. A-Gen.* **2012,** *433*, 135-145.

(107) Birks, L. S.; Brooks, E. J., Hafnium-Zirconium and Tantalum-Columbium Systems - Quantitative Analysis by X-ray Flourescence. *Anal. Chem.* **1950,** *22*, 1017-1020.

(108) Di Cosimo, J. I.; Diez, V. K.; Xu, M.; Iglesia, E.; Apesteguia, C. R., Structure and Surface and Catalytic Properties of Mg-Al Basic Oxides. *J. Catal.* **1998,** *178*, 499-510.

(109) Doskocil, E. J.; Davis, R. J., Spectroscopic Characterization and Catalytic Activity of Zeolite X Containing Occluded Alkali Species. *J. Catal.* **1999,** *188*, 353-364.

(110) Lercher, J. A.; Colombier, C.; Noller, H., Acid-Base Properties of Alumina Magnesia Mixed Oxides. 4. Infrared Study of Adsorption of Carbon-Dioxide. *J. Chem. Soc., Faraday Trans. 1* **1984,** *80*, 949-959.

(111) Bredow, T.; Jug, K., Theoretical Investigation of Water-Adsorption at Rutile and Anatase Surfaces. *Surf. Sci.* **1995,** *327*, 398-408.

(112) Chizallet, C.; Digne, M.; Arrouvel, C.; Raybaud, P.; Delbecq, F.; Costentin, G.; Che, M.; Sautet, P.; Toulhoat, H., Insights into the Geometry, Stability and Vibrational Properties of OH Groups on γ-Al_2O_3, TiO_2-Anatase and MgO from DFT Calculations. *Top. Catal.* **2009,** *52*, 1005-1016.

(113) Echterhoff, R.; Knözinger, E., FT-IR Characterization of Adsorption Complexes on Magnesium-Oxide Surfaces. *J. Mol. Struct.* **1988,** *174*, 343-350.

(114) Molinari, M.; Parker, S. C.; Sayle, D. C.; Islam, M. S., Water Adsorption and Its Effect on the Stability of Low Index Stoichiometric and Reduced Surfaces of Ceria. *J. Phys. Chem. C* **2012,** *116*, 7073-7082.

(115) Nawrocki, J.; Rigney, M. P.; McCormick, A.; Carr, P. W., Chemistry of Zirconia and its Use in Chromatography. *J. Chromatogr. A* **1993,** *657*, 229-282.

(116) Fouad, N. E.; Thomasson, P.; Knozinger, H., IR Study of Adsorption and Reaction of Methylbutynol on the Surface of Pure and Modified MgO Catalysts: Probing the Catalyst Surface Basicity. *Appl. Catal. A-Gen.* **2000,** *194*, 213-225.

(117) Knozinger, E.; Jacob, K. H.; Singh, S.; Hofmann, P., Hydroxyl-Groups as IR Active Surface Probes on MgO Crystallites. *Surf. Sci.* **1993,** *290*, 388-402.

(118) Kataoka, Y.; Kitadai, N.; Hisatomi, O.; Nakashima, S., Nature of Hydrogen Bonding of Water Molecules in Aqueous Solutions of Glycerol by Attenuated Total Reflection (ATR) Infrared Spectroscopy. *Appl. Spectrosc.* **2011,** *65*, 436-441.

(119) Morrow, B. A.; Thomson, L. W.; Wetmore, R. W., C-H Stretching Bands of Methanol Adsorbed on Silica. *J. Catal.* **1973,** *28*, 332-334.

(120) Takezawa, N.; Kobayash.H, Shift of CH Stretching Band of Surface Alcoholate on Metal Oxides. *J. Catal.* **1972,** *25*, 179-&.

(121) Takezawa, N.; Kobayash.H, CH Stretching Bands of Surface Alcoholates Formed on Metal Oxides - A Reply to Morrow, Thomson and Wetmore. *J. Catal.* **1973,** *28*, 335-336.

(122) Rep, M.; Palomares, A. E.; Eder-Mirth, G.; van Ommen, J. G.; Rosch, N.; Lercher, J. A., Interaction of Methanol with Alkali Metal Exchanged Molecular Sieves. I. IR Spectroscopy Study. *J. Phys. Chem. B* **2000,** *104*, 8624-8630.

(123) Kuwahara, Y.; Kang, D. Y.; Copeland, J. R.; Bollini, P.; Sievers, C.; Kamegawa, T.; Yamashita, H.; Jones, C. W., Enhanced CO_2 Adsorption over Polymeric Amines Supported on Heteroatom-Incorporated SBA-15 Silica: Impact of Heteroatom Type and

Loading on Sorbent Structure and Adsorption Performance. *Chem.-Eur. J.* **2012,** *18*, 16649-16664.

(124) Kuwahara, Y.; Kang, D. Y.; Copeland, J. R.; Brunelli, N. A.; Didas, S. A.; Bollini, P.; Sievers, C.; Kamegawa, T.; Yamashita, H.; Jones, C. W., Dramatic Enhancement of CO_2 Uptake by Poly(ethyleneimine) Using Zirconosilicate Supports. *J. Am. Chem. Soc.* **2012,** *134*, 10757-10760.

(125) Lonyi, F.; Valyon, J.; Engelhardt, J.; Mizukami, F., Characterization and Catalytic Properties of Sulfated ZrO_2-TiO_2 Mixed Oxides. *J. Catal.* **1996,** *160*, 279-289.

(126) Lefevre, G.; Duc, M.; Lepeut, P.; Caplain, R.; Fedoroff, M., Hydration of γ-Alumina in Water and its Effects on Surface Reactivity. *Langmuir* **2002,** *18*, 7530-7537.

(127) Branda, M. M.; Ferullo, R. M.; Belelli, P. G.; Castellani, N. J., Methanol Adsorption on Magnesium Oxide Surface with Defects: a DFT Study. *Surf. Sci.* **2003,** *527*, 89-99.

(128) Peng, X. D.; Barteau, M. A., Acid-Base Properties of Model MgO Surfaces. *Langmuir* **1991,** *7*, 1426-1431.

(129) Binet, C.; Daturi, M.; Lavalley, J. C., IR Study of Polycrystalline Ceria Properties in Oxidised and Reduced States. *Catal. Today* **1999,** *50*, 207-225.

(130) Chen, T. L.; Mullins, D. R., Ethylene Glycol Adsorption and Reaction over CeO_x(111) Thin Films. *J. Phys. Chem. C* **2011,** *115*, 13725-13733.

(131) Ketchie, W. C.; Murayama, M.; Davis, R. J., Promotional Effect of Hydroxyl on the Aqueous Phase Oxidation of Carbon Monoxide and Glycerol over Supported Au Catalysts. *Top. Catal.* **2007,** *44*, 307-317.

(132) Bennett, R. V.; Cleaves, H. J.; Davis, J. M.; Sokolov, D. A.; Orlando, T. M.; Bada, J. L.; Fernandez, F. M., Desorption Electrospray Ionization Imaging Mass Spectrometry as a Tool for Investigating Model Prebiotic Reactions on Mineral Surfaces. *Anal. Chem.* **2013,** *85*, 1276-1279.

(133) Chen, Y. F.; Chen, H. Y.; Aleksandrov, A.; Orlando, T. M., Roles of Water, Acidity, and Surface Morphology in Surface-Assisted Laser Desorption/Ionization of Amino Acids. *J. Phys. Chem. C* **2008,** *112*, 6953-6960.

(134) Nguyen, V. S.; Orlando, T. M.; Leszczynski, J.; Nguyen, M. T., Theoretical Study of the Decomposition of Formamide in the Presence of Water Molecules. *J. Phys. Chem. A* **2013,** *117*, 2543-2555.

(135) Scott, A. M.; Dawley, M. M.; Orlando, T. M.; Hill, F. C.; Leszczynski, J., Theoretical Study of the Roles of Na+ and Water on the Adsorption of Formamide on Kaolinite Surfaces. *J. Phys. Chem. C* **2012,** *116*, 23992-24005.

(136) Kandoi, S.; Greeley, J.; Simonetti, D.; Shabaker, J.; Dumesic, J. A.; Mavrikakis, M., Reaction Kinetics of Ethylene Glycol Reforming over Platinum in the Vapor versus Aqueous Phases. *J. Phys. Chem. C* **2010,** *115*, 961-971.

(137) Shabaker, J. W.; Huber, G. W.; Davda, R. R.; Cortright, R. D.; Dumesic, J. A., Aqueous-Phase Reforming of Ethylene Glycol over Supported Platinum Catalysts. *Catal. Lett.* **2003,** *88*, 1-8.

(138) Davda, R. R.; Shabaker, J. W.; Huber, G. W.; Cortright, R. D.; Dumesic, J. A., Aqueous-Phase Reforming of Ethylene Glycol on Silica-Supported Metal Catalysts. *Appl. Catal. B-Environ.* **2003,** *43*, 13-26.

(139) Davda, R. R.; Alcala, R.; Shabaker, J.; Huber, G.; Cortright, R. D.; Mavrikakis, M.; Dumesic, J. A., DFT and Experimental Studies of C-C and C-O Bond Cleavage in Ethanol and Ethylene Glycol on Pt Catalysts. In *Science and Technology in Catalysis 2002*, Anpo, M.; Onaka, M.; Yamashita, H., Eds. Kodansha Ltd: Tokyo, 2003; Vol. 145, pp 79-84.

(140) Greeley, J.; Mavrikakis, M., Competitive Paths for Methanol Decomposition on Pt(111). *J. Am. Chem. Soc.* **2004,** *126*, 3910-3919.

(141) Liu, B.; Greeley, J., Decomposition Pathways of Glycerol via C-H, O-H, and C-C Bond Scission on Pt(111): A Density Functional Theory Study. *J. Phys. Chem. C* **2011,** *115*, 19702-19709.

(142) Huber, G. W.; Shabaker, J. W.; Evans, S. T.; Dumesic, J. A., Aqueous-Phase Reforming of Ethylene Glycol over Supported Pt and Pd Bimetallic Catalysts. *Appl. Catal. B-Environ.* **2006,** *62*, 226-235.

(143) Morterra, C.; Emanuel, C.; Cerrato, G.; Magnacca, G., Infrared Study of Some Surface-Properties of Boehmite (γ-AlO_2H). *J. Chem. Soc., Faraday Trans.* **1992,** *88*, 339-348.

(144) Ortiz-Hernandez, I.; Williams, C. T., In Situ Investigation of Solid-Liquid Catalytic Interfaces by Attenuated Total Reflection Infrared Spectroscopy. *Langmuir* **2003,** *19*, 2956-2962.

(145) Holleman, A. F.; Wiberg, E., *Inorganic Chemistry*. 34 ed.; Academic Press: Berlin, 2001; p 1884.

(146) Trenary, M., Reflection Absorption Infrared Spectroscopy and the Structure of Molecular Adsorbates on Metal Surfaces. *Annu. Rev. Phys. Chem.* **2000,** *51*, 381-403.

(147) Ferri, D.; Burgi, T.; Baiker, A., Pt and Pt/Al_2O_3 Thin Films for Investigation of Catalytic Solid-Liquid Interfaces by ATR-IR Spectroscopy: CO Adsorption, H_2 Induced Reconstruction and Surface-Enhanced Absorption. *J. Phys. Chem. B* **2001,** *105*, 3187-3195.

(148) Teliska, M.; O'Grady, W. E.; Ramaker, D. E., Determination of H Adsorption Sites on Pt/C Electrodes in $HClO_4$ from Pt L-23 X-Ray Absorption Spectroscopy. *J. Phys. Chem. B* **2004,** *108*, 2333-2344.

(149) Conway, B. E.; Angerste, H.; Lalibert, L. H., Reflectance Changes During Formation and Reduction of Oxide-Films on Gold and Platinum - Correction for Double-Layer-Effects. *J. Electrochem. Soc.* **1974,** *121*, 1596-1603.

(150) Nichols, R. J.; Bewick, A., Spectroscopic Identification of the Adsorbed Intermediate in Hydrogen Evolution on Platinum. *J. Electroanal. Chem.* **1988,** *243*, 445-453.

(151) Liu, X. S.; Korotkikh, O.; Farrauto, R., Selective Catalytic Oxidation of CO in H_2: Structural Study of Fe Oxide-Promoted Pt/Alumina Catalyst. *Appl. Catal. A-Gen.* **2002,** *226*, 293-303.

(152) Xu, X.; Wu, D. Y.; Ren, B.; Xian, H.; Tian, Z. Q., On-Top Adsorption of Hydrogen at Platinum Electrodes: a Quantum-Chemical Study. *Chem. Phys. Lett.* **1999,** *311*, 193-201.

(153) Ogasawara, H.; Ito, M., Hydrogen Adsorption on Pt(100), Pt(110), Pt(111) and Pt(1111) Electrode Surface Studied by In-Situ Infrared Reflection-Absorption Spectroscopy. *Chem. Phys. Lett.* **1994,** *221*, 213-218.

(154) Kappers, M. J.; Vandermaas, J. H., Correlation Between CO Frequency and Pt Coordination-Number - A DRIFT Study on Supported Pt Catalysts. *Catal. Lett.* **1991,** *10*, 365-373.

(155) Kizhakevariam, N.; Jiang, X. D.; Weaver, M. J., Infrared-Spectroscopy of Model Electrochemical Interfaces in Ultrahigh-Vacuum - the Archetypical Case of Carbon-Monoxide Water Coadsorption on Pt(111). *J. Chem. Phys.* **1994,** *100*, 6750-6764.

(156) Chang, S. C.; Weaver, M. J., Insitu Infrared-Spectroscopy at Single-Crystal Metal-Electrodes - an Emerging Link Between Electrochemical and Ultrahigh-Vacuum Surface Science. *J. Phys. Chem.* **1991,** *95*, 5391-5400.

(157) Gland, J. L.; Sexton, B. A.; Fisher, G. B., Oxygen Interactions With the Pt(111) Surface. *Surf. Sci.* **1980,** *95*, 587-602.

(158) Morterra, C.; Magnacca, G., A Case Study: Surface Chemistry and Surface Structure of Catalytic Aluminas, as Studied by Vibrational Spectroscopy of Adsorbed Species. *Catal. Today* **1996,** *27*, 497-532.

(159) Derrouiche, S.; Bianchi, D., Experiments and Kinetic Model Regarding the Induction Period Observed During the Oxidation by O_2 of Adsorbed CO Species on Pt/Al_2O_3 Catalysts. *J. Catal.* **2005,** *230*, 359-374.

(160) Bourane, A.; Derrouiche, S.; Bianchi, D., Impact of Pt Dispersion on the Elementary Steps of CO Oxidation by O_2 over Pt/Al_2O_3 Catalysts. *J. Catal.* **2004,** *228*, 288-297.

(161) Hanawa, H.; Kunimatsu, K.; Uchida, H.; Watanabe, M., In Situ ATR-FTIR Study of Bulk CO Oxidation on a Polycrystalline Pt Electrode. *Electrochim. Acta* **2009,** *54*, 6276-6285.

(162) Kunimatsu, K.; Sato, T.; Uchida, H.; Watanabe, M., Role of Terrace/Step Edge Sites in CO Adsorption/Oxidation on a Polycrystalline Pt Electrode Studied by In Situ ATR-FTIR Method. *Electrochim. Acta* **2008,** *53*, 6104-6110.

(163) Sievers, C.; Onda, A.; Olindo, R.; Lercher, J. A., Adsorption and Polarization of Branched Alkanes on H-LaX. *J. Phys. Chem. C* **2007,** *111*, 5454-5464.

(164) Kazansky, V. B.; Pidko, E. A., Intensities of IR Stretching Bands as a Criterion of Polarization and Initial Chemical Activation of Adsorbed Molecules in Acid Catalysis. Ethane Adsorption and Dehydrogenation by Zinc Ions in ZnZSM-5 Zeolite. *J. Phys. Chem. B* **2005,** *109*, 2103-2108.

(165) Spendelow, J. S.; Goodpaster, J. D.; Kenis, P. J. A.; Wieckowski, A., Mechanism of CO Oxidation on Pt(111) in Alkaline Media. *J. Phys. Chem. B* **2006,** *110*, 9545-9555.

(166) Osterloh, F. E., Inorganic Materials as Catalysts for Photochemical Splitting of Water. *Chem. Mat.* **2008,** *20*, 35-54.

(167) Hollins, P., Coupling Effects in the Vibrational-Spectra of Adsorbed Layers with Island Structures. *Surf. Sci.* **1981,** *107*, 75-87.

(168) Wang, H.; Tobin, R. G.; Lambert, D. K.; Fisher, G. B.; Dimaggio, C. L., CO on Pt(335) - Electric-Field Screening on a Stepped Surface. *J. Chem. Phys.* **1995,** *103*, 2711-2718.

(169) Panagiotopoulou, P.; Kondarides, D. I., Effects of Promotion of TiO_2 with Alkaline Earth Metals on the Chemisorptive Properties and Water-Gas Shift Activity of Supported Platinum Catalysts. *Appl. Catal. B-Environ.* **2011,** *101*, 738-746.

(170) Hadjiivanov, K. I.; Vayssilov, G. N., Characterization of Oxide Surfaces and Zeolites by Carbon Monoxide as an IR Probe Molecule. In *Advances in Catalysis, Vol 47*, Gates, B. C.; Knozinger, H., Eds. Elsevier Academic Press Inc: San Diego, 2002; Vol. 47, pp 307-511.

(171) Hammer, B.; Nielsen, O. H.; Norskov, J. K., Structure Sensitivity in Adsorption: CO Interaction with Stepped and Reconstructed Pt Surfaces. *Catal. Lett.* **1997,** *46*, 31-35.

(172) Bradford, M. C. J.; Vannice, M. A., Catalytic Reforming of Methane with Carbon Dioxide over Nickel Catalysts. 1. Catalyst Characterization and Activity. *Appl. Catal. A-Gen.* **1996,** *142*, 73-96.

(173) Alifanti, M.; Baps, B.; Blangenois, N.; Naud, J.; Grange, P.; Delmon, B., Characterization of CeO_2-ZrO_2 Mixed Oxides. Comparison of the Citrate and Sol-Gel Preparation Methods. *Chem. Mat.* **2003,** *15*, 395-403.

VITA

John Robert Copeland

John was born in Allentown, Pennsylvania on November 15, 1986 to parents Mary and Randall Copeland. There he attended public schools until graduating from Parkland High School in 2005. John then moved to State College, Pennsylvania to attend The Pennsylvania State University until graduating with high honors in 2009 with a B.S. in chemical engineering and a minor in environmental engineering. After having been awarded GIT President's Research Fellowship from the Georgia Institute of Technology, John then moved to Atlanta, Georgia to pursue a M.S. and a Ph.D. in chemical engineering at Georgia Tech. When not conducting research, John enjoys reading, engaging in outdoor activities, working out, spending time with friends, and playing tenor saxophone in a rock and roll band.